CHAPTER I

INTRODUCTION

Thesis Objective and Scope

The objective of this research is to quantify the relationship between axial force, spindle speed, travel speed, and other process parameters for friction stir welding (FSW) at high spindle speeds (1500-5000 RPM), and correlate the results with a two dimensional fluid flow model capable of predicting the forces and torque during FSW.

In order to build an efficient control system for robotic FSW, a valid force prediction model needs to be established, and many basic physical mechanics of this process need to be understood. The 2-D model presented here represents the initial steps in developing a 3-D process model.

Process Overview

Friction stir welding (FSW) was invented and patented by W. M Thomas et al. [1] of the Welding Institute in Cambridge, UK. In FSW, a cylindrical, shouldered tool with a profiled probe is rotated and slowly plunged into the joint line between two pieces of sheet or plate material, which are butted together. The pieces are rigidly clamped onto a backing plate in a manner that prevents the abutting joint faces from being forced apart. Frictional heat is generated between the tool shoulder and the material of the work pieces. This heat causes the latter to reach a visco-plastic state that allows traversing of the tool along the weld line. The plasticized material is transferred from the leading edge of the tool to the trailing edge of the tool probe and is forged by the intimate contact of the tool shoulder and the pin profile. It leaves a solid phase bond between the two pieces.

Applications

The current industries which utilize FSW are the aerospace, railway, land transportation, shipbuilding/marine, and the construction industries. These industries have seen a push towards using lightweight yet strong metals such as aluminum. Many products of these industries require joining three-dimensional contours, which is not achievable using friction stir welding heavy-duty machine tool type equipment with traversing systems which are limited to only straight line or two-dimensional contours.

For these applications, industrial robots would be a preferred solution for performing friction stir welding for a number of reasons, including: lower costs, energy efficiency, greater manufacturing flexibility, and most significantly, the ability to follow three-dimensional contours.

Chapter II

PREVIOUS FRICTION STIR WELDING RESEARCH

In this chapter, an overview of the physical and mechanical properties of FSW will be presented. Also, previous FSW research will be reviewed in order to show how this research contributes to the science of FSW. An emphasis is placed on work that relates to the topics of process parameter quantification and thermo-mechanical modeling.

Terminology

To understand the process of friction stir welding and the focus of this research, it is worth while to define certain terminologies and their usage in this thesis.

In FSW, the tool typically consists of a cylindrical shoulder with a profiled probe, also called the pin. The material or materials being welded can be called the work piece, part, sample, or plate. The joint where the samples are abutted will be referred to as the weld line. The part used to support and clamp the sample is called the backing plate, backing bar, or anvil.

The tool rotates at an angular velocity given in revolutions per minute (RPM), which will be referred to as rotational speed (RS). The translational velocity at which the tool travels along the weld line is called the feed rate or travel speed (TS), and will be given in millimeter per second (mm/s) or inches per minute (ipm). The side of the weld where the angular velocity and forward velocity of the pin tool are additive is called the advancing or leading side. The other side where the angular velocity and translational velocity are in opposite directions is called the trailing or retreating side.

As shown in Figure 2, forces act in three dimensional spaces. The force along the X-axis, Y-axis, and Z-axis will be referred to as the translational (F_x), transverse (F_y), and axial force (F_z) respectively, and will be given in Newtons (N). The moment (Mz) about the axis of rotation will be referred to as the torque and given in Newton-meters (N-m).

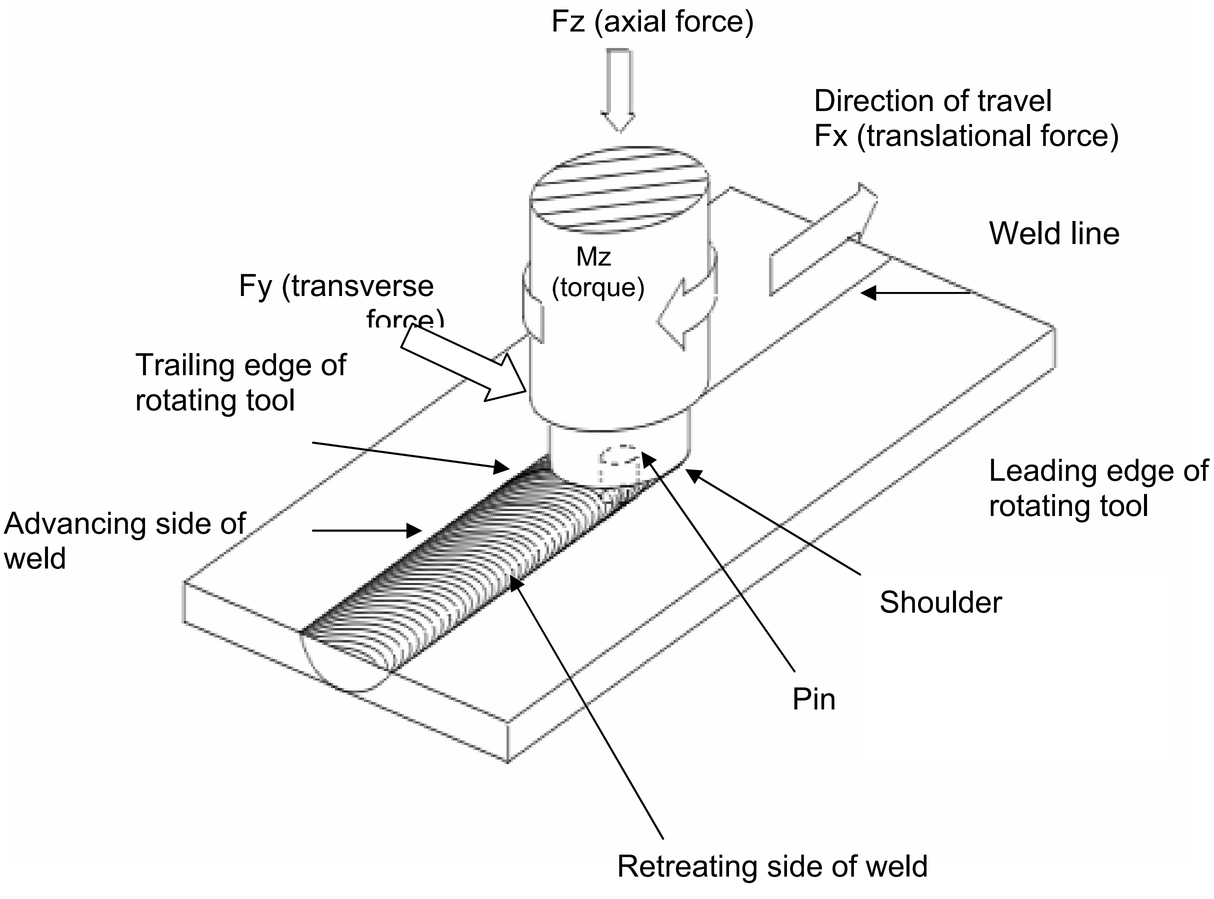

Figure 2.1 - Schematic of FSW.

Power however will be given in Watts (N-m/s). Figure 2 shows a schematic of the process and the given terminologies.

Welding Materials

A wide range of materials can be successfully joined. These materials include thermoplastics, lead, zinc, aluminum alloys, copper, silver and gold. Materials with higher melting points (in excess of 1100°C) such as ferrous metals and alloys can also be joined. However they require probes of high grade temperature resisting materials such as tungsten [1].

Aluminum has been welded in single passes ranging from 0.050" to 2" in thickness. Using a double pass method, welds up to 4" thick have been made [2]. Copper up to 2" thick has been welded. Welds up to 0.5" thick have been successfully made in steel using the double pass method, and 0.37" thick magnesium alloy AZ61A has been welded in a single pass [3].

Friction stir welding has successfully been performed in a variety of joint geometries. Butt welds, corner welds, T-sections, overlap welds, and fillet welds have all been done [2]. Circumferential welds have also been performed in the aerospace industry for the manufacture of large cryogenic tanks [33].

Welding Tools

A FSW tool may be made out of a number of different materials. Choice of a material for a tool is dependent on the type of metal material to be welded, particularly the melting temperature of the material. An additional consideration is the desired travel speed. Table 2.1 lists different tool material and the maximum operating temperatures [4].

Table 2-1. Various tool materials. [4]

Material	Approximate Max Work Temp (F)
H-13	1000
Ferro-TiC SK	1100
MP-159	1100
Stellite 6B	1600
Ferro-TiC HT-6A	1800
MAR-M-246	1900
Mo-TZM	2400
Rhenium	3600
Tungsten	3600

The tool has two basic parts; the shoulder and pin. The tool shoulder has two general functions, create frictional heat at the tool/work piece interface and to cap the plasticized material as it “stirred”.

The pin is a cylindrical pin projecting from the distal shoulder surface and has a longitudinal axis co-extensive with the shoulder longitudinal axis. The pin must be large enough to stay above the plastic stress level at operating temperatures. Current FSW practice uses a pin having a surface profile consistent with the thread of a bolt, much like the end of a machine bolt [4]. The purpose of profiling the pin is to reduce traverse loads and improve material flow [5].

Tool pin shapes have taken the form of frusto-conical, inverted frusto-conical, spherical, and pear shape, to simple conical, truncated cones, to slightly tapered cylinders [5, 6]. Cocks et al. [7] introduced a pin which has a combined right handed and left handed thread pattern. This “enantionmorphic” pin is said to produce welds of improved mechanical properties [7].

For this research, a tool made of H-13 tool steel heat treated to Rc 48-50 with a 0.5” diameter cylindrical shoulder and a threaded cylindrical pin will be used.

Weld Microstructures

The heat and deformation generated during FSW produce four micro-structurally distinct regions across the weld. They are the heat affected zone (HAZ), thermo-mechanically affected zone (TMAZ), dynamically recrystallized zone (DXZ) or weld nugget, and the unaffected material. [8]

The HAZ is the outermost portion of the weld which is modified by the thermal field of the welding process but does not experience any deformation. It is similar to the heat affected zones observed in welds prepared by more conventional fusion welding processes. Inward from the HAZ is located the TMAZ, where the material experienced plastic deformation due to the stirring process in addition to the heat-induced micro-structural changes. At the center of the weld, where the heat and deformation are the greatest, aluminum alloys undergo significant grain refinement within an onion-shaped region called the weld nugget or DXZ, which is approximately the size of the rotating pin of the tool. The unaffected, or parent-material, is material that is heated but not modified by the thermal field of the weld.

Mechanical Properties

In whole-weld tensile tests, most precipitation-strengthened aluminum alloys exhibit similar yielding and fracture behavior [9–12]. During these tests, the tensile strain becomes localized in the HAZ on both sides of the weld nugget [13]. Fracture will typically occur at this location and will usually be located on the retreating side of the weld [12]. The localization of yield and fracture at the HAZ demonstrates the importance of this region in controlling the mechanical behavior of friction stir welds. Despite this, there have been few systematic examinations of the HAZ to determine the underlying cause of this behavior.

Some studies [9–11, 14–17] have demonstrated that precipitates are significantly coarsened in the HAZ relative to those observed in the unaffected base plate or weld nugget. Sato et al. [18] examined different locations in the HAZ and weld nugget of a 6063 Al FSW and observed that the precipitates experienced increasing dissolution toward the weld center. Su et al. [19] recently reported on precipitate evolutions occurring in a 7050 Al FSW. They observed a coarsening of precipitates from the base plate into the TMAZ, with increasing dissolution and re-precipitation occurring from the TMAZ into the weld nugget.

Kwon et al. [20] investigated the influence of the tool rotation speed on the hardness and tensile strength of the friction stir welding aluminum 1050 and concluded that the hardness within the weld was higher on the advancing side than on the retreating side. Also, that in the transition zone between the weld and the parent material the variation in hardness was more drastic on the advancing side than on the retreating side and that the hardness and tensile strength of the weld increased significantly with decreased tool rotation speed.

Lee et al. [21] examined the microstructure and mechanical properties of FSW 6005 Al alloy with increasing welding speed and concluded that the tensile strength increased as welding speed increased.

Experimental and Theoretical Modeling

In this section, previous works pertaining to thermal-mechanical modeling will be reviewed. Since little is known about the physics involved during the FSW process, these works will help to provide insight into the mechanics of FSW.

Thermo-mechanical Modeling

Ulysse et al. [22] attempted to model the friction stir-welding process using three-dimensional visco-plastic modeling. The simulation was limited to one tool geometry where the tool pin was 6.4 mm in diameter and its depth into the plate was 6.4 mm, which is about 1/3 of the plate thickness. The pin was tilted by 3° from the vertical, leaning away from the direction of welding. The tool shoulder was 19 mm in diameter. The shoulder face was a 7° concave cone design.

In the model, a cylindrical shoulder recess was assumed in order to approximate the shallow concave area as shown in Figure 2.2. The tool above the work surface was approximated as a 20 mm high cylindrical shaft. The 3D finite-element (FE) friction stir-welding simulations were conducted using the commercial software FIDAP [24]. The mesh used for the FSW simulations are shown in Figures 2.2 and 2.3; about 33,000 eight-noded (brick) elements and 29,400 nodes were used in this study.

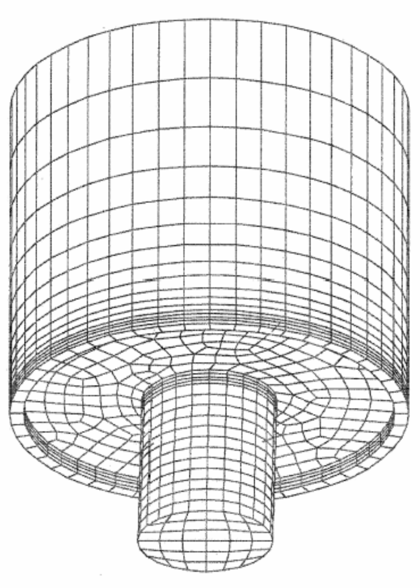

Figure 2.2 – Enlarged view of Ulysse FSW tool FE mesh. [22]

In addition, only butt joints 19.1 mm AA 7050-T7451 (2.3% Cu, 2.25% Mg, 6.2% Zn) thick plates were considered in this work. The model of the work-piece region was 60 mm wide by 100 mm in length as shown in Figure 2.3. The support table, located underneath the work-piece, is not included in the analysis in order to reduce the size of the numerical model. Therefore, heat transfer to the support table is ignored in this work.

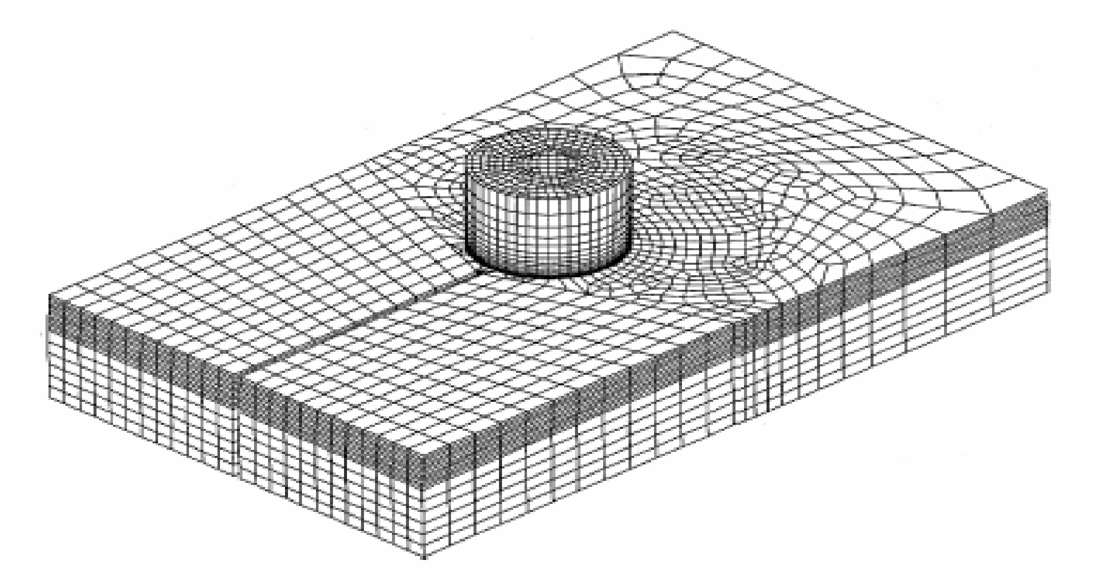

Figure 2.3 – FE mesh of the welding model. [22]

Ulysse [22] modeled the large plastic deformation involved in stir-welding processes by relating the deviatoric stress tensor to the strain-rate tensor. The TMAZ was assumed to be a rigid-visco-plastic material where the flow stress depends on the strain-rate and temperature and is represented by an inverse hyperbolic-sine relation as follows:

$$\sigma_e = \frac{1}{\alpha}\sinh^{-1}\left[\left(\frac{Z}{A}\right)^{\frac{1}{n}}\right] \quad Z = \dot{\varepsilon}\exp\left(\frac{Q}{RT}\right) \qquad \textbf{Eq. 2.1}$$

where α, *Q*, *A*, *n* are material constants, *R* the gas constant , *T* the absolute temperature and Z the Zener-Hollomon parameter [42]. The material constants were determined using standard compression tests. The mechanical model equations are complete after appropriate boundary conditions are prescribed.

The temperature distribution is obtained by solving the energy equation, expressed here as the conductive–convective, steady-state equation

$$\rho c_p \mathbf{u}\cdot\nabla\theta = \nabla\cdot(k\nabla\theta) + \dot{Q}, \quad \textbf{Eq. 2.2)}$$

where ρ is density, c_p the specific heat, u the velocity vector, k the conductivity, θ the temperature and $\dot{Q}$ is the internal heat generation rate. About 90% of the plastic deformation is assumed to be converted into heat [23]. In this work, temperature-dependent conductivity and specific heat coefficients for aluminum alloys were adopted. The heat generation rate term can be expressed as the product of the effective stress and effective strain-rate.

Comparisons of model predictions with experimental data are illustrated in Figures 2.4-2.6. All temperatures are peak temperatures. The trend of the measured data is also indicated for convenience in the figures. The following parameters were used in the comparisons: (1.0 mm/s, 11.7 rev/s), (1.37 mm/s, 8.17 rev/s), (1.9 mm/s, 11.7 rev/s), (2.593 mm/s, 11.7 rev/s), (3.54 mm/s, 8.17 rev/s), (1.9 mm/s, 11.7 rev/s), (2.593 mm/s, 11.7 rev/s), (3.54 mm/s, 8.17 rev/s), (3.5mm/s,25.5rev/s).

While various temperature measurements have been recorded, experimental measurements to validate the present force predictions are not available. Analytical predictions of axial (*Fz*) and shear forces on the pin are shown in Figure 2.5 as a function of translational speed. It can be observed that increasing the welding speed, regardless of rotational speed, has the effect of increasing the axial force thrust and shear force on the pin. In addition, for a fixed welding speed, increasing the rotational speed has the effect of decreasing the forces. Quantification of this relation over a wide parametric range is the core topic of this thesis.

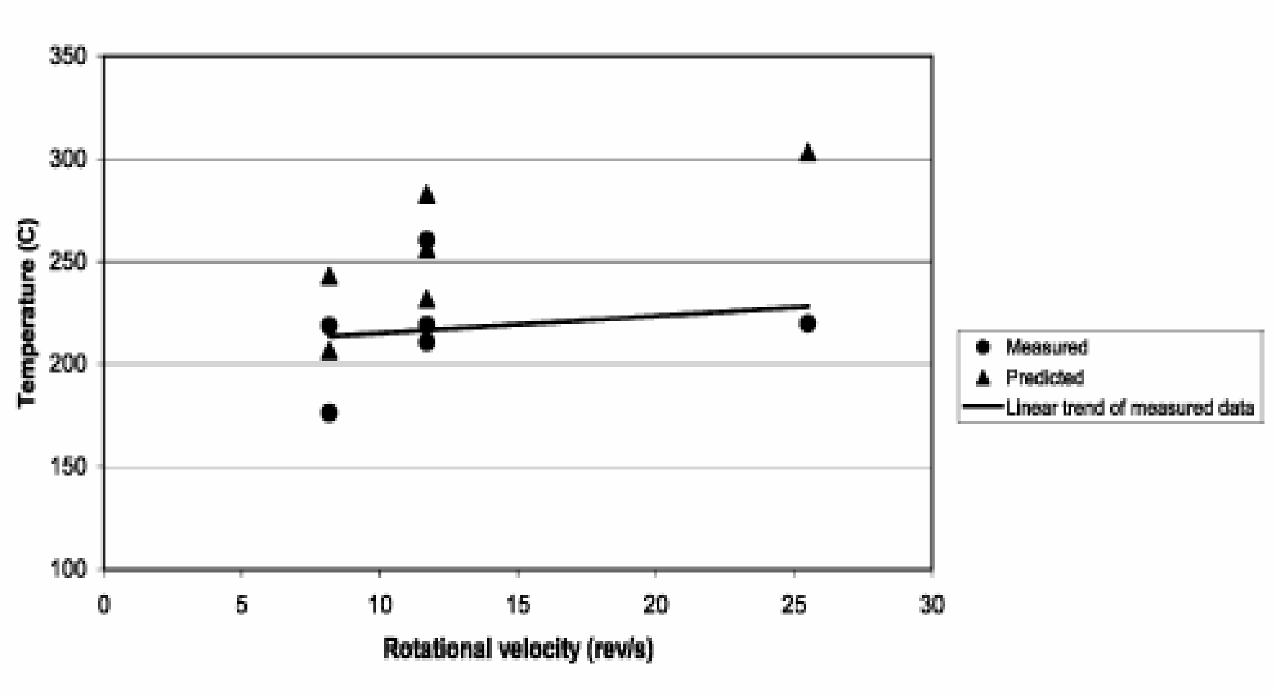

Figure 2.4 – FSW temperatures as a function of tool rotational speed. [22]

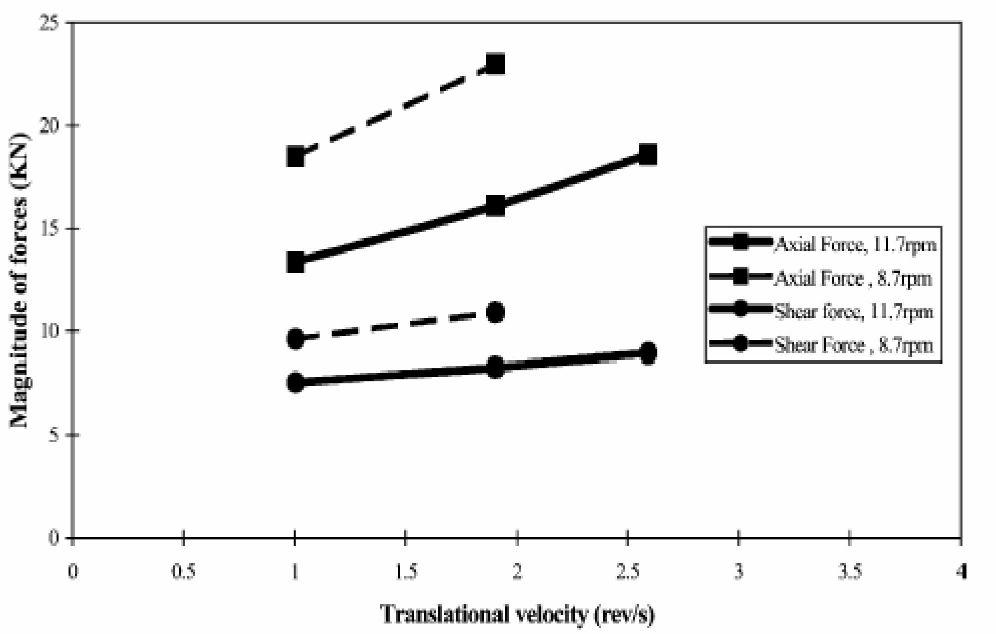

Figure 2.5 - Axial (*Fz*) and shear forces on the pin shown as a function of translational speed. [22]

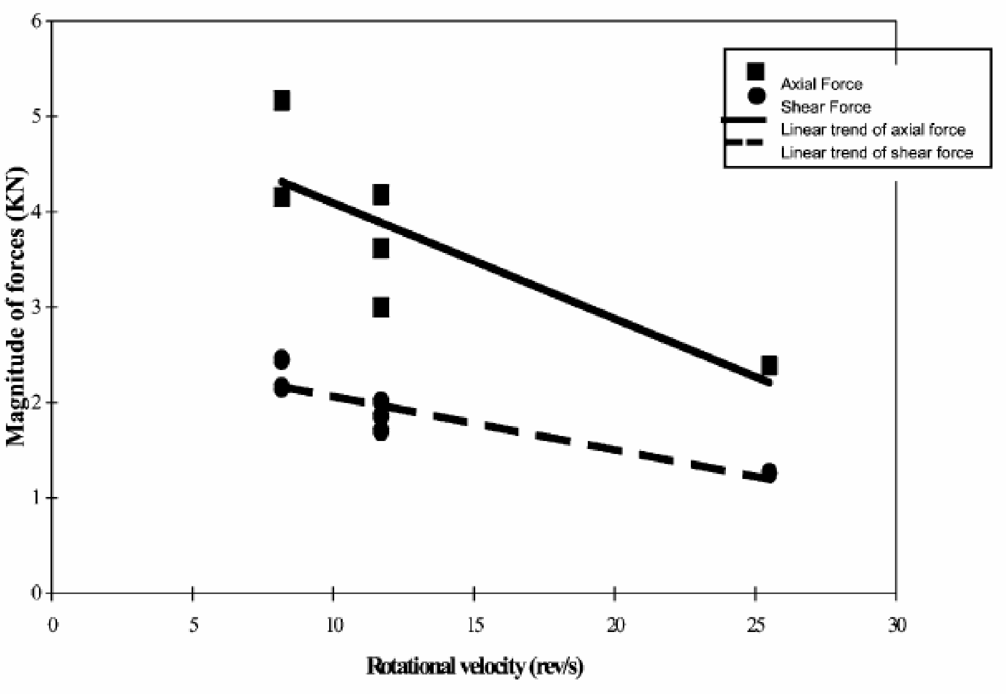

Figure 2.6 – Axial and shear forces on pin as function of tool rotational speed. [22]

Reynolds et al. [25] introduced a two dimensional model based on fluid mechanics that modeled the solid state material transport during welding as a laminar viscous flow of a non-Newtonian fluid past a cylinder. Only the tool pin was represented in the simulation. The temperature and strain rate dependent viscosity of AA6061 was based on the constitutive law of the flow stress of aluminum alloys using the Zener-Hollomon parameter (Z) (Eq. 2.1). Also, temperature dependent thermal conductivity and specific heat were used to calculate the heat transfer in the fluid.

Reynolds et al. [25] concluded that the force against the welding direction at the pin increases with increasing TS at constant SS and decreases with increasing SS at constant TS. The power increases with increasing SS at constant RS and remains constant with varying TS and constant SS.

Colegrove [30] used an advanced analytical estimation of the heat generation for tools with a threaded probe to estimate the heat generation distribution. The fraction of heat generated by the probe is estimated to be as high as 20%, which leads to the conclusion that the analytical estimated probe heat generation contribution is not negligible.

In parallel with the analytical model, Colegrove and Shercliff et al. [30, 31] developed a material flow model, which addresses the influence of threads on the material flow. An advanced viscous material model is introduced and the influence of different contact conditions prescribed as the boundary condition is analyzed [31].

Schidmt et al. sought to establish an analytical model for heat generation during friction stir welding based on different assumptions of the contact condition between the rotating tool surface and the weld piece. The material flow and heat generation are characterized by the contact conditions at the interface and are described as sliding, sticking or partial sliding/sticking. Different mechanisms of heat generation were found to be behind each contact condition. The analytical expression for the heat generation is a modification of previous analytical models known from the literature [29, 30] and accounts for both conical surfaces and different contact conditions.

Chen et al. [32] introduced a three-dimensional model based on finite element analysis to study the thermal history and thermo-mechanical process in the butt-welding of aluminum alloy 6061-T6. The model incorporates the mechanical reaction of the tool and thermo-mechanical process of the welded material. The heat source incorporated in the model involves the friction between the material and the pin and the shoulder. The dynamics of the FSW thermo-mechanical process, the thermal history and the evolution of longitudinal, lateral, and through-thickness stress in the friction stirred weld are simulated numerically. The X-ray diffraction (XRD) technique is used to measure the residual stress of the welded plate.

Chen et al. [32] suggested that the maximum temperature gradients in longitudinal and lateral directions are located just beyond the shoulder edge, and that the longitudinal residual stress is greater than the lateral residual stress at the top surface of the weld. The prediction shows that the high stress is located in the region extending down from the crown to the mid-thickness of the weld. A higher traverse speed induces a larger high longitudinal stress zone and a narrower lateral stress zone in the weld.

Nunes et al. [26] modeled the tool torque to be totally due to the shear flow stress of the metal acting perpendicular to the direction of tool rotation and integrated over the surface. The welding power is equal to the torque multiplied by the RS and is given by

$$P = \omega_0 M_z$$

$$M_z = \int_{R_p}^{R_s} 2\pi R_p \sigma dR_p + 2\pi R_p^2 t\sigma + \int_0^{R_p} 2\pi R_p^2 \sigma dR_p , \qquad \textbf{Eq. 6.3}$$

where M_z is the welding torque, ω_o is the tool rotational speed, R_p is the pin radius, R_s is the shoulder radius, σ is the shear flow stress, and t is the pin depth. Figure 2.7 shows a comparison of Mitchell et al. [27] experimental torques to torques computed from the Nunes et al. model [26].

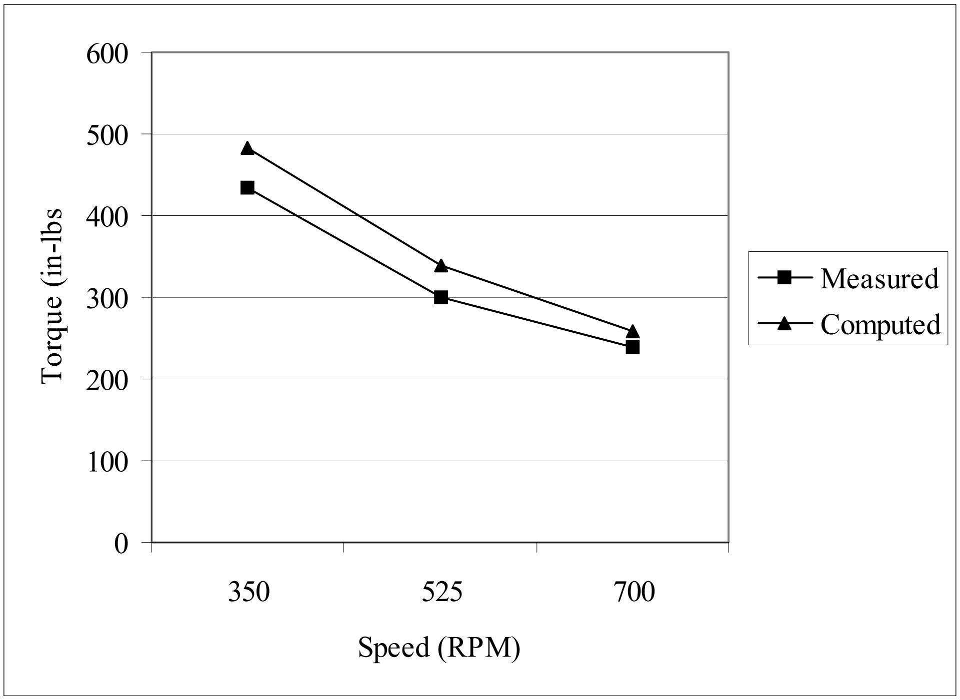

Figure 2.7 - Comparison of Mitchell et al. [27] experimental torques to torques computed from Nunes et al. model.

Flow Field Visualization

The visualization of material flow during friction stir welding is key to understanding the internal workings of the process and is critical to process modeling.

Nunes et al. [26] state that the flow field around a standard threaded tool or tools with threadlike features is comprised of two parts. The primary flow of material is around the tool in the direction of rotation. There is a plug of metal that rotates with the pin, and the flow gradient goes from the velocity of the plug at the plug surface to zero some distance away. Nunes et al. [26] states that the plug radius occurs at a point that creates a minimum torque for a given shear flow stress. The plug hypothesis is supported by computational fluid dynamics work done by Dong et al. [33], which predicted that a plug of metal rotates with the tool. The plug model can be seen below in Figure 2-8.

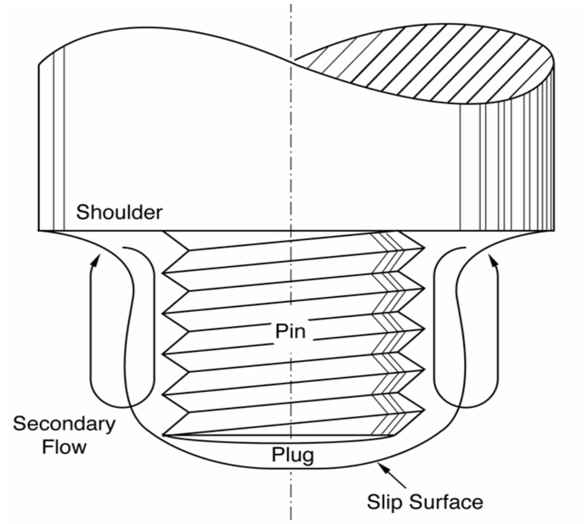

Figure 2.8 - Secondary Flow Caused by Threads.

Ulysse [22] was able to extract useful information along the path line of a material particle traced in the welding region from the visco-plastic FSW model. The path line of a material particle located just underneath the pin tip was traced back to its original location in the shoulder recess. The temperature history of the particle along the path line is shown in Fig. 2.9. As seen in the figure, the particle was traced back in time from $t = 2$ s (at the pin tip) to 0 s (near the shoulder region).

For about 0.5 s, the particle rotates around the top of the pin with a relatively small downward or axial velocity Uz; and during this time, its temperature remains relatively uniform. After the initial 0.5 s, the particle follows the pin rotation and downward motion which sets up some periodicity in the temperature history.

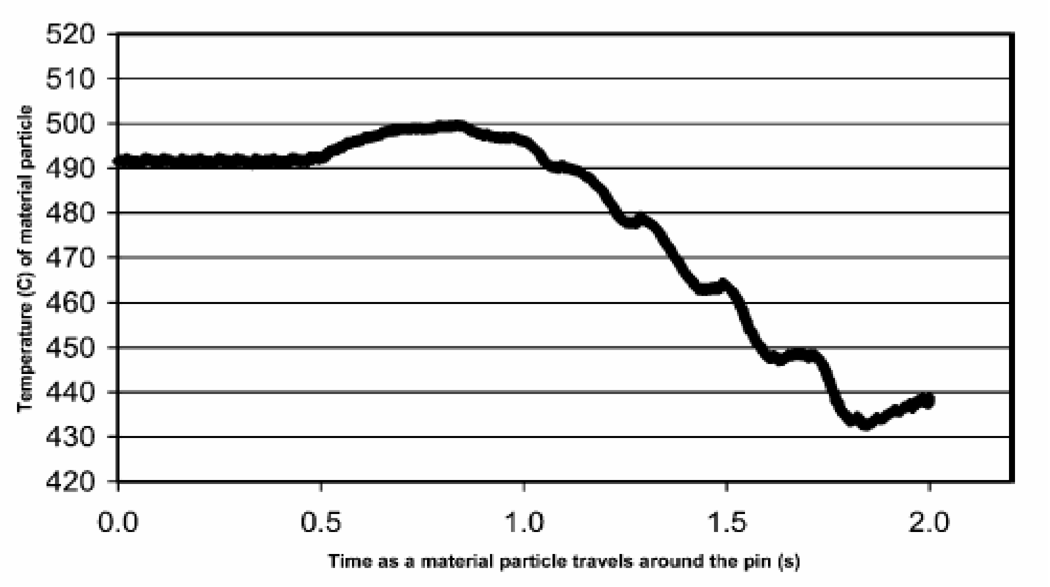

Figure 2.9 - Temperature (in °C) history of a material particle near the pin. [22]

As the particle rotates, it crosses cold and hot regions located at the leading and trailing edges of the pin, respectively, which explains the peaks in Fig. 2.9. The material particle is also pushed downward, toward the tip of the pin, where temperatures are relatively cold, which explains the decreasing trend in temperature.

Guerra et al. [28] investigated the flow of metal during FSW using a faying surface tracer and a pin frozen in place during welding. It was shown that the material is transported by a wiping of material from the advancing front side of the pin onto a zone of material that rotates and advances with the pin. The material undergoes a helical motion within the rotational zone that rotates, advances, and descends in the wash of the threads on the nib and rises on the outer part of the rotational zone. After one or more rotations, this material is sloughed off in the wake of the pin, primarily on the advancing side. The second process is an entrainment of material from the front retreating side of the nib that fills in between the sloughed off pieces from the advancing side.

Colligan et al. [29] followed material flow in 6061 and 7075 aluminum by imbedding small steel balls as tracers into grooves cut into the work-piece parallel to the weld direction. Grooves were cut parallel to the weld direction but at various distances from the weld centerline and at various depths. After welding, the distribution of the steel balls was revealed by radiography in both the plan and the cross-sectional views. Results
are displayed nicely in the original paper but, in general, the work showed that the material striking the pin on the advancing side of the weld would be displaced from the rear of the retreating side of the pin.

CHAPTER III

EXPERIMENTAL PROCEDURE

Both experimental and analytical results [22, 23] show that the axial force (and other forces) can be reduced by increasing the spindle speed. The full range over which this apparent relationship can be expected to hold true is not known. A full quantification of the relationships between spindle speed and other process parameters for friction stir welding are needed. These relationships are of fundamental importance to improved weld productivity with the friction stir welding process and are key to the widespread use of robots for FSW.

Vanderbilt University Welding Automation Laboratory FSW Experiments

To study this relationship, experiments were performed at the Vanderbilt University Welding Automation Laboratory using a Milwaukee #2K Universal Milling Machine fitted with a Kearney and Trecker Heavy Duty Vertical Head Attachment modified to accommodate high spindle speeds. The weld sample, clamping fixture (or backing plate), tool design, instrumentation, and machine modifications detailed below.

Sample Description

For this experiment, plates of AL 6061-T651 aluminum, nominally 0.250 inches thick were friction stir welded. The samples were 3 inches wide by 18 inches long. The tool depth was set to 0.145”. To ensure precise setting of the tool depth, the tool was positioned along the weld line aft of the samples leading edge. The sample is clamped via the scheme shown in Figure 3-1.

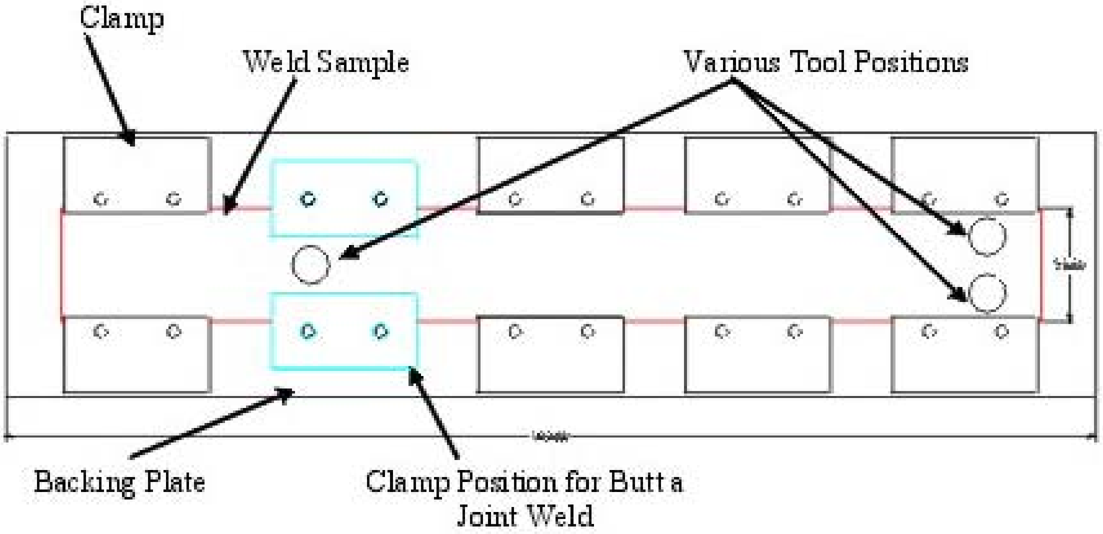

Figure 3-1: VU FSW backing plate.

The clamping system allows for 30 inches of travel and samples with 3” or 5” widths. Using the horizontal spindle, the maximum travel distance was 12 inches and limited to 3” width samples. See Appendix A for a detailed schematic of the backing plate.

Tool Design

For this experiment, the tool was made from H-13 tool steel heat treated to Rockwell c hardness 48-50. The shank diameter was 1”. The tool shoulder was flat with a 0.50” diameter. The pin was cylindrical with a 10-24 threads per inch left hand pattern.

The pin length was 0.1425" and the diameter was 0.190". Heat sinks were cut into the far end of the tool shank near the shoulder to facilitate heat dissipation during welding. The tool was rigidly mounted into the tool holder using a twist lock system. The tool lead angle was set to 2º. Figure 3-2 shows a detailed schematic of the tool.

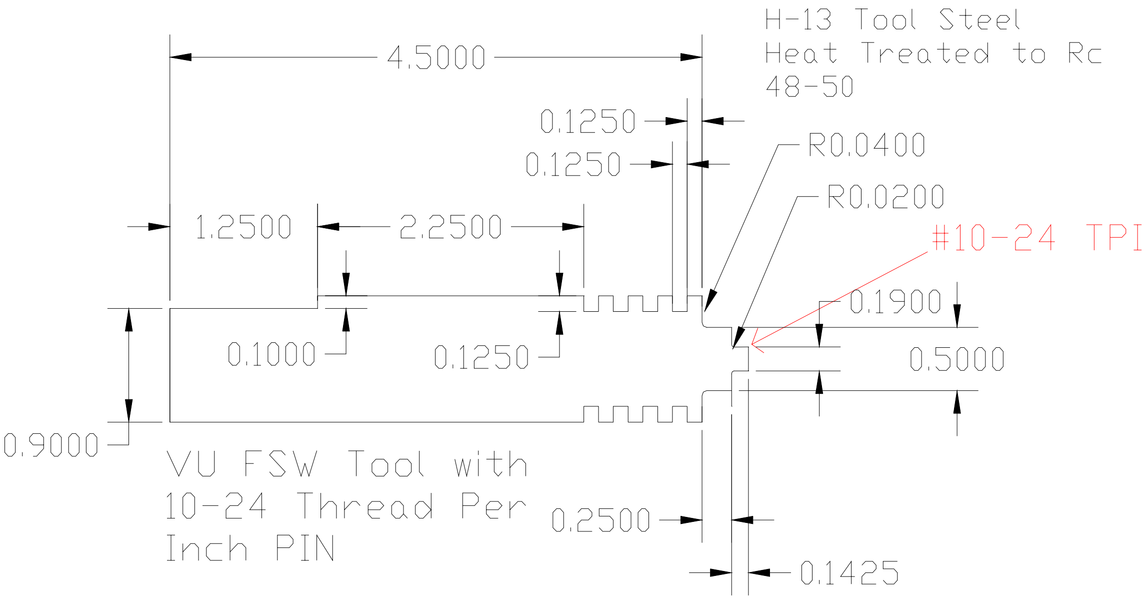

Figure 3-2: VU FSW tool with 0.5" shoulder and left hand 10-24 thread pattern.

Instrumentation

A Kistler rotating quartz 4-component dynamometer (RCD) was used for measuring forces and torque on the rotating tool. The dynamometer (Figure 3-3) consists of a four component sensor fitted under high preload between a base plate and a top plate. The four components are measured without displacement. The four component sensor is ground-insulated, therefore ground loop problems are largely eliminated. The dynamometer is rustproof and protected against penetration of splash water and cooling agents. For each component a 2-range miniature charge amplifier is integrated in the dynamometer. The output voltages of the charge amplifiers are digitized and transmitted by telemetry to the stator and then acquired by a PC. The stator is rigidly mounted concentrically with the RCD with a 2 mm gap between them. A mount was fabricated and bolted to the face of the vertical head. A detailed schematic of the stator mount can be seen in Appendix A.

The Kistler data acquisition software DynoWare was used for data collection. DynoWare records the three forces and torque during welding and allows the data points to be exported to a tabularized text file. The data is then imported into MATLAB 7.0, where it is run through a linear smoothing filter and is plotted. Please see Appendix C for the linear smoothing filter program file.

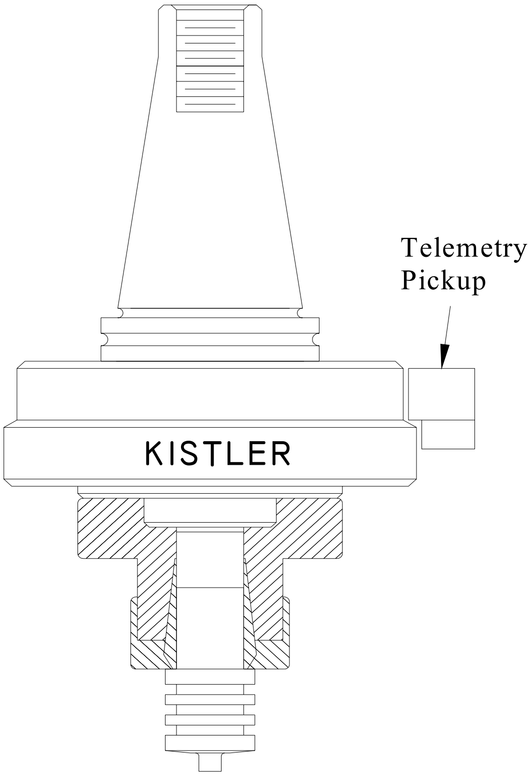

Figure 3-3: Kistler Rotating Cutting Force Dynamometer

Machine Modifications

Welding is performed on a Milwaukee #2K Universal Milling Machine fitted with a Kearney and Trecker Heavy Duty Vertical Head Attachment modified to accommodate high spindle speeds. The vertical head clamps the vertical sliding surface of the milling machine. A Baldor VM2514, 20 HP, 3450 RPM, 3Phase 230 VAC motor is mounted to the shoulder of the head and drives the vertical spindle via a Poly-V belt (Browning 380J16) and drive system. The motor is controlled by a Cutler Hammer SVX-9000 20HP variable frequency drive. Please see Appendix A for a detailed schematic of the motor mount.

To meet the operational speed requirements, a 1.33 pulley over drive ratio was used. The large pulley's (Browning 16J60P) diameter was 6" while the smaller pulley's (Browning 16J45P) diameter was 4.5". The maximum speed using the above configuration is 4800 rpm. The overdrive ratio was selected to prevent the possibility of over-speeding the RCD, whose max operational speed is 5000 rpm. Over-speeding would require the RCD to be recalibrated. Therefore the maximum rotational speed at which data was collected for this experiment was 4500 rpm.

To reduce the inertial load of the vertical spindle, the gear train which coupled the head to the milling machine drive was removed. The gearing system total weight was approximately 50 lbs. This reduction of loading allows for more torque to be available during welding.

The head was originally grease lubricated, and accommodated a maximum operational speed of 1500 rpm. To suit the higher operational speeds for the experiment, the lubricating grease was cleaned from the spindle's tapered roller bearings. A Bijur

Fluid Flex Pressurized Lubricating System was used to lubricate the tapered roller bearings.

The Fluid Flex system dispenses a mixture of compressed air (125 psi maximum) and oil (DTE Lite ISO VG 32). The compressed air is filtered through an air filter/regulator (160 Psi maximum) with a ¼ NPT inlet. The air enters the Fluid Flex system and is reduced to a desired level and passed through a solenoid valve which synchronizes the system with the spindle. Low-pressure air enters the fluid reservoir and forces fluid from the reservoir. Separate lines carry an atomized mixture of air and oil through the distribution lines in the system to the Jet Tip assembly for discharge onto the tapered roller bearings (Timken #455 and #749) of the spindle. Figure 3-4 shows the VU FSW test bed.

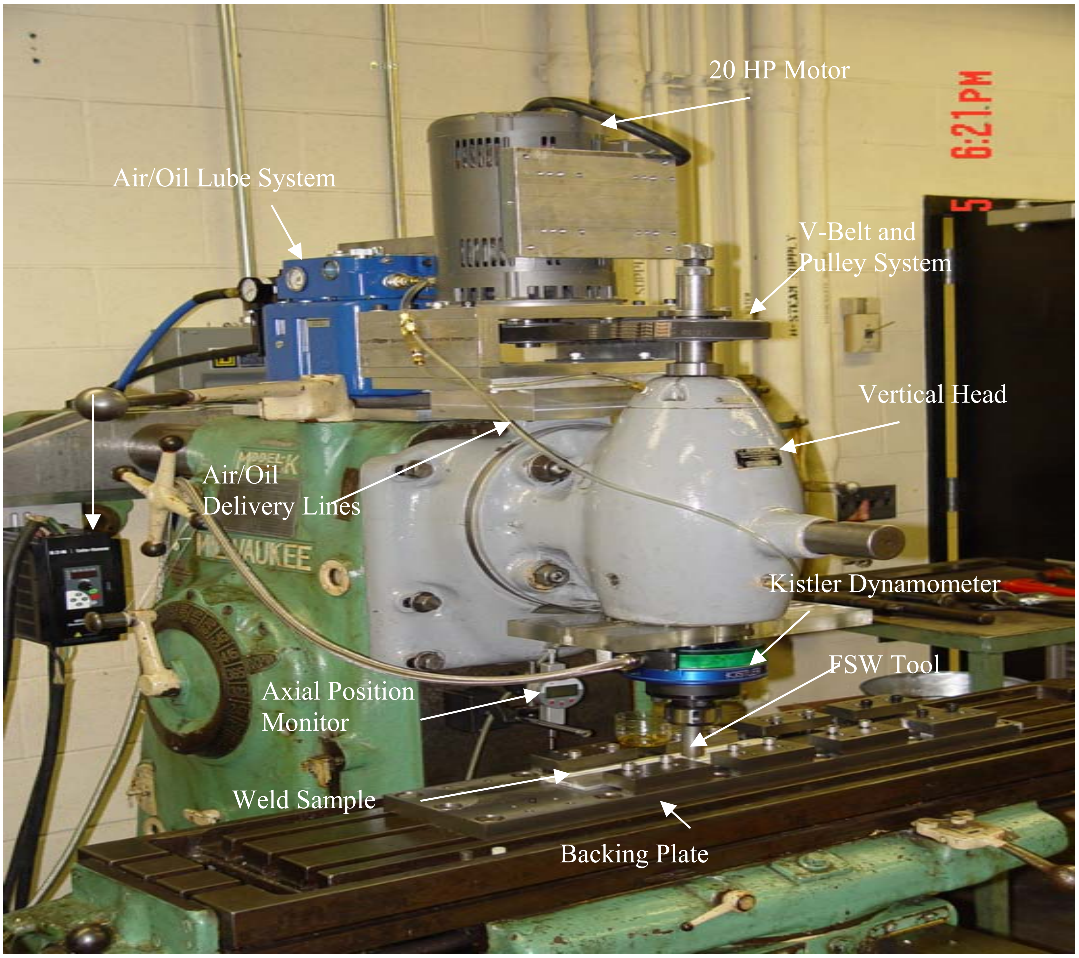

Figure 3-4 VU FSW test bed.

The experimental procedure is as follows:

1. Program the spindle speed.
2. Set the travel speed.
3. Set the tool depth.
4. Start the lubrication system.
5. Start the machine spindle.
6. Plunge the tool into the material.
7. Start the data acquisition.
8. Engage the table travel.
9. Travel 18”.
10. Stop the spindle.

Using the procedure above, welds were made for the parameter set below.

Table 3-1: VU FSW Experimental Parameter matrix.

Feed Rate (ipm)

Spindle Speed (RPM)	11.4	27	37.2	44.8	53.3	63.3
1500	X	X	X	X	X	X
2250	X*	X	X	X	X	X
3000	X**	X	X	X	X	X
3750	-	X	X	X	X	X
4500	-	-	-	X	X	X

*Actual Rotational Speed was 2000 RPM
** Actual Rotational Speed was 2500 RPM

The parameters for which welding was not conducted are those where the rotational speed is too high for the travel speed and creates a weld with a deformed surface as shown in Figure 3-5. The overheat phenomena occurred at the preceding parameter set. For example, for the 3750 rpm and 37.2 ipm parameter set, the weld experienced the overheat phenomena. Therefore a weld for 4500 rpm and 37.2 ipm was not run because the surface deformation is assumed to only increase. Detailed photographs of the deformed welds can be seen in Appendix C. A discussion of the suggested optimum weld pitch, the ratio of rotational speed to travel speed for a specified parameter pair, will be discussed in Chapter 5.

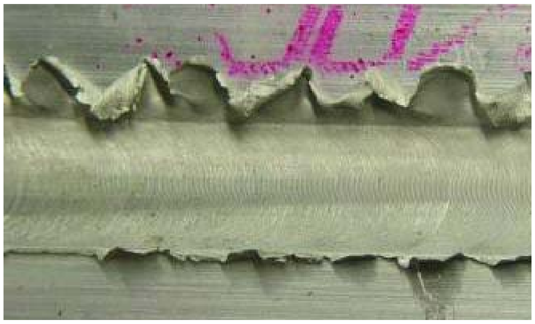

Figure 3-5: Typical weld deformation for overheat phenomena experienced during experimentation. (Parameter Set: 3750 rpm and 27.7 ipm.)

CHAPTER IV

THEORETICAL MODELING PROCEDURE

In FSW, a cylindrical, shouldered tool with a profiled probe is rotated and slowly plunged into the joint line between two pieces of sheet or plate material, which are butted together. Following tool penetration, the friction stir welding operation depends on continuous refurbishment of the visco-plastic layer surrounding the rotating tool. The term 'third body' has been used to describe the region containing the visco-plastic material produced during frictional welding and friction surfacing [34]. This terminology will be applied for the remainder of this thesis.

It is apparent that the development of a satisfactory 3-dimensional process model for FSW will depend on how well the ‘third body’ region is handled, in particular how the material properties in this region are determined. A logical first step in developing a full 3-dimensional representation of the friction stir welding process is to develop a working 2-dimensional model. For this thesis, only the pin bottom and the sample are considered. This allows a basic approach where the model is modularly developed. The model is validated in stages, which allows the contribution of various components to be examined and understood. The key factors during FSW which were considered in this model are detailed below.

Currently FSW process modeling typically incorporates either a solid or fluid mechanics approach. Experimental results have been shown to correlate with models using either approach. Due to the moderately high temperatures associated with FSW (up to 480 °C) (Sato et al. [18]), and the relatively low melting point of Al 6061-T6 (652°C);

it is clear the weld material in the third body region enters what is called a mushy zone [35].

A mushy zone is a temperature region where the material is not a true solid or liquid, though it has aspects of the behavior of both. Understanding and accurately modeling the third body region will lead to an optimal 3-D model.

FSW Modeling: A Fluid Mechanics Approach

Using a fluid mechanics approach, the third body region is approximated as a viscous flow domain under high shear stress and strain-rates at moderately high temperatures. The thermo-mechanical property of primary importance for a model such as this is the material viscosity.

Mechanical Model: Part 1

For the fluid mechanical approach to FSW modeling, the determination of the material viscosity is the logical first step to begin development of a 3-dimensional model for friction stir welding. North et al. [36] experimentally correlated the material viscosity during FSW with the viscosity of a fluid intermediate between two concentric cylinders as first suggested by Couette in 1890 [45]. Figure 4-1 shows a schematic of the Couette Viscous Flow model. The material viscosity is found to be [45]

$$\mu = (r_1^2 - r_o^2)\, M \;/\; [4\pi\, r_1^2\, r_o^2\, (\omega_1 - \omega_0)] \quad \textbf{Eq. 4.1}$$

The inner cylinder has radius r_o, and angular velocity ω_o while the outer cylinder has r_1 and ω_1, respectively, and M is the torque per unit depth of the tool pin. Applying

Equation 4.1 to FSW; take r_o to be the radius of the tool pin, and set ω_o equal the tool rotational speed.

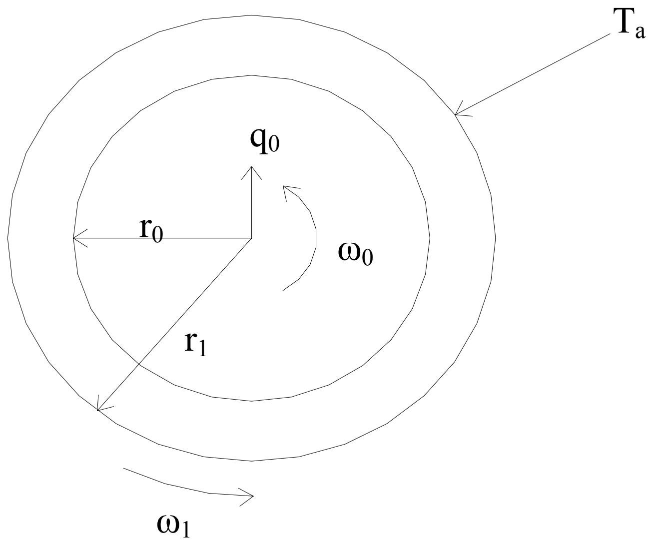

Figure 4-1: Geometry and boundary conditions for the simple Couette flow model.

The outer cylinder radius r_1 is taken to be the radius of the tool pin plus the width of the third body region to a point in space where the material is solid and does not rotate, giving $\omega_1 = 0$. M is the experimentally measured steady state welding torque for the parameter sets in Table 3-1.

Couette flow will be unstable if it satisfies the Rayleigh criterion for Couette flow instability [37]. The criterion states that Couette flow will be unstable if

$$\frac{d}{dr_o}\left|\omega_o r_o^2\right| < 0 \qquad \textbf{Eq. 4.2}$$

$$\omega_0 r_0^2 > \omega_1 r_1^2 \qquad \textbf{Eq. 4.3}$$

Equation 4.2 simplifies to ω_o r_o , which is always greater than zero for friction stir welding. Since $\omega_1 = 0$ when applying Couette flow to FSW, Equation 4.3 simplifies to $\omega_o r_1^2 > 0$, which is always true for FSW. There fore the flow is always stable for FSW.

The width of the third body region as shown in Figure 4-2, and is modeled as

$$Wr = \alpha\left[\beta\phi^2 + R_p\phi + 1\right]^{-1} \qquad \textbf{Eq. 4.4}$$

where ω is the rotational speed of the tool pin, v_f is the travel speed, and R_p is the radius of the tool pin [38]. For notation purposes, from this page forward in this thesis, R_p will be used as the notation for the tool pin radius.

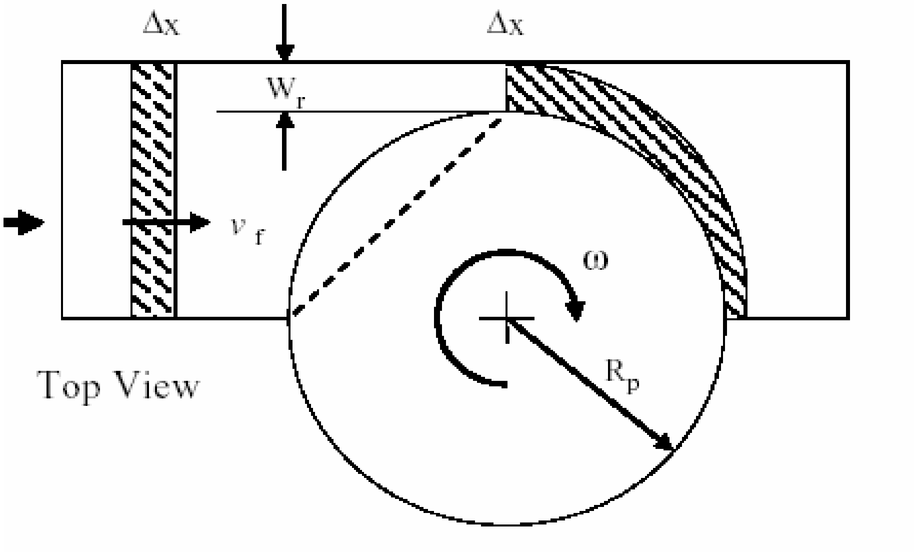

Figure 4-2: Schematic for the approximation of the third body region. [38]

The variables α, β, and φ are given by

$$\alpha = 1/2\,[(R_p) - \lambda\,\delta^2]^{-1} \qquad \textbf{Eq. 4.5}$$

$$\beta = (R_s^2 - R_p^2) / (h\lambda) \qquad \textbf{Eq. 4.6}$$

$$\varphi = \omega v_f^{-1} \qquad \textbf{Eq. 4.7}$$

where R_s is the radius of the shoulder, δ^2 is the projected thread area, and λ (24 threads per inch) is the number of threads per inch. Since the model presented here is two dimensional, secondary flows created by the threads are neglected.

Figure 4-3 shows the material viscosity for FSW using the Couette flow model.

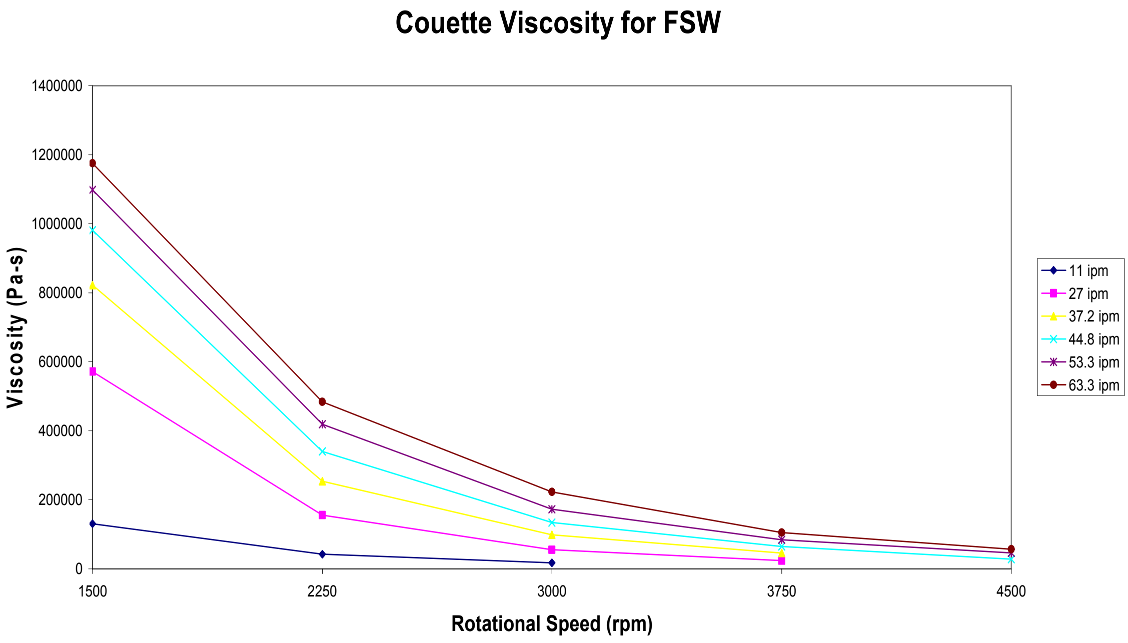

Figure 4-3: Couette Flow Viscosity for FSW.

Mechanical Model: Part 2

Applying the rigid-visco-plastic viscosity approximation used by Ulysse [22] and Reynolds et al. [25], the material viscosity is found as

$$\mu = \frac{\sigma_e}{3\dot{\varepsilon}_t} \qquad \textbf{Eq. 4.8}$$

where σ_e is the flow stress and is found by Equation 2.1. The material constants for the constitutive law (Equation 2.1) for Al 6061 are: $\alpha = 0.045\ (\mathrm{Mpa})^{-1}$, $Q = 145\ \mathrm{kJmol}^{-1}$, $A = 8.8632E6\ \mathrm{s}^{-1}$, $n = 3.55$, and $R = 8.314\ \mathrm{mol}^{-1}\mathrm{K}^{-1}$. The material constants were first published by Sheppard and Jackson [42]. The time average mean strain rate ($\dot{\varepsilon}_t$) is found as a function of the geometry, extrusion zone width, and FSW processing parameters as suggested by Abregast et al. [38].

$$\dot{\varepsilon}_t = \frac{6\,(v_f)\,\ln\left(\dfrac{h\,(R_p + W_r)}{[h - (\boldsymbol{\omega} / v_f)(W_r / \boldsymbol{\lambda})]\,[W_r + \lambda\delta^2]}\right)}{(R_p + W_r)} \qquad \textbf{Eq. 4.9}$$

Figure 4-4 shows the mean strain-rate for the parameter sets in Table 3-1.

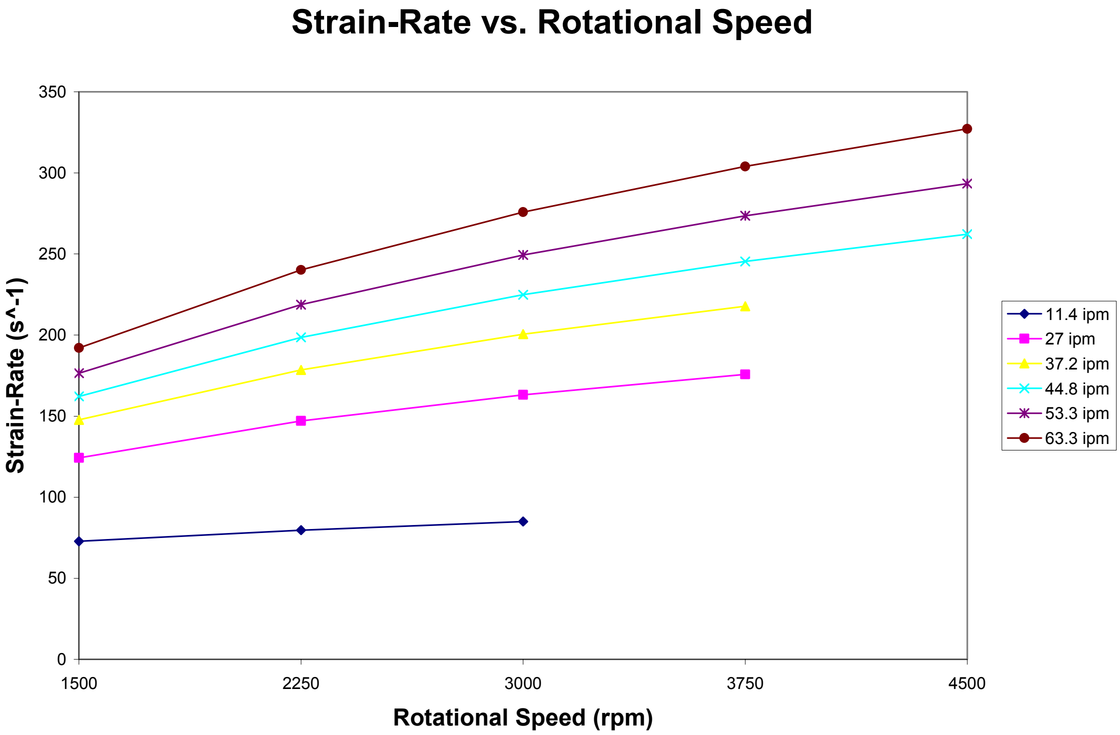

Figure 4-4: Mean Average Strain-Rate vs. Rotational Speed for Constant Travel Speeds.

The flow stress depends on the strain-rate and temperature and is represented by an inverse sine-hyperbolic as shown in Equation 2.1. As shown in Figure 4-5, using the time average mean strain-rate found above, the flow stress for temperatures ranging from 20ºC to 720ºC were found for each parameter set in Table 3-1.

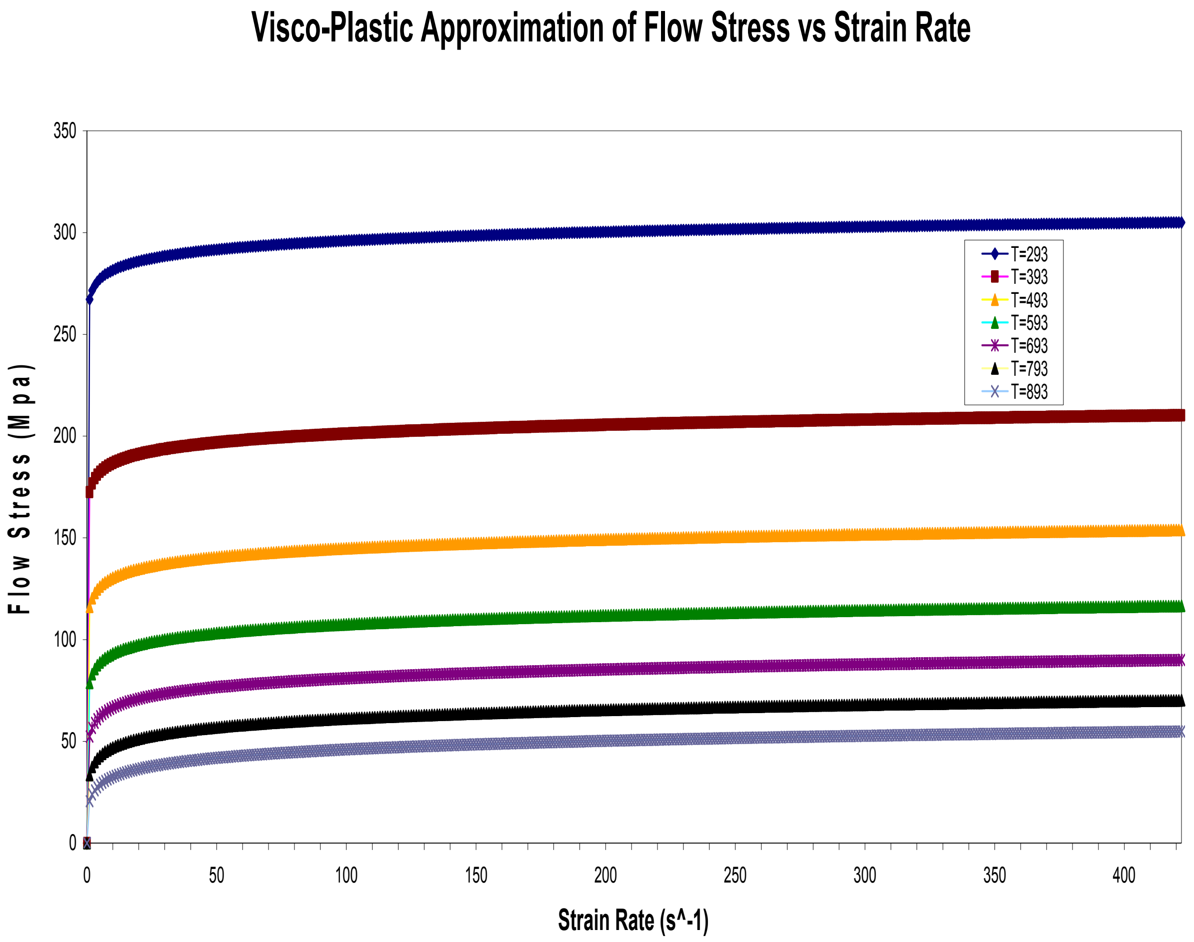

Figure 4-5: Flow Stress vs. Strain Rate using the Visco-Plastic model.

Then, applying Equation 4.8, the strain-rate/temperature dependent material viscosity was found for each parameter set in Table 3-1.

Thermal Modeling

A very important factor during friction stir welding is the steady state welding temperature. For this experiment the rotational speed was varied for the range of travel speeds listed in Table 3-1. It was observed that the rotational speed is the primary factor associated with heat generation. During the experiment, the rotational speed was constant, which should result in a constant rate of heat generation.

Various models exist which predict the heat generation during FSW. In the model by Chao and Qi [39], the heat generation comes from the sliding friction, where Coulomb's law is used to estimate the shear or friction force at the interface. Russell and Shercliff [40] based the heat generation on a constant friction stress at the interface, equal to the shear yield stress at elevated temperature, which is set to 5% of the yield stress at room temperature. The heat input is applied as a point source or line source as in the normal version of Rosenthal's equations, but the solution is modified to account for the limited extent of the plate width. Schmidt et al. [41] estimated the heat generation based on assumptions for different contact conditions at the tool/material interface in FSW joints. In this thesis, a sticking condition at the tool/material interface is assumed. The heat generation model during FSW for a sticking interface [42] at the pin sides is

$$Q_p = 2\pi(\sigma_y / \sqrt{3})\, R_p^2 h\, \omega_o \qquad \textbf{Eq. 4.10}$$

where σ_y is the yield stress of AL 6061-T6, R_p is the radius of the pin, h is the height of the pin and ω_o is the rotational speed. The incoming weld material temperature was set to 300 K. Applying Equation 4.9 for AL 6061 – T6 at 300 K, gives σ_y = 241 MPa. Substituting this result into Eq. 4.10 gives the heat generation shown in Figure 4-6.

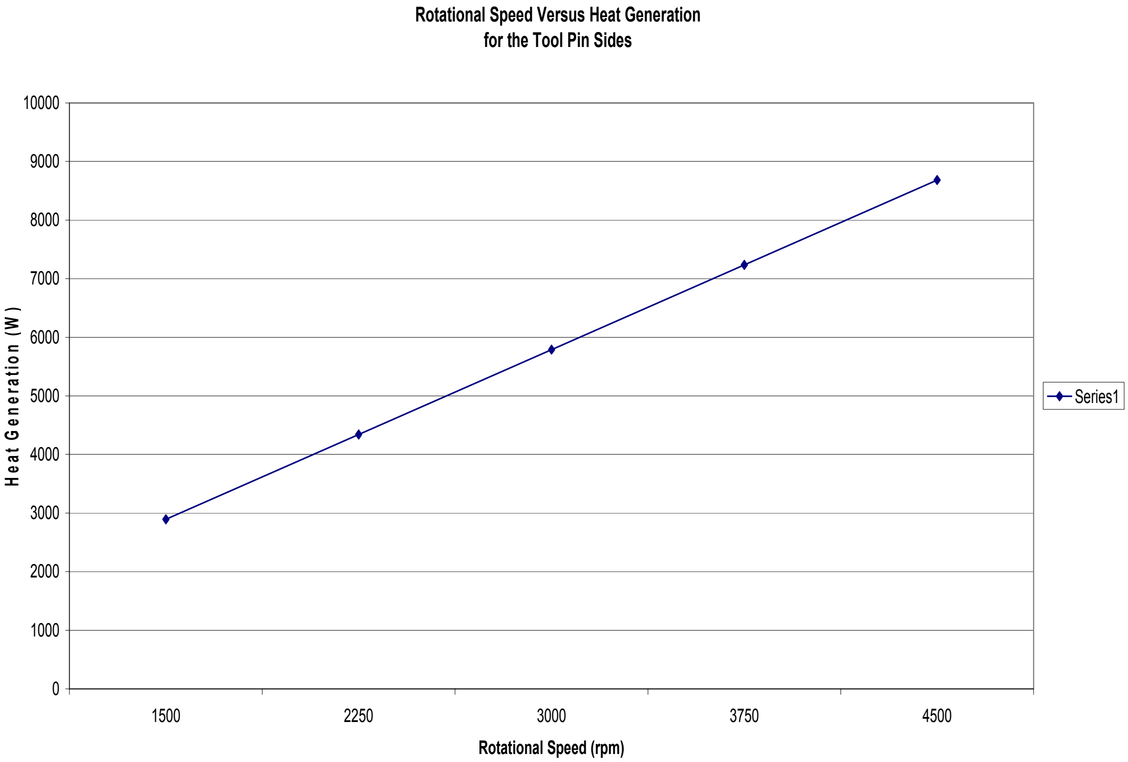

Figure 4-6: Heat Generation as a function of Rotational Speed for a sticking contact surface.

Numerical Model

The computational fluid dynamics package FLUENT [43] was used to simulate flow past a 2-dimensional pin for the weld parameters given in Table 3-1. The FLUENT package includes the following software:

1) FLUENT, the solver.

2) prePDF, the preprocessor for modeling non-premixed combustion in FLUENT.

3) GAMBIT, the preprocessor for geometry modeling and mesh generation.

4) TGrid, an additional preprocessor that can generate volume meshes from existing boundary meshes.

5) Filters(translators) for import of surface and volume meshes from CAD/CAE packages such as ANSYS, CGNS, I-DEAS, NASTRAN, PATRAN, and others.

The flow field around the pin is modeled in 2D with the Z-axis of the pin perpendicular to the direction of flow. The pin is modeled as a circle and a square flow domain is created around it. Velocity at the inlet of the flow domain is specified by the user. The procedure for implementing the model is:

1. Create the geometry (pin and the flow domain)
2. Mesh the domain
3. Set the material properties and boundary conditions

The geometry and mesh (Figure 4.7) are created using Gambit and are exported to FLUENT.

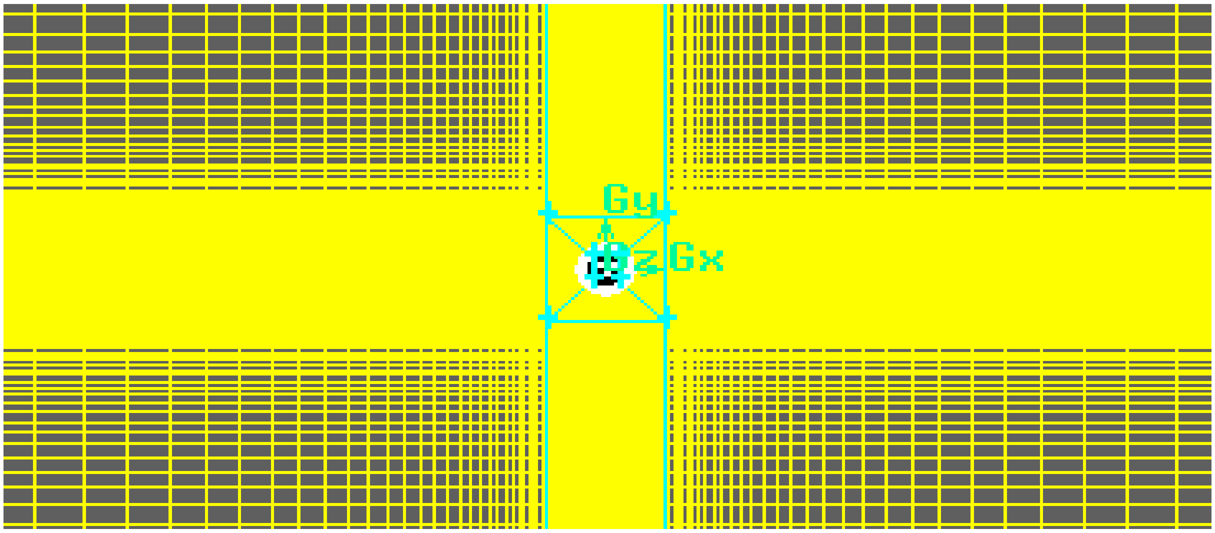

Figure 4-7: 2-D mesh of pin and sample with the origin shown at the tool pin center.

The pin has a diameter of 0.190” and the sample dimensions are 6”x3”. Because the area of most interest is near the pin, the mesh is densest near the pin and in the primary flow path of the material which contacts the pin. A 10-row boundary layer is placed at the pin wall. The flow domain is meshed using a quad map scheme using user specified discretization values.

Process Model

The three dimensional friction stir welding process is represented here by only the pin bottom and the sample. This 2-D model is the logical first step in developing a 3-D model. The process is represented here as a steady state two-dimensional laminar, incompressible, non-Newtonian flow past a rotating non-threaded tool pin. Plunge conditions are ignored. The heat generation, as detailed earlier in this chapter, is assumed to be mainly due to the contact condition from rotation of the tool pin, and the contribution from forward travel of the tool pin is negligible.

Material Properties

The material properties used as input variables for FLUENT are detailed below. Table 4-1 lists the constant properties for H-13 tool steel while Tables 4-2 and 4-3 list the temperature dependent properties for the weld material (AL 6061).

Table 4-1: FSW Tool Properties

Material Property	Density (ρ)	Thermal Conductivity (k)	Specific Heat (Cp)
H-13	7805 (kg/m3)	202 W/(m-K)	871 (J/kg-K)

Table 4-2 Temperature Dependent Yield Strength of AL 6061-T6

T (K)	σ_y (MPa)
311	241
339	238
366	232
394	223
422	189
450	138
477	92
533	34
589	19
644	12

Table 4-3 Temperature Dependent Thermal Conductivity and Specific Heat for AL 6061-T6

T (K)	K [W / (m-K)]	Cp [J / (kg-K)]
293	195	870
373	195	950
473	173	980
573	211	1020
673	212	1060
773	225	1150
873	200	1160
915	90	1170
973	91	1170
1073	92	1170

Boundary Conditions

The pin is assigned a constant rotational speed. The heat flux and heat generation rate are determined by dividing Equation 4.10 by the pin surface area and volume respectively. The wall thickness is set equal to the pin radius. The pin material is H-13 tool steel. The properties are listed in Table 4-1.

The lateral edges of the mesh are specified as a translational flow domain. This feature specifies that the fluid translates between these boundaries with a user specified velocity magnitude and direction. The magnitude is equal to travel speed during welding and the flow direction is in the positive X direction.

The inlet velocity is set to the travel speed with the flow direction in the positive X direction. The inlet temperature of the weld material is set to 300 K. The outlet pressure is set to 101,325 Pa.

The fluid is AL 6061 with temperature dependent properties from Table 4-2 and 4-3. The viscosity is for each found using Equation 4.1 (Couette) or 4.8 (Visco-Plastic). The weld material is assumed to be fed towards the tool at the user specified travel speed and temperature.

So*lver*

The solver controls for the simulations were set to 2-D, segregated, laminar, implicit, and steady flow. Using a segregated solver, the governing equations are solved sequentially (i.e., segregated from one another). Because the governing equations are non-linear (and coupled), several iterations of the solution loop must be performed before a convergent solution is obtained. The iteration process consists of the steps illustrated in Figure 4-8 and are outlined below:

The steps are as follows:

1. Fluid properties are updated, based on the current solution. (If the calculation has just begun, the fluid properties will be updated based on the initialized solution.)

2. The u, v, and w momentum equations are each solved in turn using current values for pressure and face mass fluxes, in order to update the velocity field.

3. Since the velocities obtained in Step 2 may not satisfy the continuity equation locally, a ``Poisson-type" equation for the pressure correction is derived from the continuity equation and the linearized momentum equations. This pressure correction equation is then solved to obtain the necessary corrections to the

pressure and velocity fields and the face mass fluxes such that continuity is satisfied.

4. Where appropriate, equations for scalars such as turbulence, energy, species, and radiation are solved using the previously updated values of the other variables.

5. When inter-phase coupling is to be included, the source terms in the appropriate continuous phase equations may be updated with a discrete phase trajectory calculation.

6. A check for convergence of the equation set is made.

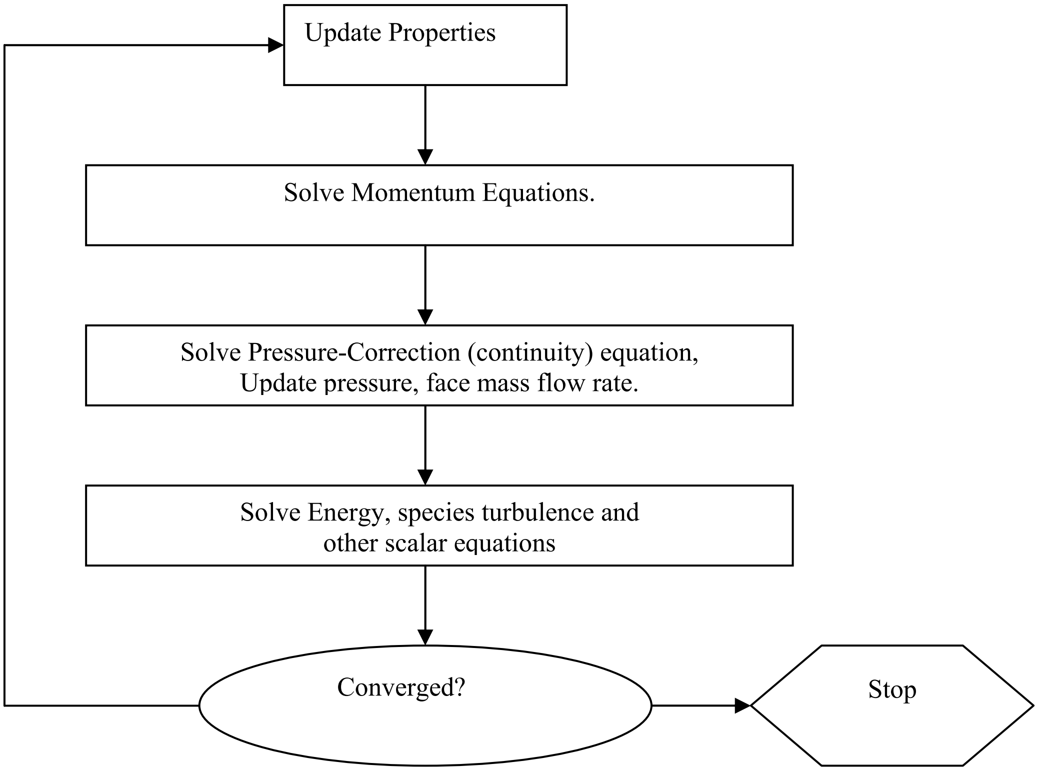

Figure 4-8: Overview of the Segregated Solution Method

These steps are continued until the convergence criteria are met.

Using the implicit solution method, for a given variable, the unknown value in each cell is computed using a relation that includes both existing and unknown values from neighboring cells. Therefore each unknown will appear in more than one equation in the system, and these equations must be solved simultaneously to give the unknown quantities.

Laminar flow of the weld material was assumed because of the large viscosity values (on the order of 10^6 Pa-s) that were found using Equation 4.1 and 4.8, leading to very small Reynolds numbers (approx. 10^{-5}) close to the pin. Due to the low Reynolds number, only viscous effects are important and inertial effects may be neglected. The material is assumed to translate past the rotating tool pin as it does in the actual experiments.

Governing Equations

FLUENT uses the solver configuration above to solve the conservation of mass, momentum (Navier-Stokes equations), and energy equations. For two-dimensional steady state incompressible fluid flow the continuity equation is

$$\frac{\partial u}{\partial x} + \frac{\partial v}{\partial y} = 0 \qquad \textbf{Eq. 4.11}$$

where x and y denote coordinates and u and v are velocity components

Neglecting gravitational and body forces, the conservation of momentum yields the following form of the Navier-Stokes equations

$$\rho u\frac{\partial u}{\partial x}+\rho v\frac{\partial u}{\partial y}=-\frac{\partial p}{\partial x}+\mu\left(\frac{\partial^2 u}{\partial x^2}+\frac{\partial^2 u}{\partial y^2}\right) \qquad \textbf{Eq. 4.12}$$

$$\rho u\frac{\partial u}{\partial x}+\rho v\frac{\partial u}{\partial y}=-\frac{\partial p}{\partial y}+\mu\left(\frac{\partial^2 v}{\partial x^2}+\frac{\partial^2 v}{\partial y^2}\right) \qquad \textbf{Eq.4.13}$$

where ρ is the density, μ is the viscosity, and p is the static pressure. The stress tensor is given by τ

$$\tau = \mu\left(\frac{\partial u}{\partial y}+\frac{\partial v}{\partial x}\right) \qquad \textbf{Eq.4.14}$$

Neglecting changes in potential energy and assuming that heat transfer obeys Fourier's law of heat conduction the steady state energy equation is written as

$$\rho C_v\left(\frac{\partial T}{\partial t}+u\frac{\partial T}{\partial x}+v\frac{\partial T}{\partial y}\right)=k\left(\frac{\partial^2 T}{\partial x^2}+v\frac{\partial^2 T}{\partial y^2}\right)+\mu\left[2\left(\frac{\partial u}{\partial x}\right)^2+2\left(\frac{\partial v}{\partial y}\right)^2+\left(\frac{\partial u}{\partial y}+\frac{\partial v}{\partial x}\right)^2\right] \qquad \textbf{Eq. 4.15}$$

where C_v is the constant volume specific heat and k is the thermal conductivity. The terms on the right hand side of Equation 4.13 represent energy transfer by conduction and viscous dissipation.

CHAPTER V

EXPERIMENTAL RESULTS AND DISCUSSION

To establish guidelines for understanding the experimental results and their anticipated consequences, some terminology will be introduced here.

The ratio of spindle speed to travel speed will be referred to as the weld pitch (w_p), and has units of revolutions per inch. The weld pitch can be increased in one of two ways; 1) increasing the tool rotational speed, or 2) decreasing the travel speed. Likewise, the weld pitch can be decreased by reducing tool rotational speed or increasing the travel speed or feed rate.

The contact condition at the tool pin can be described as sliding, sticking, or partial sliding/sticking. The experimental results will be presented with respect to the effects due to weld pitch variation. Table 5-1 lists the weld pitch for the parameter matrix in Table 3-1.

As stated in the introduction, a goal of this research is to establish guidelines for implementing FSW capable robots. A significant limiting factor when implementing FSW capable robots is the axial force requirement necessary when welding. In the experimental results to be presented here, the translational force, transverse force, axial force, and welding torque were measured for the parameter sets listed in Table 3-1. The raw data plots can be seen in Appendix A.

Table 5-1: VU FSW Experimental Parameter matrix Weld Pitch.

Feed Rate (ipm)

Spindle Speed (RPM)	11.4	27	37.2	44.8	53.3	63.3
1500	132	56	40	33	28	24
2250	175*	83	60	50	42	36
3000	219**	111	81	67	56	47
3750	-	139	101	84	70	59
4500	-	-		100	84	71

*Actual Rotational Speed was 2000 RPM
** Actual Rotational Speed was 2500 RPM

Axial Force (Fz)

The axial force was measured for the weld parameter sets shown in Table 5-1. The raw data plots can be seen in Appendix B. The steady state axial force is presented in the following figures as the average axial force during the weld. Each weld parameter set was run a minimum of two times in order to verify the precision of the force data. The steady state axial force was found by averaging the mean axial force of each run of a weld parameter. Figures 5-1 and 5-2 show the steady state axial force for variable rotational speed and travel speed, respectively. From Figure 5-1, it can be seen that the axial force decreases as the rotational speed increases.

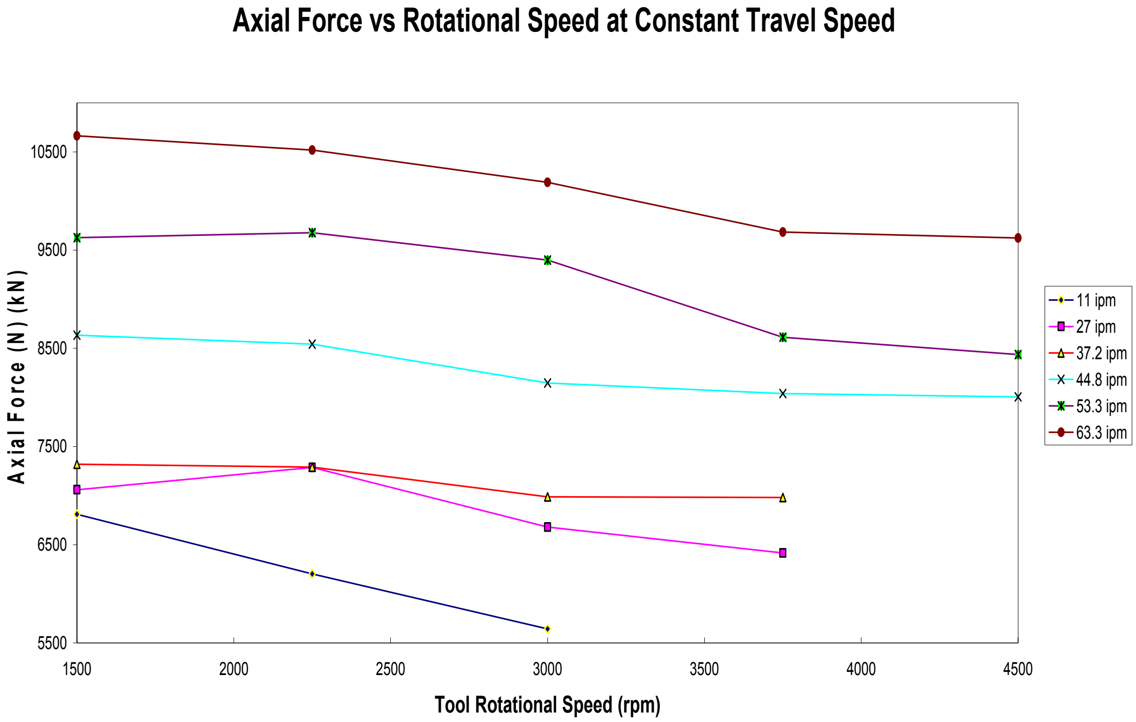

Figure 5-1: Axial Force vs. Rotational Speed for constant travel speeds.

Increasing the rotational speed and holding the travel speed constant leads to a decrease in axial force. Increasing the travel speed and holding the rotational speed constant leads to an increase in axial force. The decrease in axial force for increasing weld pitch through increased rotational speed is shown in Table 5-2.

Table 5-2: Percentage Decrease in Axial Force for Increasing Weld Pitch by increasing Rotational Speed

TS (ipm)	Min w_p (rpi)	Max w_p (rpi)	% F_z Decrease
11.4	131.6	219.3	17.1
27.0	55.6	138.9	9.1
37.2	40.3	100.8	4.6
44.8	33.5	100.4	7.3
53.3	28.1	84.4	12.4
63.3	23.7	71.1	9.8

Figure 5-2 shows the axial force for various travel speeds at constant rotational speeds. Table 5-3 shows the percentage decrease in axial force for increasing weld pitch by decreasing the travel speed.

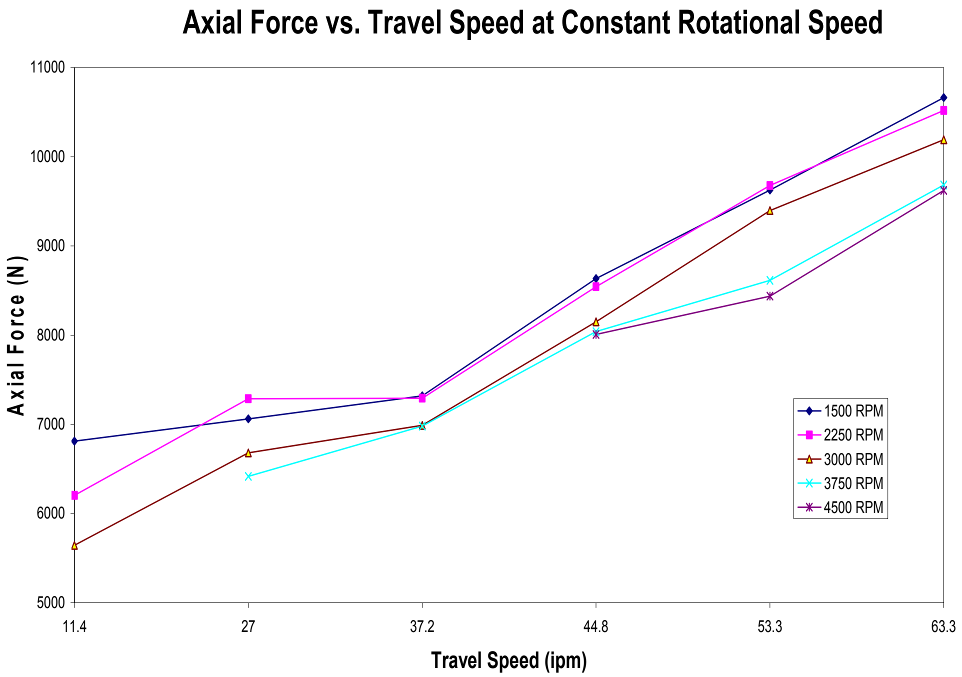

Figure 5-2: Axial Force vs. Travel Speed for constant rotational speed.

Table 5-3: Percentage Decrease in Axial Force for Increasing Weld Pitch by reducing Travel Speed

RS (ipm)	Min w_p (rpi)	Max w_p (rpi)	% F_z Decrease
1500	23.7	131.6	36.1
2250	35.5	197.4	41.0
3000	47.4	263.2	44.6
3750	59.2	138.9	33.7
4500	71.1	100.4	16.8

Welding Torque

The effect of weld pitch variation on the welding torque is key to understanding the friction stir welding process and successfully implementing FSW capable robots. The torque was measured for the weld parameter sets shown in Table 5-1. The raw data plots can be seen in Appendix B.

The steady state torque is presented in Figures 5-3 and 5-4. The steady state welding torque is found by averaging the mean torque each run of a weld parameter set. Figures 5-3 and 5-4 show the steady welding torque for variable rotational speed and travel speed respectively. Tables 5-4 and 5-5 show the percentage decrease in torque from increasing weld pitch.

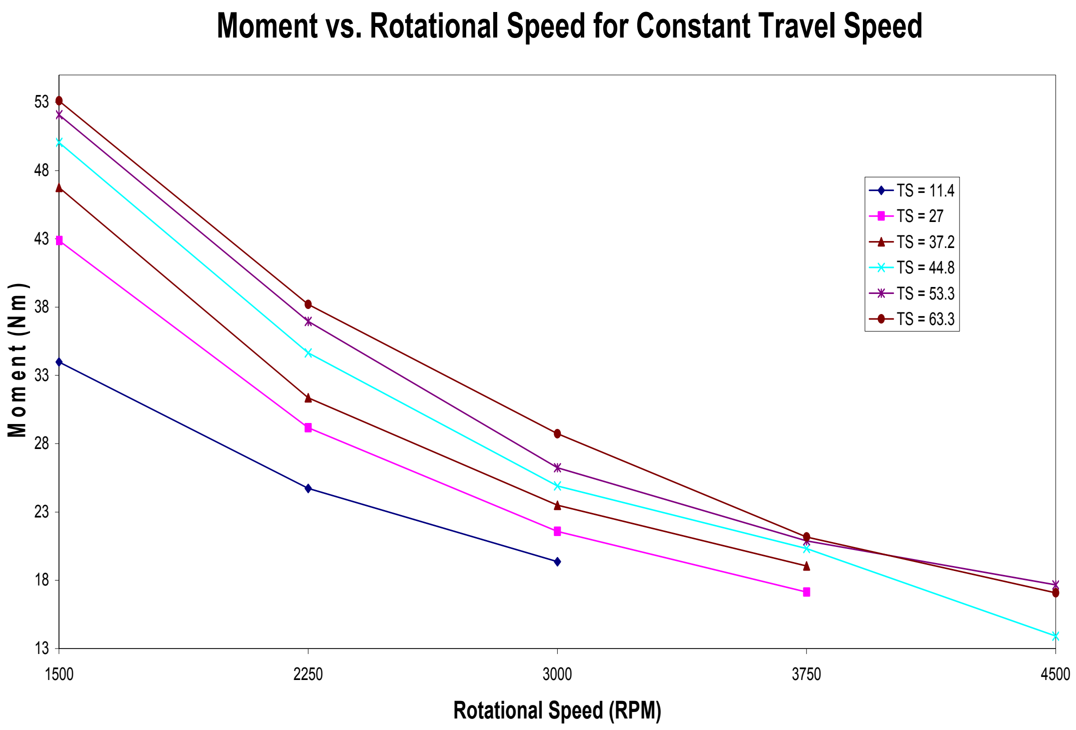

Figure 5-3: Torque vs. Rotational Speed for constant travel speed.

Table 5-4: Percentage Decrease in Torque for Increasing Weld Pitch by increasing Rotational Speed

TS (ipm)	Min w_p (rpi)	Max w_p (rpi)	% M_z Decrease
11.4	131.6	219.3	45.9
27.0	55.6	138.9	60.0
37.2	40.3	100.8	59.3
44.8	33.5	100.4	72.2
53.3	28.1	84.4	66.1
63.3	23.7	71.1	67.9

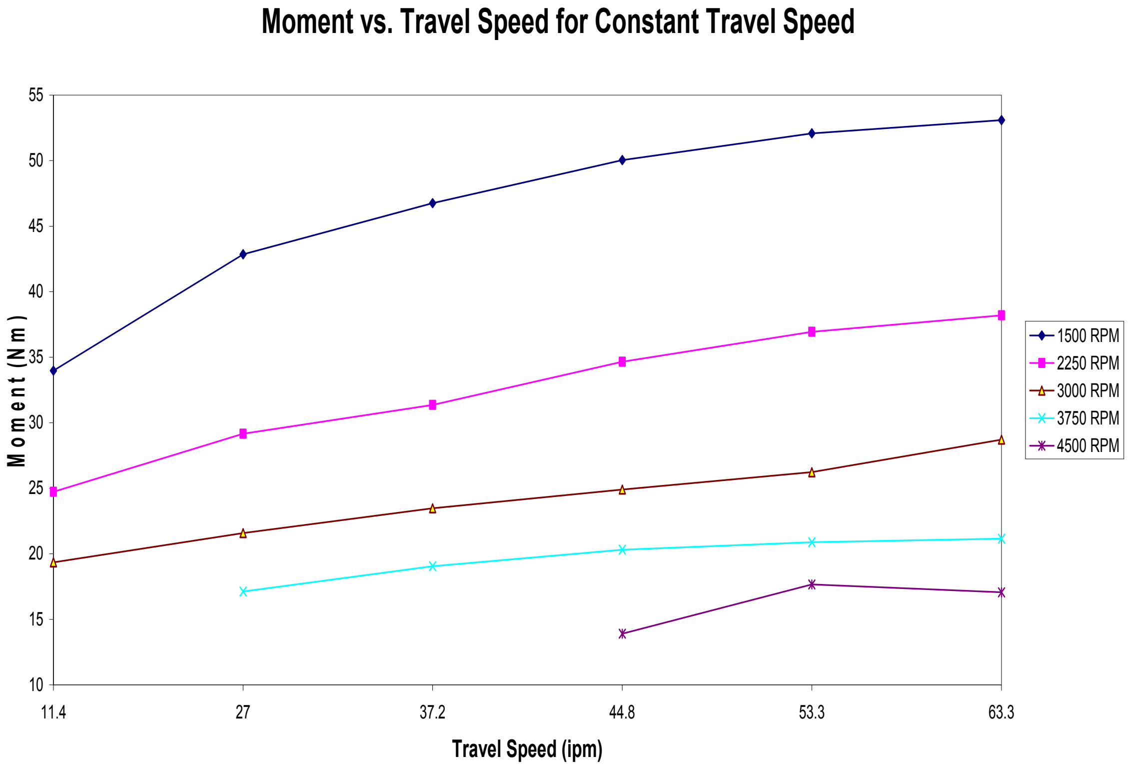

Figure 5-4: Torque vs. Travel Speed for constant rotational Speed.

Increasing the rotational speed while holding the travel speed constant leads to a decrease in torque; while increasing the travel speed and holding the rotational speed constant leads to an increase in torque. The decrease in torque for increasing weld pitch through reduced travel speed is shown in Table 5-5.

Table 5-5: Percentage Decrease in Torque for Increasing Weld Pitch by reducing Travel Speed

TS (ipm)	Min w_p (rpi)	Max w_p (rpi)	% M_z Decrease
1500.0	23.7	131.6	36.0
2250.0	35.5	197.4	35.3
3000.0	47.4	263.2	32.6
3750.0	59.2	138.9	19.1
4500.0	71.1	100.4	18.5

The welding power is shown in Figure 5-5 and appears to remain nearly constant for a constant travel speed.

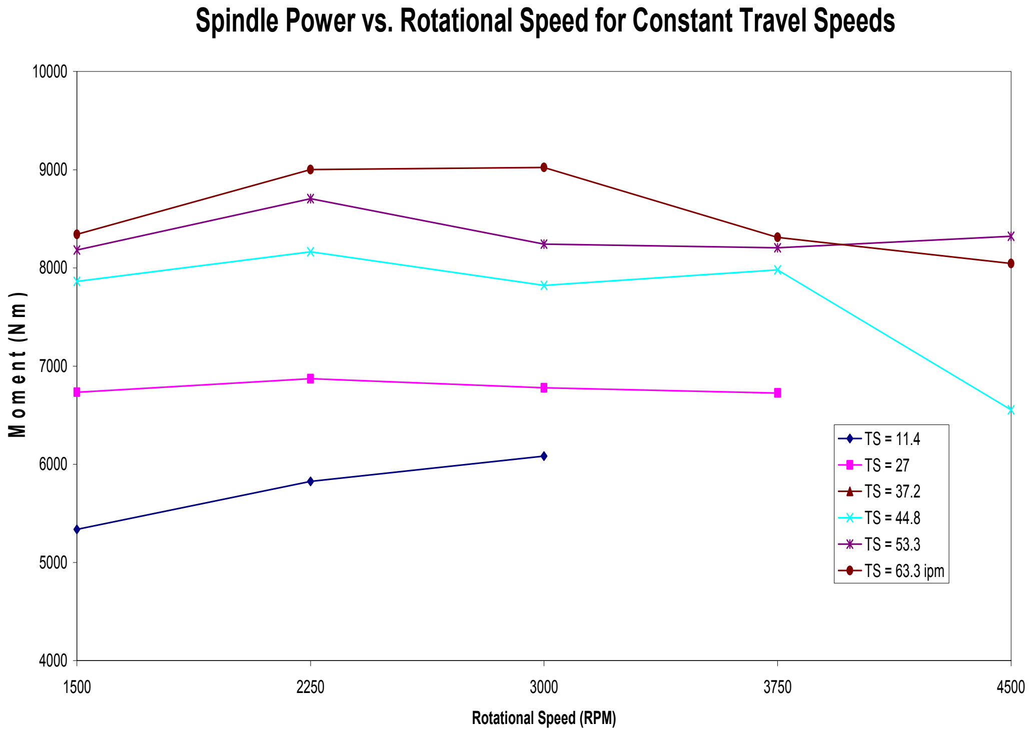

Figure 5-5: Spindle Power vs. Rotational Speed for constant travel speed.

Translational and Transverse Force

The translational and transverse forces were measured for the weld parameter sets shown in Table 5-1. The steady state translational and transverse forces are presented in the following figures as the average force (Fx or Fy) during a weld. Each weld parameter set was run a minimum of two times in order to verify the precision of the force data. The steady state translational or transverse force is found by averaging the mean translational or transverse force of each parameter set. Figures 5-7 and 5-8 show the steady state translational and transverse force for variable rotational speed respectively.

From Figures 5-6 and 5-7, it is apparent that the translational and transverse forces have the general trend of decreasing with increased weld pitch, but not with the linear trend as the axial force and torque follow.

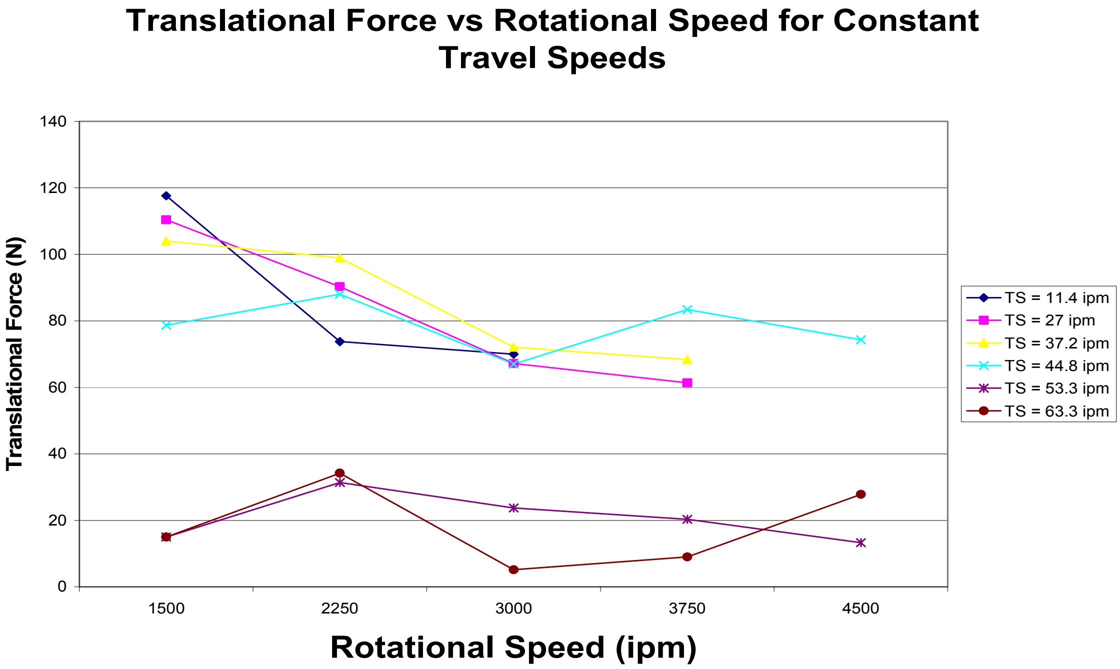

Figure 5-6: Translational Force vs. Rotational Speed for constant travel speed.

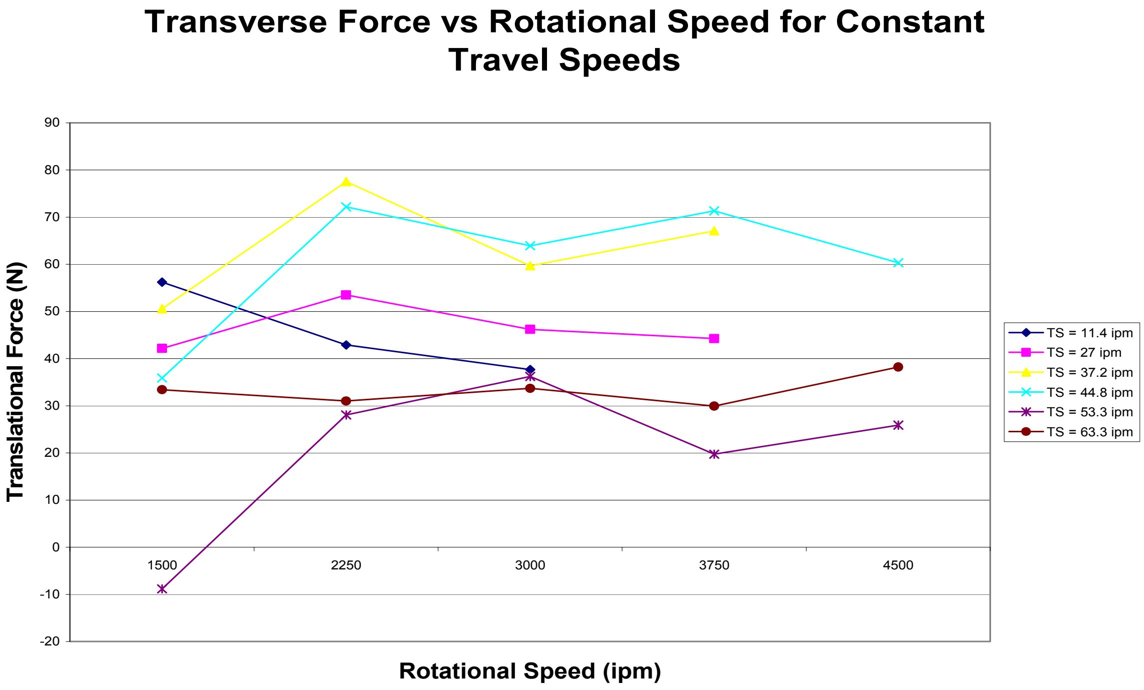

Figure 5-7: Transverse Force vs. Rotational Speed for constant travel speed.

The steady state plots of the translational and transverse forces follow the general parametric relationship of increased rotational speed/ decreased force, however as the rotational speed is increased, a new relationship becomes apparent.

Viewing the raw data plots gives insight into the force behavior at higher rotational speeds. Figures 5-8 and 5-9 show the raw data plots of the translational and transverse force for various rotational speeds and 44 ipm travel speed. Increasing the rotational speed for a constant travel speed creates a varying contact condition at the tool pin/material interface.

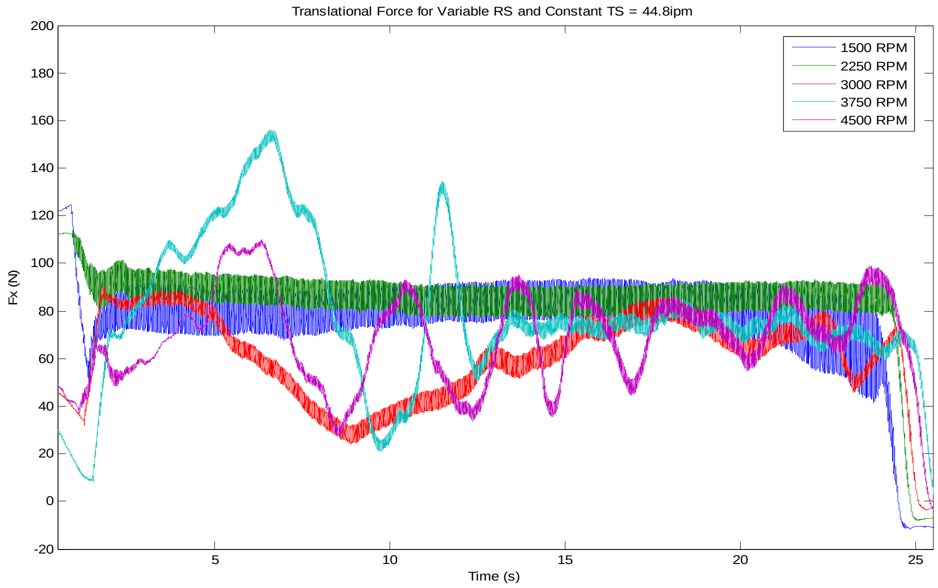

Figure 5-8: Raw data plot of Translational Force for various RS and TS = 44 ipm.

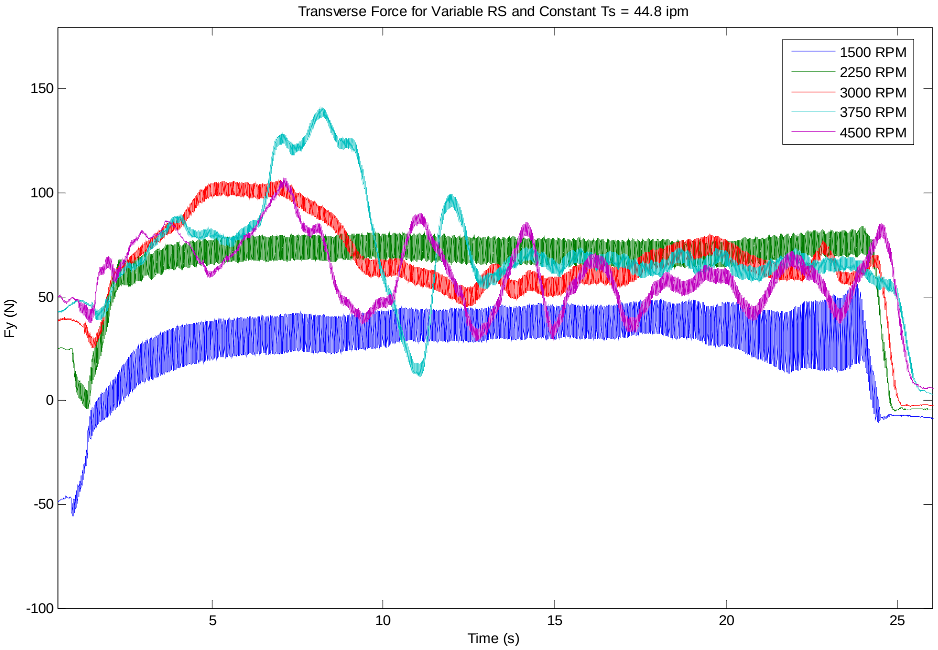

Figure 5-9: Raw data plot of Transverse Force for various RS and TS = 44 ipm.

In Figures 5-9 and 5-10, the translational and transverse forces are constant lines of force for wp < 50.2 rpi and oscillates for wp > 50.2 rpi. The constant lines of force indicate a constant pressure at the tool pin/material interface. The oscillation indicates that the material at the tool pin/material interface does not apply constant pressure but rather it sticks to the tool and drags along behind the tool as it rotates.

With the sticking contact condition, if the friction shear stress exceeds the yield shear stress, the weld material at the tool/material interface will stick to the moving tool surface segment. In this case, the matrix segment will accelerate along the tool surface (finally receiving the tool velocity), until an equilibrium state is established between the contact shear stress and the internal matrix shear stress. At this point, the stationary full sticking condition is fulfilled [41].

For the sliding condition, if the contact shear stress is smaller than the internal matrix yield shear stress, the matrix segment volume shears slightly to a stationary elastic deformation, where the shear stress equals the ‘dynamic’ contact shear stress. This state is referred to as the sliding condition [41].

The partial sliding/sticking contact condition is a mixed state of the two contact conditions. In this case, the matrix segment accelerates to a velocity less than the tool surface velocity, where it stabilizes. The equilibrium occurs when the ‘dynamic’ contact shear stress equals the internal yield shear stress due to a quasi-stationary plastic deformation rate [41].

The variation of the contact condition can reasonably be assumed to be induced by increasing the rotational speed. Increasing the rotational speed causes a corresponding increase in welding temperature. The over-heat phenomena (discussed in Chapter 3) that occurred at certain welding parameter sets was always preceded by a sliding/sticking contact condition for the lower weld pitch parametric set (rotational speed and travel speed).

The raw data plots in Appendix B show that the contact condition is sliding for wp < 50.2 rpi, and that the force is due to a pressure. For the for wp > 50.2, the contact condition would appear to be sliding/sticking and the force on the pin is due to visco-plastic drag of the weld material.

Understanding these conditions is key developing a three dimensional model capable of predicting the forces and torques during FSW for various weld pitches and tool geometries. Chapter 6 details the results of the two dimensional fluid flow model discussed in Chapter 4 and is compared to the experimental results presented here.

CHAPTER VI

2-D MODELING RESULTS AND DISCUSSION

It will be useful now to identify the limiting factors for implementation of FSW capable robots. The primary limiting factor is the large axial force required.

The axial force was found to decrease by either increasing rotational speed or decreasing travel speed. An increase in rotational speed decreases the axial force by increasing the heat input into the weld material, thus raising the temperature of the weld material. Reducing the travel speed increases the number of revolutions per unit length of the weld, which increases the heat input per unit length of the weld.

Table 3-3 shows that increasing the temperature of the weld material from 38ºC to 371ºC decreases the yield strength from 241 MPa to 12 MPa, a 95% decrease. Therefore the optimum weld pitch for FSW will occur at high rotational speeds and low travel speeds.

Another potential limiting factor is the welding torque. The welding torque is largely governed by the weld pitch as well as the tool geometry. Increasing the size of the tool pin and particularly the tool shoulder, causes a corresponding increase in welding torque. Increasing the rotational speed increases the temperature of the weld material, decreasing the yield strength, which decreases the torque required to displace the weld material to facilitate forward travel of the tool. As stated earlier, reducing the travel speed increases the heat input to the weld, and reduces the yield strength, which reduces the required torque.

A significant goal of this research is to establish practical design guidelines for developing FSW capable robots. Developing a 3-D model capable of predicting the forces and torques associated with FSW would greatly aide the ability of scientists and engineers to design, fabricate, and implement FSW capable robots.

In this thesis, a two dimensional model was developed to predict the translational force, welding torque, and temperature on the tool pin for parameter sets listed in Table 5-1. All simulations were run using the computational fluid dynamics package FLUENT. Chapter 4 details the determination of the material properties, boundary conditions, mechanical modeling, thermal modeling, solver configuration and governing equations.

Welding Torque

Friction stir welding is a three dimensional process. In this thesis, the initial modeling efforts are represented in 2-D. Though a 2-D model cannot fully represent a 3-D process, if implemented correctly, the 2-D model may suggest the general trends of the 3-D process.

As stated in Chapter 4, the tool is represented by a 2-D rotating pin. In order for the torque experimental results to be compared with the numerical model, the experimental results must be scaled to represent the contribution of the pin during welding. The rotating plug model suggested by Nunes et al. [26] was used to determine the pin contribution.

With the rotating plug model, the tool torque is taken to be totally due to the shear flow stress of the metal acting perpendicular to the direction of tool rotation and integrated over the surface. The tool torque is given by

$$M_z = \int_{Rp}^{Rs} 2\pi R_p \sigma dR_p + 2\pi R_p^2 t\sigma + \int_0^{Rp} 2\pi R_p^2 \sigma dR_p, \qquad \textbf{Eq. 6.1}$$

where R_p is the pin radius, R_s is the shoulder radius, σ is the shear flow stress, and t is the pin depth. The three terms in Equation 6.1 are the contributions to the torque from the tool shoulder, pin sides, and pin bottom respectively. Applying Equation 6.1 to the experimentally measured steady state welding torque, the shear stress was computed for each parameter set in Table 5-1, and can be seen in Table 6-1.

Table 6-1: Computed Shear Stress using the rotating plug model.

Feed Rate (ipm)

RPM	σ (Pa) @ 11.4	σ (Pa) @ 27	σ (Pa) @ 37.2	σ (Pa) @ 44.8	σ (Pa) @ 53.3	σ (Pa) @ 63.3
1500	7.92E+07	4.92E+08	5.58E+08	6.56E+08	7.80E+08	9.21E+08
2250	5.14E+07	1.35E+08	2.84E+08	3.13E+08	3.67E+08	4.58E+08
3000	2.63E+07	5.80E+07	1.15E+08	1.68E+08	2.34E+08	2.90E+08
3750		4.12E+07	6.19E+07	1.05E+08	1.47E+08	1.56E+08
4500				5.07E+07	8.97E+07	9.38E+07

From Equation 6.1, we see that the torque contribution from the pin side is

$$M_z = 2\pi R_p^2 t\sigma. \qquad \textbf{Eq. 6.2}$$

Now, substituting the shear stress from Table 6-1 into Equation 6.2, M_p is found for the corresponding parameter sets and can be seen in Table 6-2.

Table 6-2: Torque Contribution by the Tool Pin.

Feed Rate (ipm)

RPM	M_p (N-m) @ 11.4	M_p (N-m)@ 27	M_p (N-m) @ 37.2	M_p (N-m) @ 44.8	M_p (N-m) @ 53.3	M_p (N-m) @ 63.3
1500	8.3	10.4	11.4	12.2	12.7	12.9
2250	6.0	7.1	7.6	8.4	9.0	9.3
3000	4.7	5.3	5.7	6.1	6.4	7.0
3750	-	4.2	4.6	5.0	5.1	5.2
4500	-	-	-	3.4	4.3	4.2

Dividing M_p /M_z for the corresponding parameter sets show that the pin torque contribution is approximately 24.9%.

The simulations were run for the Couette Flow and Visco-Plastic Flow viscosity models. The simulation determined the shear stress at the pin wall, which was then input into Equation 6-2 to determine the moment (welding torque) of the pin. Figures 6-1 through 6-6 show a comparison of the predicted simulation results to the experimental pin torques for various weld pitches.

At low weld pitches, the Couette Flow model did not correlate very well with the experimental results. As the weld pitch increases, the experimental results and the Couette Flow model begin to converge. This implies that the Coutte Flow model is more predictive for very high weld pitches. At high weld pitches, the high heat input greatly improves the weld material's ability to flow. In general, the torque decreases as weld pitch is increased.

Overall, the Visco-Plastic flow model was more accurate than the Couette Flow model over the range of weld pitches. The Visco-Plastic Flow model also converged with the experimental results as the weld pitch was increased.

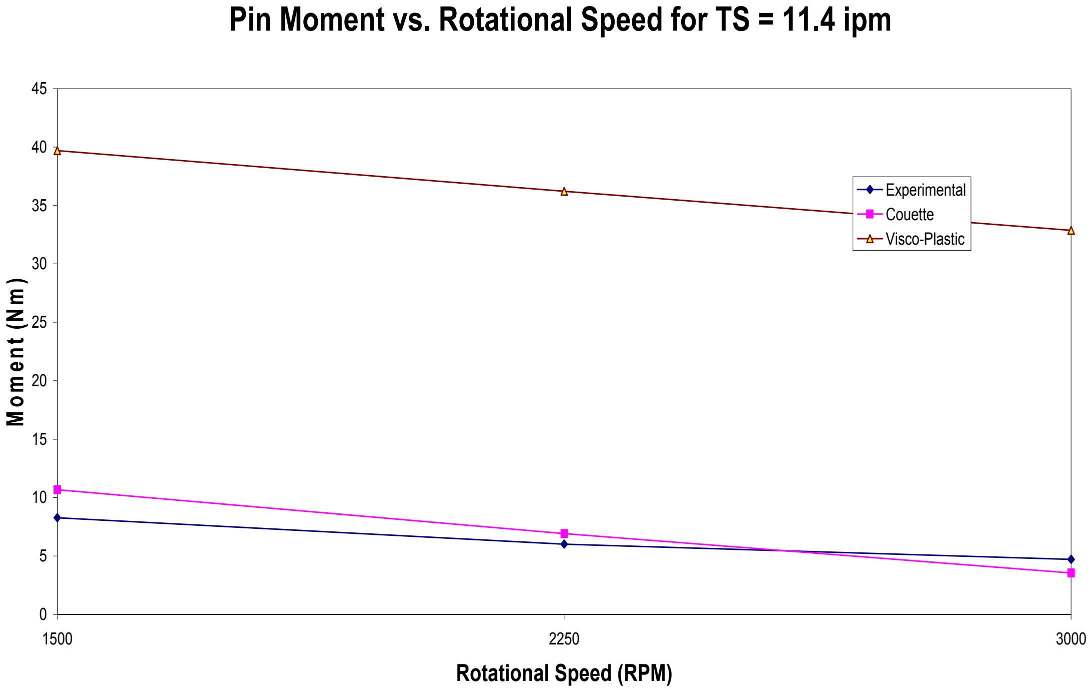

Figure 6-1: Comparison of Predicted and Experimental Pin Moment vs. Rotational Speed for 11.4 ipm

In Figure 6-1, the Couette Flow model correlates very well for the 11.4 ipm travel speed. The weld pitch at this travel speed was very high for all rotational speeds. Lending further credibility to the theory that Couette Flow is more optimal for high weld pitches.

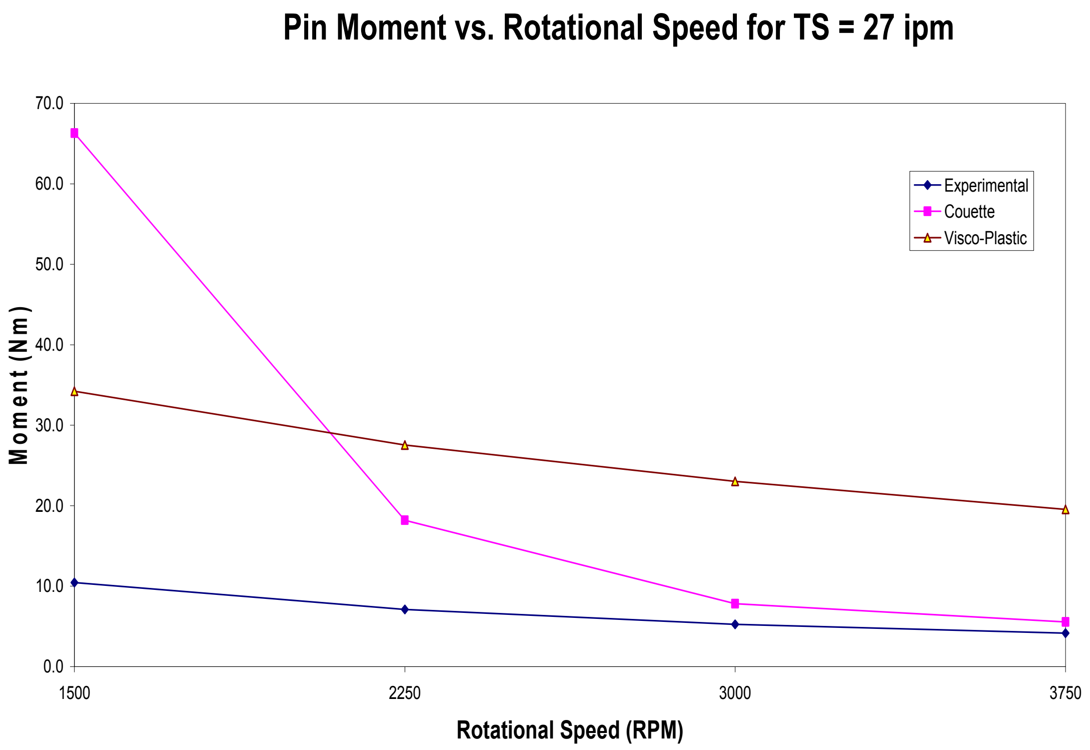

Figure 6-2: Comparison of Predicted and Experimental Pin Moment vs. Rotational Speed for 27 ipm

At approximately 2300-2400 rpm, the Couette Torque and Experimental torque are almost equal. The corresponding weld pitch is 202- 210 rpi. In Figures 6-2 through 6-6, the Couette torque is never less than the experimental torque, likewise, the weld pitch is not higher than 200 rpi for the following plots

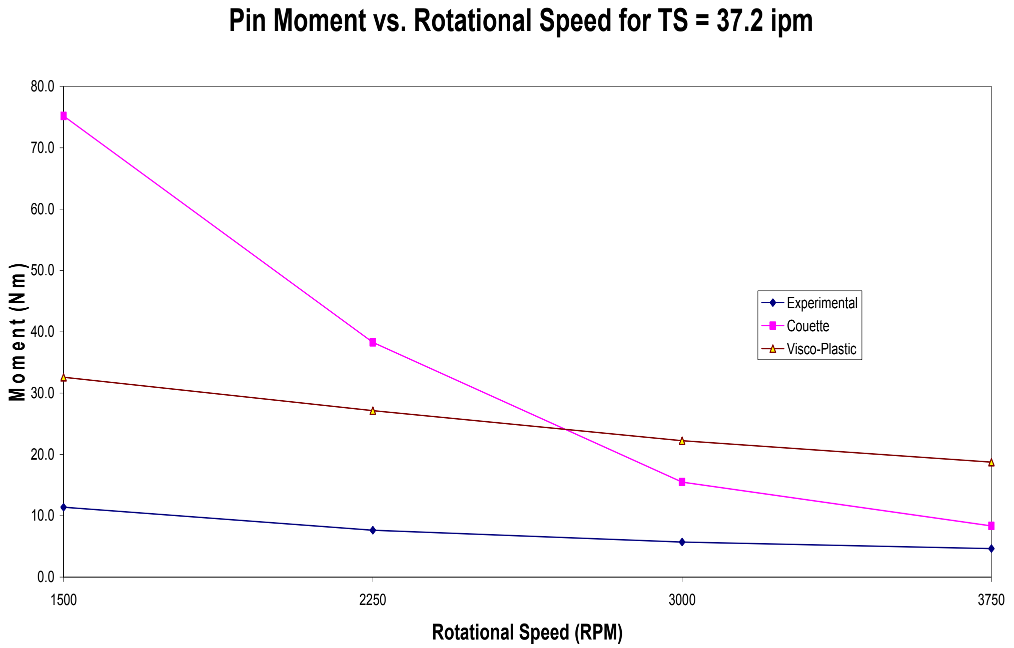

Figure 6-3: Comparison of Predicted and Experimental Pin Moment vs. Rotational Speed

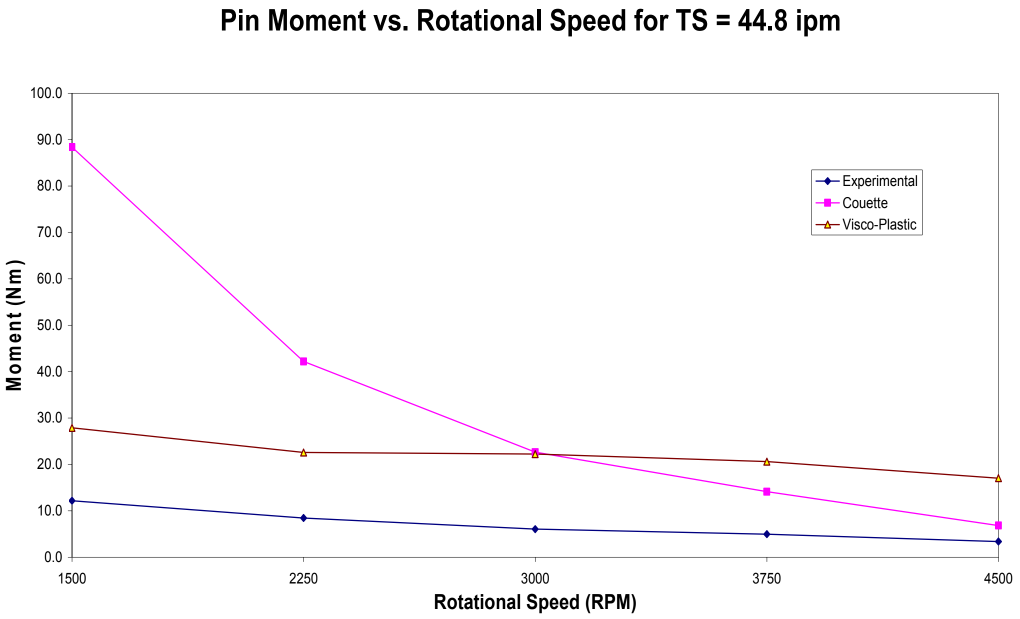

Figure 6-4: Comparison of Predicted and Experimental Pin Moment vs. Rotational Speed for 44.8 ipm

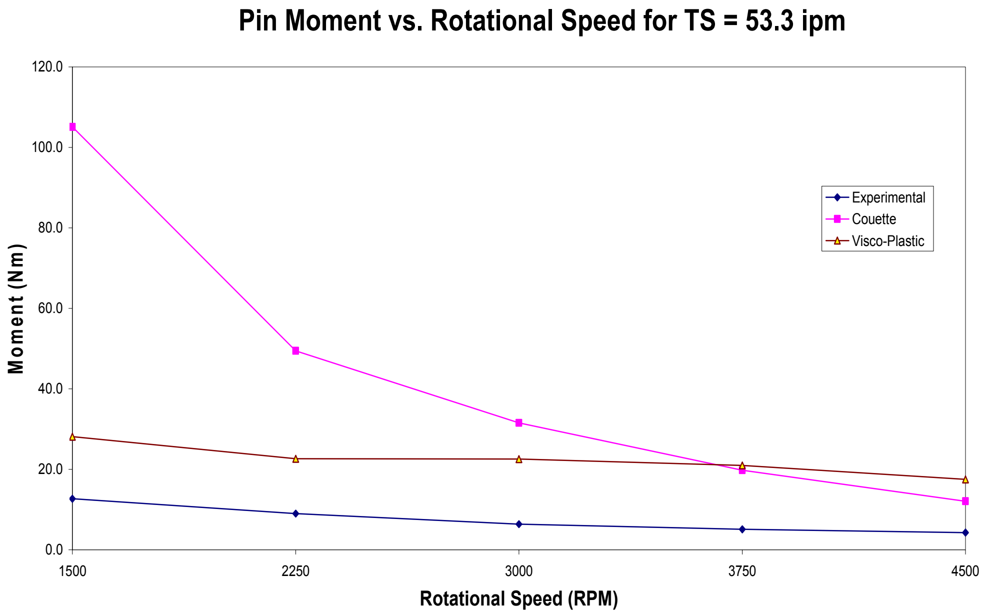

Figure 6-5: Comparison of Predicted and Experimental Pin Moment vs. Rotational Speed for 53.3 ipm

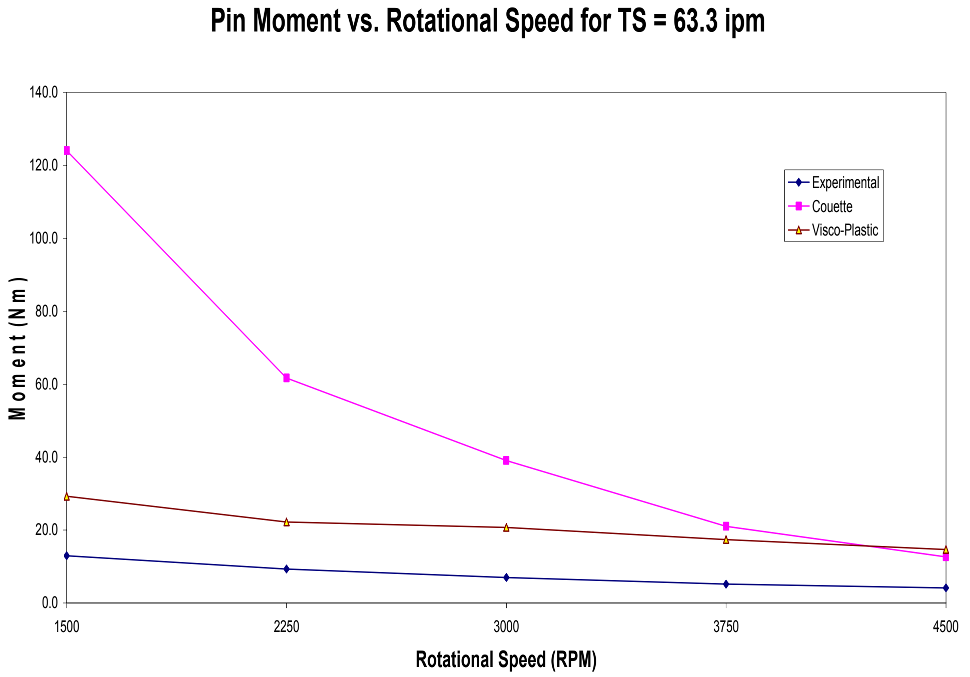

Figure 6-6: Comparison of Predicted and Experimental Pin Moment vs. Rotational Speed for 63.3 ipm

Translational Force

Figures 6-7 through 6-12 show the comparison of the experimental translational force to the predicted translational forces for the Couette Flow and the Visco-Plastic flow model. In general the results follow the increased rotational speed/decreased force relationship.

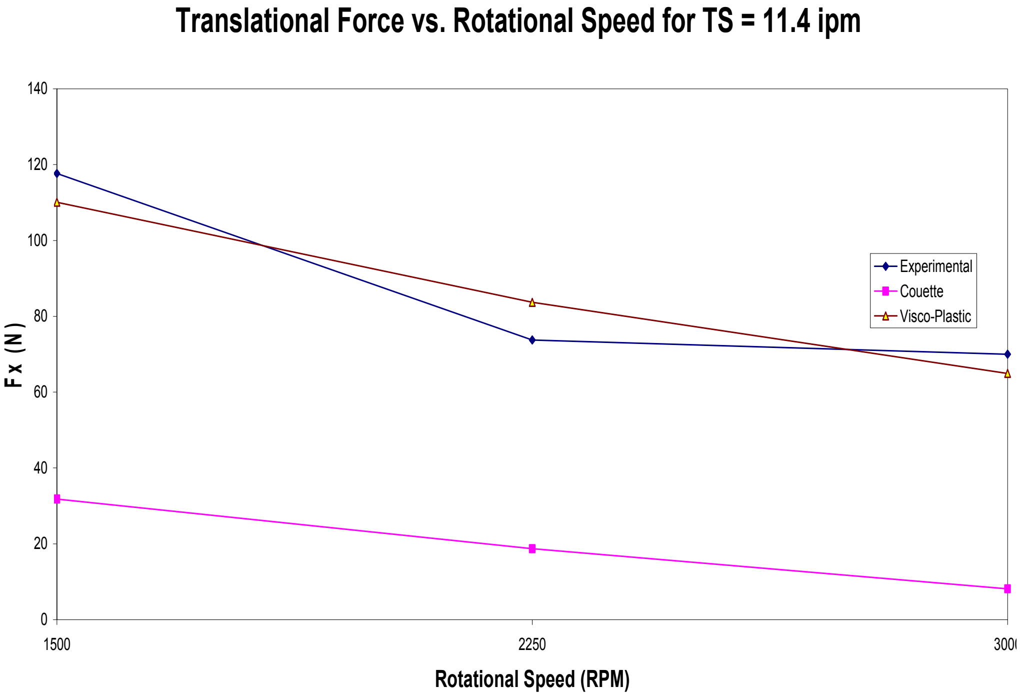

Figure 6-7: Comparison of Predicted and Experimental Translational Force vs. Rotational Speed for 11.4 ipm.

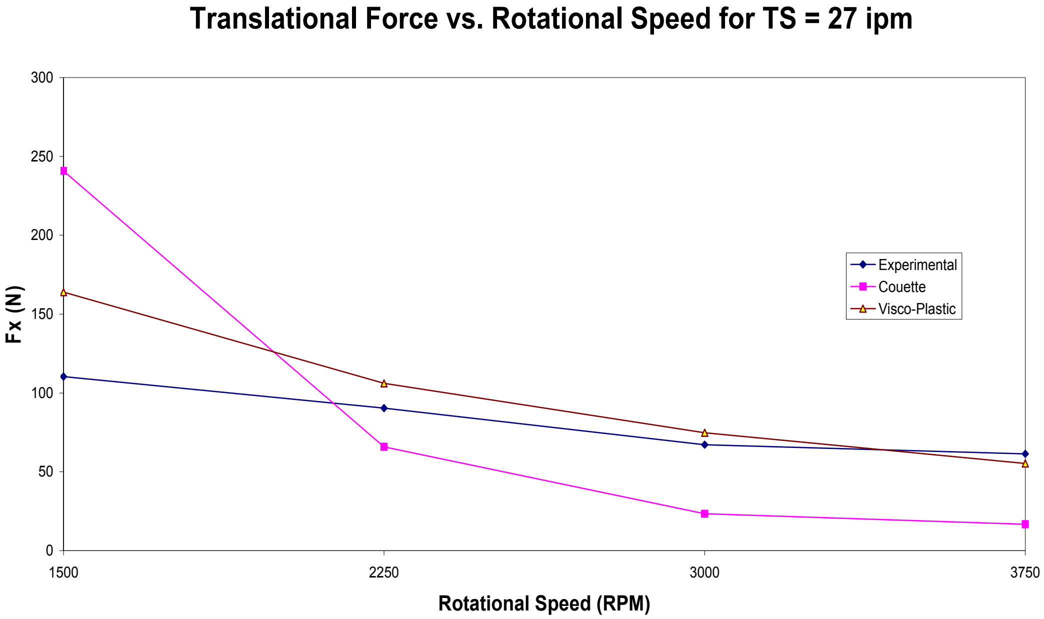

Figure 6-8: Comparison of Predicted and Experimental Translational Force vs. Rotational Speed for 27 ipm.

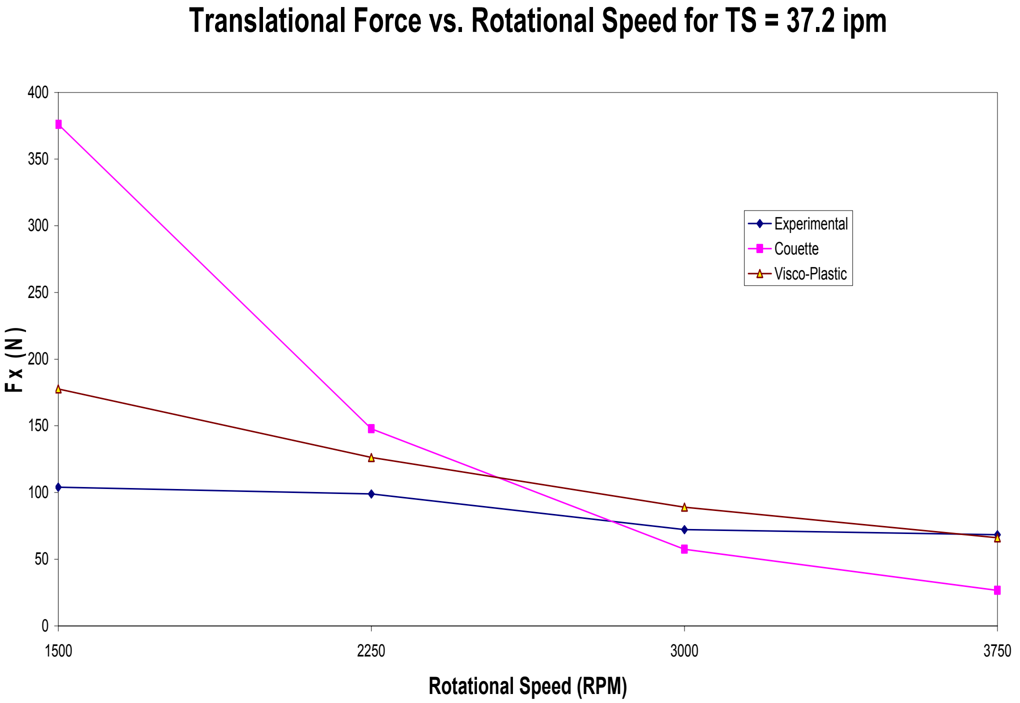

Figure 6-9: Comparison of Predicted and Experimental Translational Force vs. Rotational Speed for 37.2 ipm.

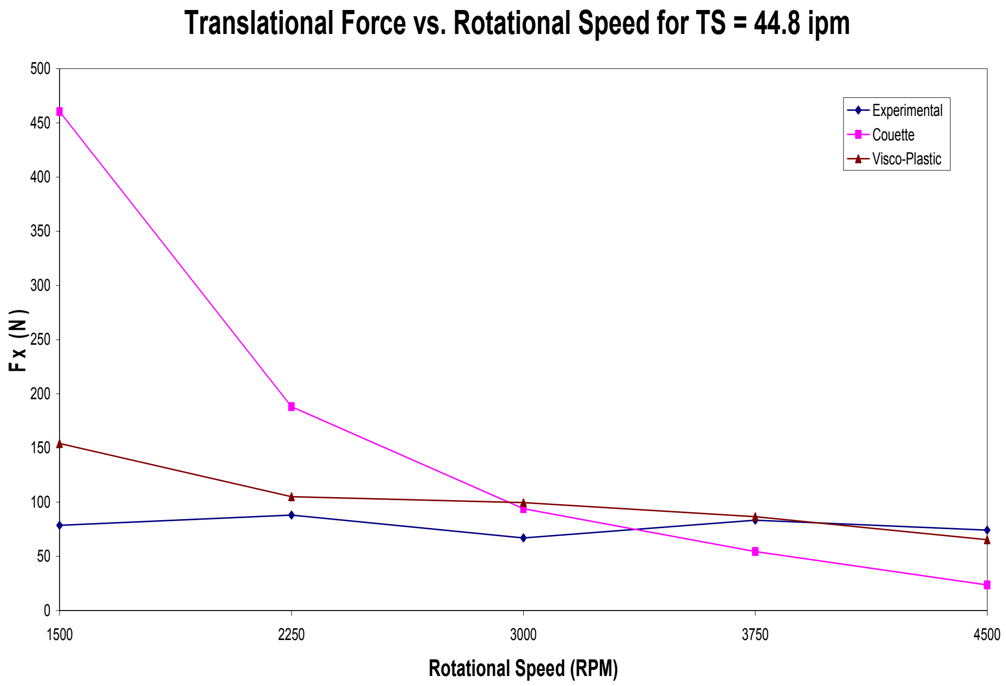

Figure 6-10: Comparison of Predicted and Experimental Translational Force vs. Rotational Speed for 44.8 ipm.

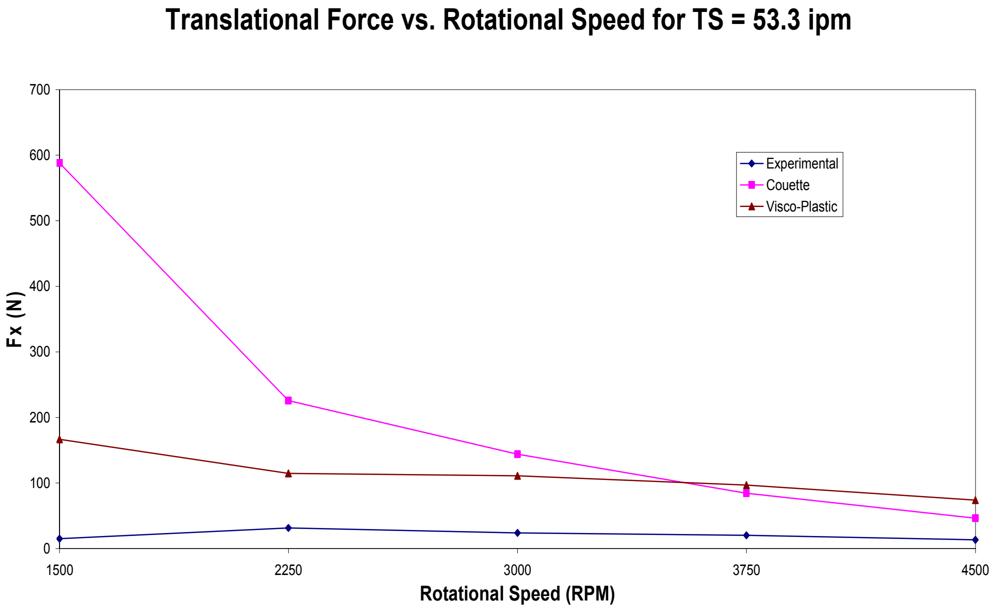

Figure 6-11: Comparison of Predicted and Experimental Translational Force vs. Rotational Speed for 53.3 ipm.

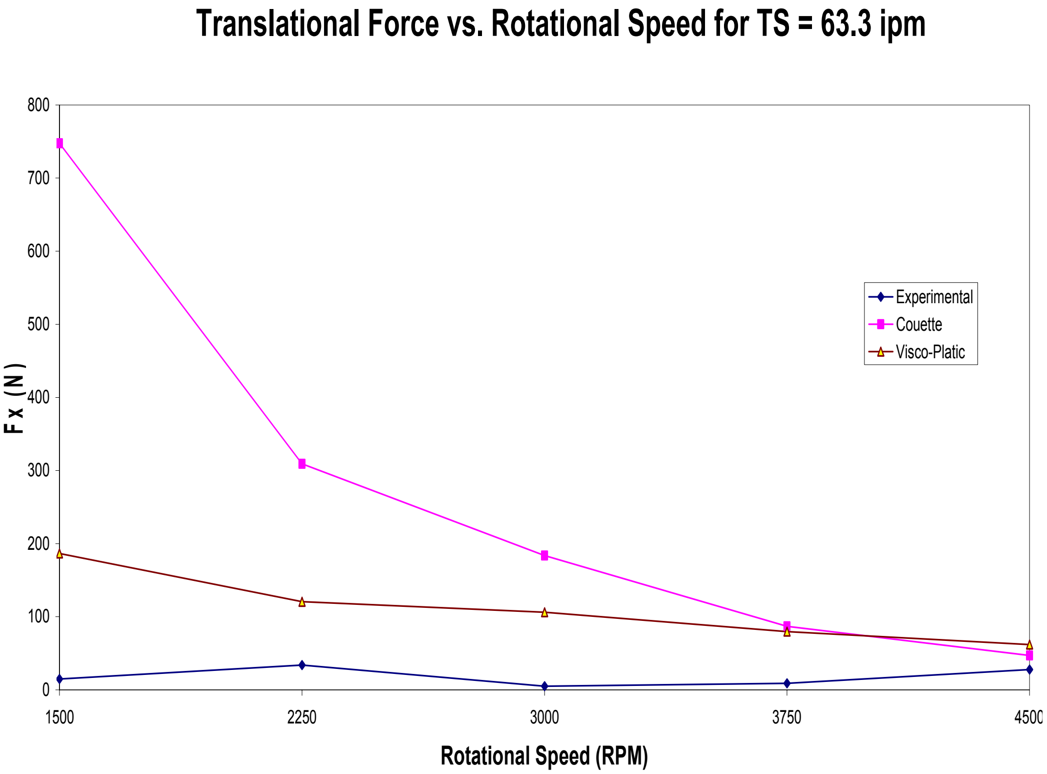

Figure 6-12: Comparison of Predicted and Experimental Translational Force vs. Rotational Speed for 63.3 ipm

The trend for the translational force seems to match the weld torque where the Coutte Flow model is more accurate for very high weld pitches and the Visco-Plastic flow model was more precise than the Couette Flow model over the range of weld pitches.

Temperature Predictions

Figures 6-13 show the predicted temperature of the weld material at the tool pin/material interface. The difference in temperature for the Couette Flow Model and the Visco-Plastic flow model were less than 1% for the various weld pitches. Figure 6-13 shows that the temperature increases as the tool rotational speed increases. This further supports the observation that the axial force decreases with increased rotational speed because the weld material temperature is higher and decreases the yield strength. The maximum predicted temperature is shown to occur at the highest rotational speed (4500 rpm), while the lowest temperature occurs at the lowest rotational speed of 1500 rpm.

Figure 6-14 shows the effect of travel speed on the weld temperature. The predicted temperature decreases as the travel speed is increased.

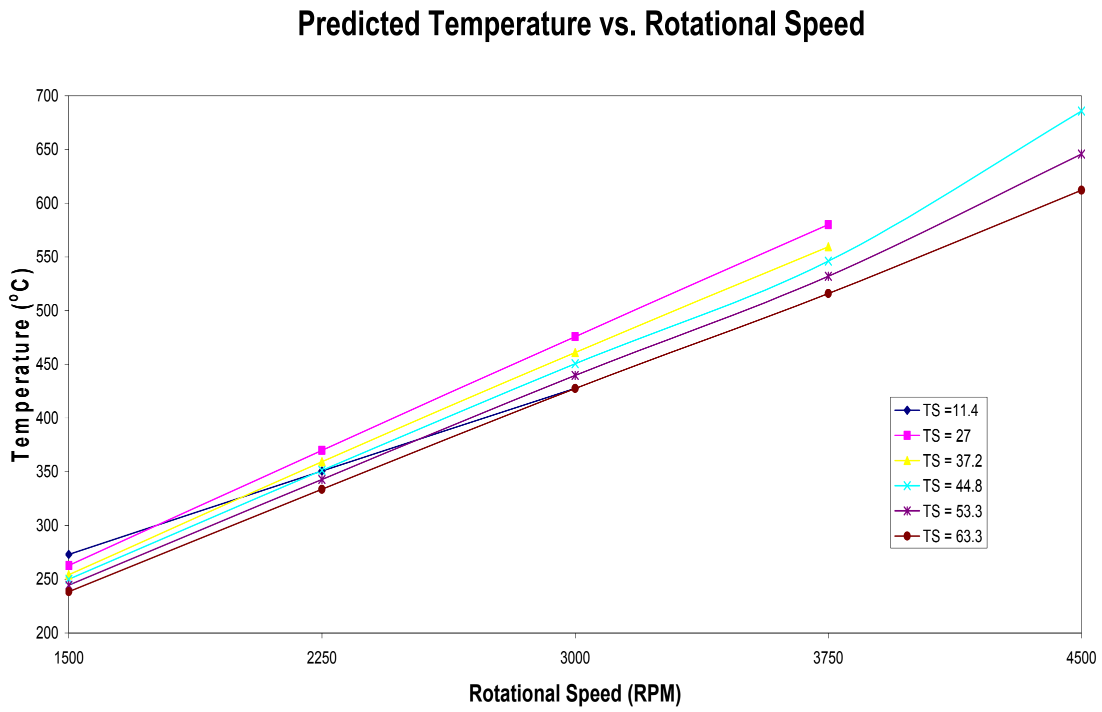

Figure 6-13: Predicted Temperature vs. Rotational Speed for Constant Travel Speed.

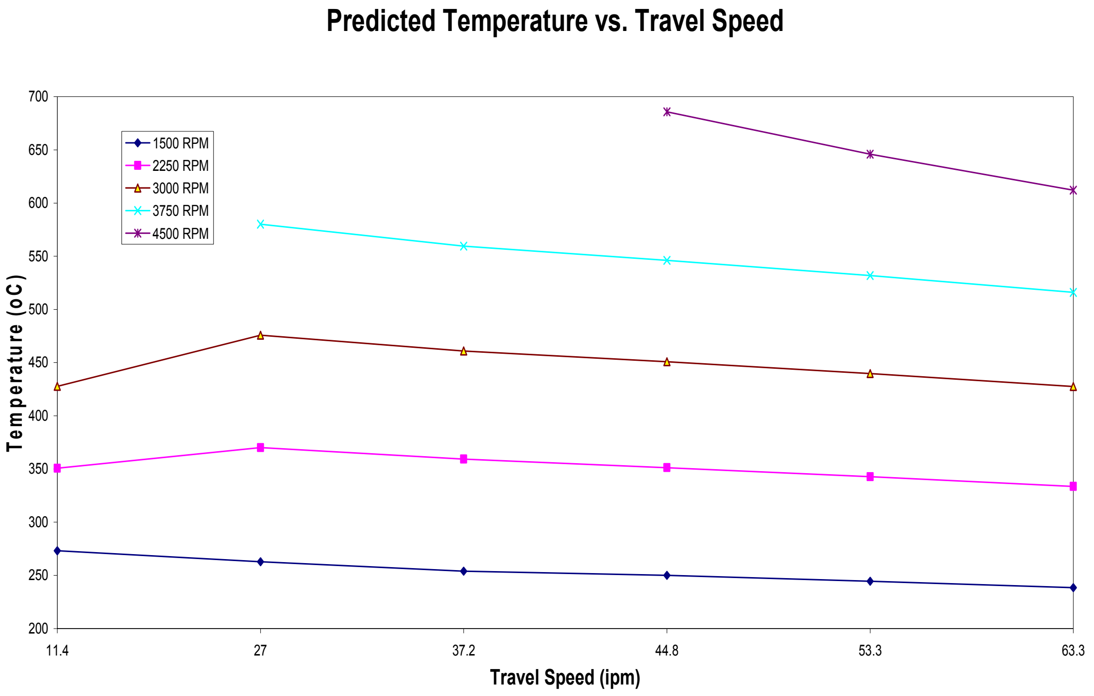

Figure 6-14: Predicted Temperature vs. Travel Speed for Constant Rotational Speed.

The predicted temperatures at 4500 rpm seem high. One possible reason is because the contact condition at the tool pin material interface was assumed to be sticking, while the experiments that the contact condition is partial sliding/sticking. More experimentation at increased temperatures is necessary to improve the analysis. The heat generation model used in this simulation has provisions for different contact conditions at the tool pin/material interface. Future research will involve modifying the contact condition used for determining the heat input during welding.

The steady state welding temperature was not measured during the experiment. Therefore there is no way at this time to validate the predicted temperatures. However, the results correlate well with the weld temperatures (up to 547 ºC) predicted by Song et al. [44]. Similar temperatures were predicted by Sato et al. for Al 6063[18], which is similar to Al 6061 in chemical composition and physical properties [44].

Figures 6-15, 6-16, and 6-17 show plots of the weld material temperature gradients for 1500 rpm / 11.4 ipm, 2000 rpm / 11.4ipm, and 2500 rpm/11.4 ipm. As can be seen in Figures 6-15 and 6-16, the contour plots of temperature profile are similar for each parameter set. Therefore only the pin temperatures are presented here and can be seen in Figure 6-13.

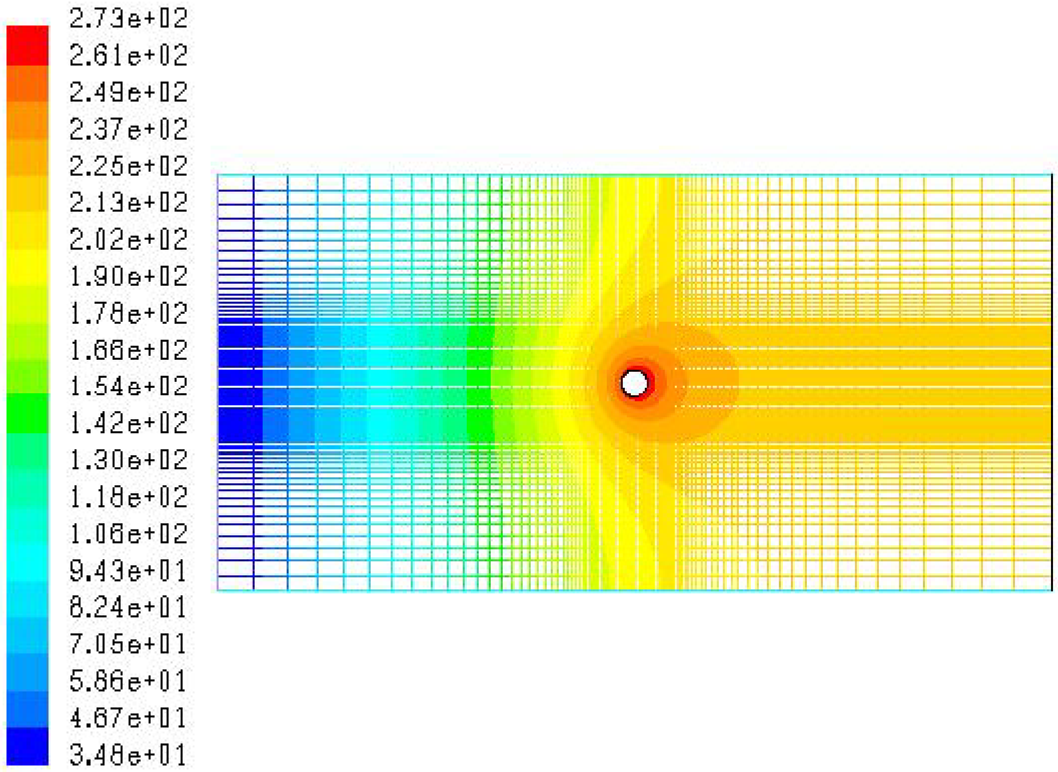

Figure 6-15: Temperature Contour Plot for 1500 RPM and 11.4 ipm.

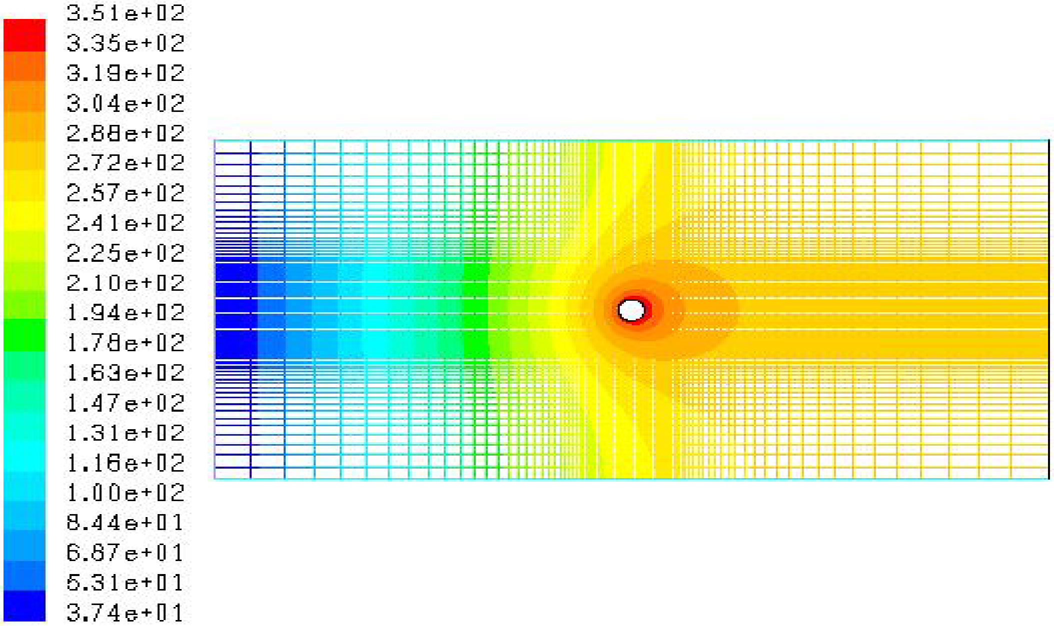

Figure 6-16: Temperature Contour Plot for 2000 RPM and 11.4 ipm.

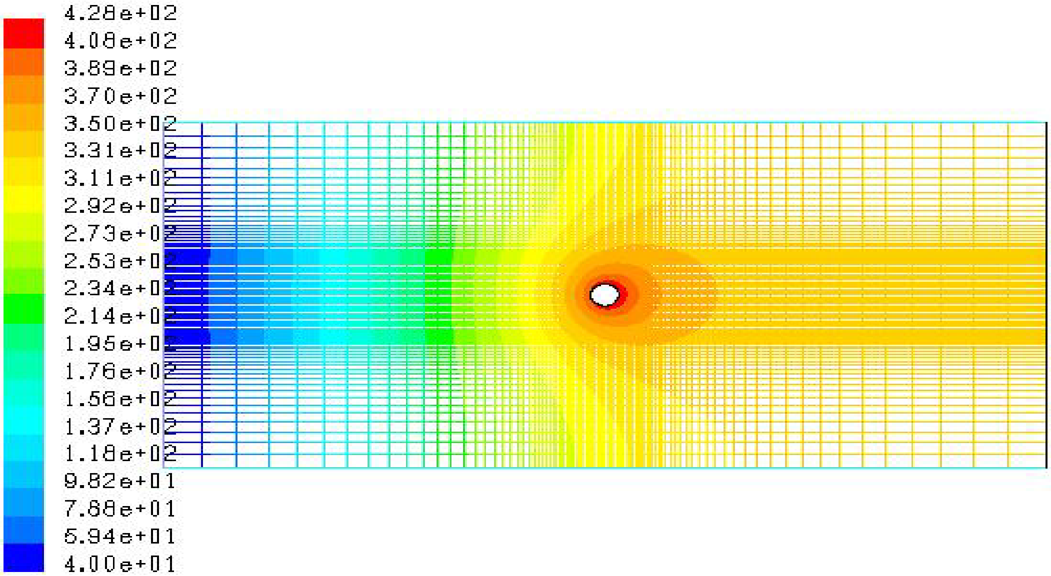

Figure 6-17: Temperature Contour Plot for 2500 RPM and 11.4 ipm.

The contour temperature plots show that as rotational speed is in creased, the preheating temperature of the incoming weld material increases.

Velocity Profile

The velocity profile can be used to understand material flow during FSW. As rotational speed is increased, the velocity of the weld material is expected to increase. On the advancing side, the velocities are additive, while on the retreating side, the velocities are subtractive. Figures 6-18, 6-19, and 6-20 show the velocity magnitude profiles for the tool pin for 1500 rpm/11.4 ipm, 2000 rpm/11.4ipm, and 2500 rpm/11.4 ipm.

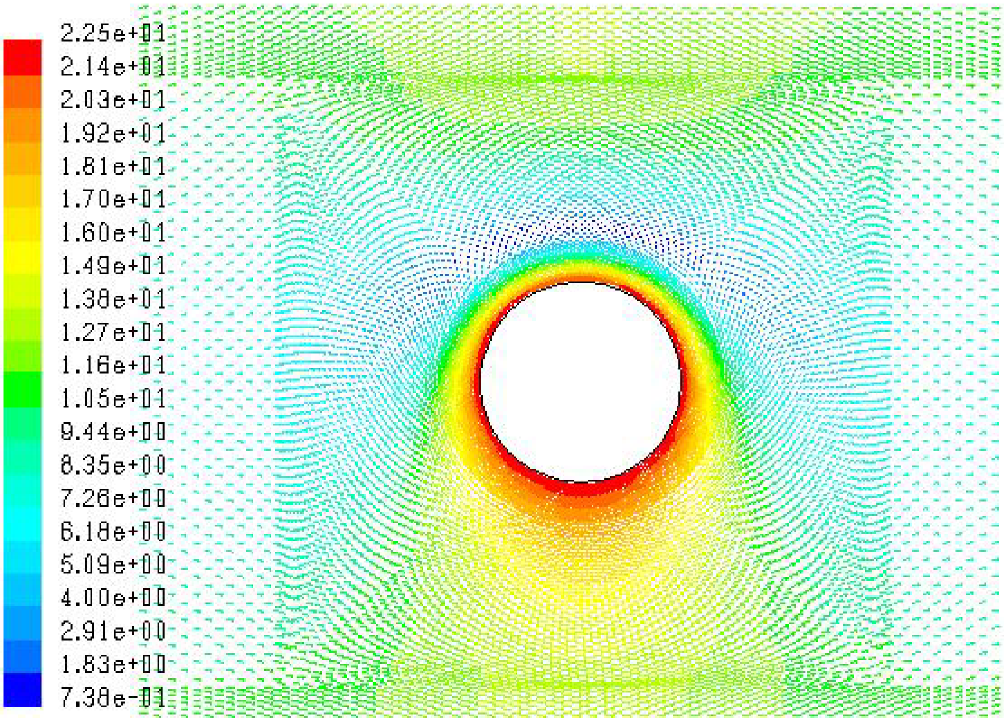

Figure 6-18: Pin Velocity Profile for 1500 rpm/ 11.4 ipm.

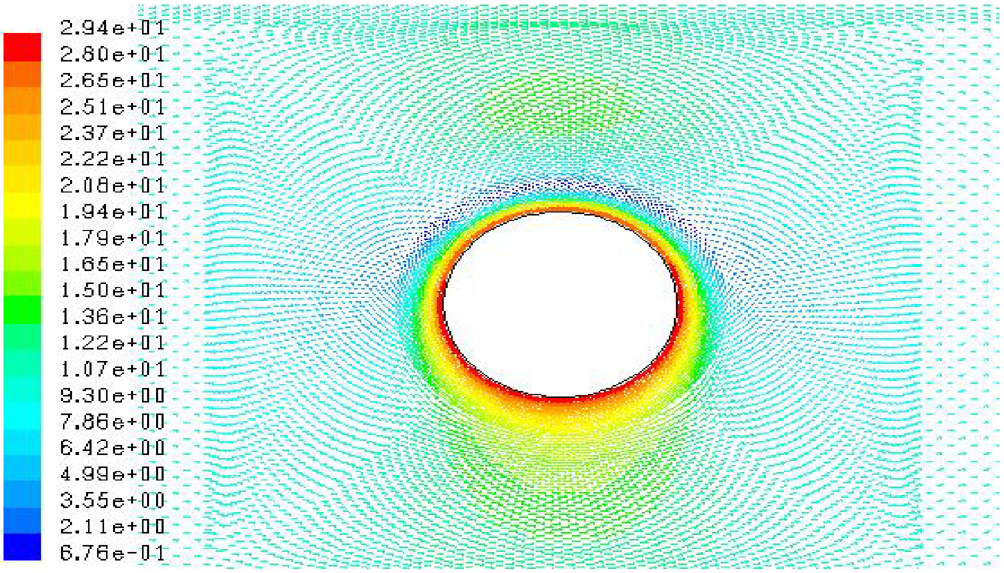

Figure 6-19: Pin Velocity Profile for 2000 rpm/ 11.4 ipm.

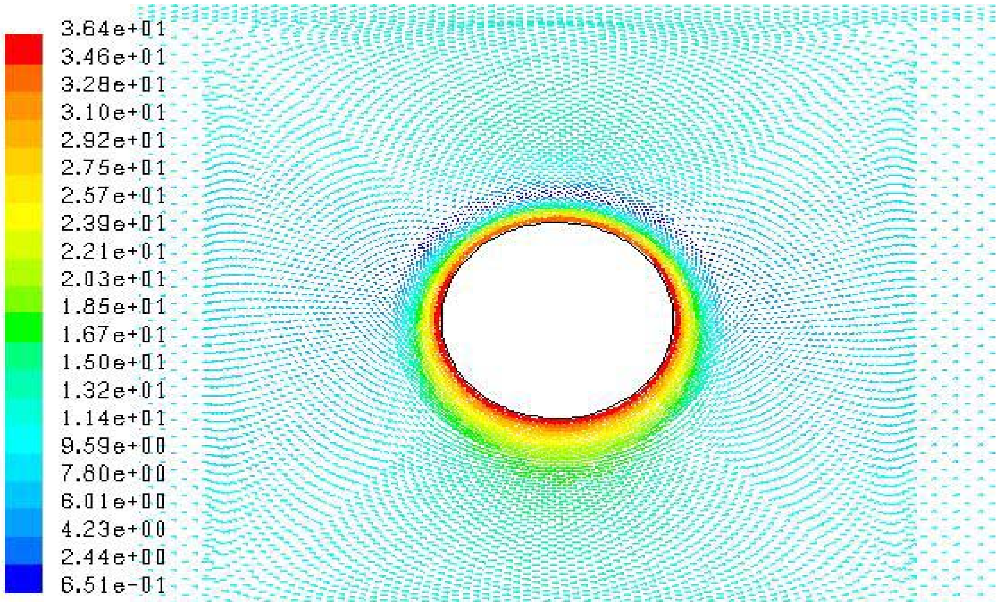

Figure 6-20: Pin Velocity Profile for 2500 rpm/ 11.4 ipm.

In general, the velocity profile for 1500 rpm and a given travel speed are very similar to Figure 6-18 for the Couette and Visco-Plastic flow mode. As rotational speed is increased, the velocity profiles wee very similar to Figures 6-19 and 6-20.

The velocity profiles presented here resemble the shape of the third body region proposed by Abregast et al. [38]. However, as rotational speed is increased, the profile begins to balance and is not skewed toward to advancing side as shown in Figures 6-18. It should be noted that the velocity profile for 1500 rpm/11.4 ipm does not resemble the Couette Flow diagram in Figure 4-1. However, as the velocity profiles in Figures 6-19 and 6-20 become more concentric with the tool pin, as assumed by the Coutte Flow model (Figure 4-1), the Couette Flow predictions improve.

CHAPTER VII

CONCLUSION AND RECCOMMEDATIONS

Experimental

The experimental data shows that the increased rotational speed/decreased force relationship exists for rotational speeds ranging from 1500 rpm to 4500 rpm, and for travel speeds from 11.4 ipm to 63.3 ipm. The percentage decreases in axial force for increasing weld pitch can be seen in Tables 5-2 and 5-3. Reducing the travel speed was observed to be a more effective method for reducing axial force. Increasing rotational speed was observed to be a viable option for reducing axial force as well. However, the present limitation to fully exploiting these relationships is the overheating of the weld material observed at high weld pitches. Appendix C shows photos of welds which experienced overheating and subsequent surface deformation. An investigation into possible methods for extracting heat away from the weld material will be necessary for high weld pitch FSW to be achieved. Another possible solution would be the implementation of force feedback control to high weld pitch FSW setups.

The experimental data shows that the increased rotational speed/decreased torque relationship exists for rotational speeds ranging from 1500 rpm to 4500 rpm, and for travel speeds from 11.4 ipm to 63.3 ipm. The percentage decreases in torque for increasing weld pitch can be seen in Tables 5-4 and 5-5. Increasing rotational speed was observed to be a more effective method for reducing the welding torque. Reducing travel speed was observed to be a viable option for reducing the welding torque as well.

The steady state plots of the translational and transverse forces follow the general parametric relationship of increased rotational speed/ decreased force, however as the rotational speed is increased, a new relationship becomes apparent.

Increasing the rotational speed for a constant travel speed creates a varying contact condition at the tool pin/material interface. As the rotational speed is increased, the contact condition at the tool pin transitions from sticking to partial sliding/sticking. The transition of the contact condition was observed to signal that the process parameters were approaching a critical weld pitch. The critical weld pitch is the weld pitch at which an increase in weld pitch led to the over-heat phenomena.

The welding power was observed to be nearly constant for a constant travel speed, which correlates well with the rotating plug model suggested by Nunes et al. [25].

2-D Model

At low weld pitches, the Couette Flow model did not correlate very well with the experimental results. As the weld pitch increases, the experimental results and the Couette Flow model begin to converge. This implies that the Coutte Flow model is more predictive for very high weld pitches.

Overall, the Visco-Plastic flow model was more accurate than the Couette Flow model over the range of weld pitches. The Visco-Plastic Flow model also converged with the experimental results as the weld pitch was increased.

The steady state welding temperature was not measured during the experiment. However, the results correlate well with the weld temperatures (up to 547 ºC) predicted by Song et al. [44]. Similar temperatures were predicted by Sato et al. for

Al 6063[45], which is similar to Al 6061 in chemical composition and physical properties [44].

The velocity profiles presented here resemble the shape of the third body region proposed by Abregast et al. [38]. However, as rotational speed is increased, the profile begins to balance and is not skew towards to advancing side as shown in Figure 6-18. It should be note that the velocity profile for 1500 rpm/11.4 ipm does not resemble the Couette Flow diagram in Figure 4-1. However, as the velocity profiles in Figures 6-19 and 6-20 begin to resemble the Coutte Flow model (Figure 4-1), the Couette Flow predictions improve.

APPENDIX A

Travel Speed = 11.4 ipm

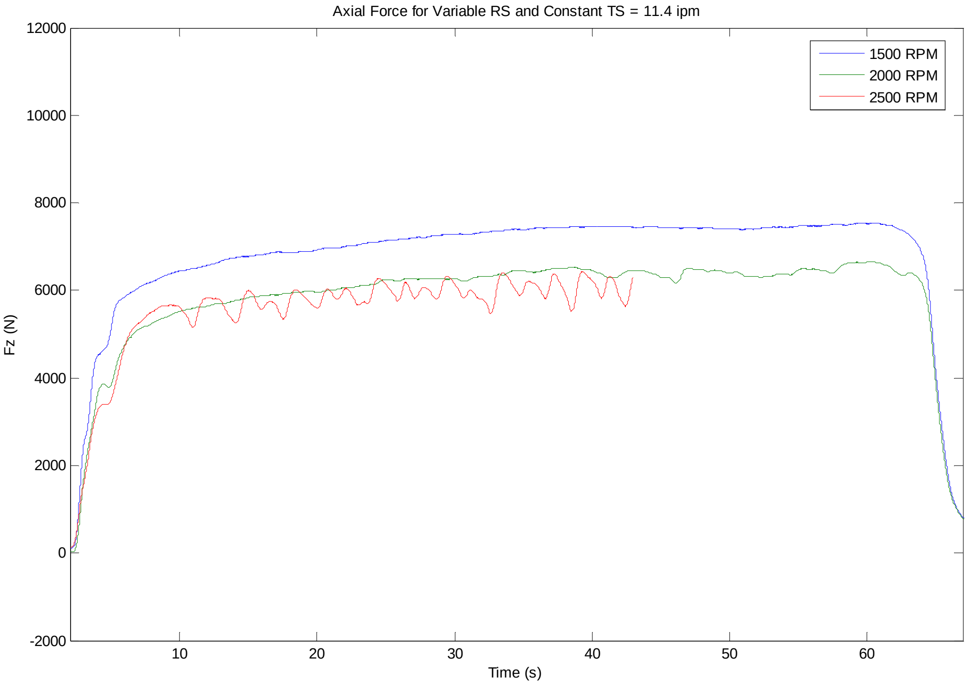

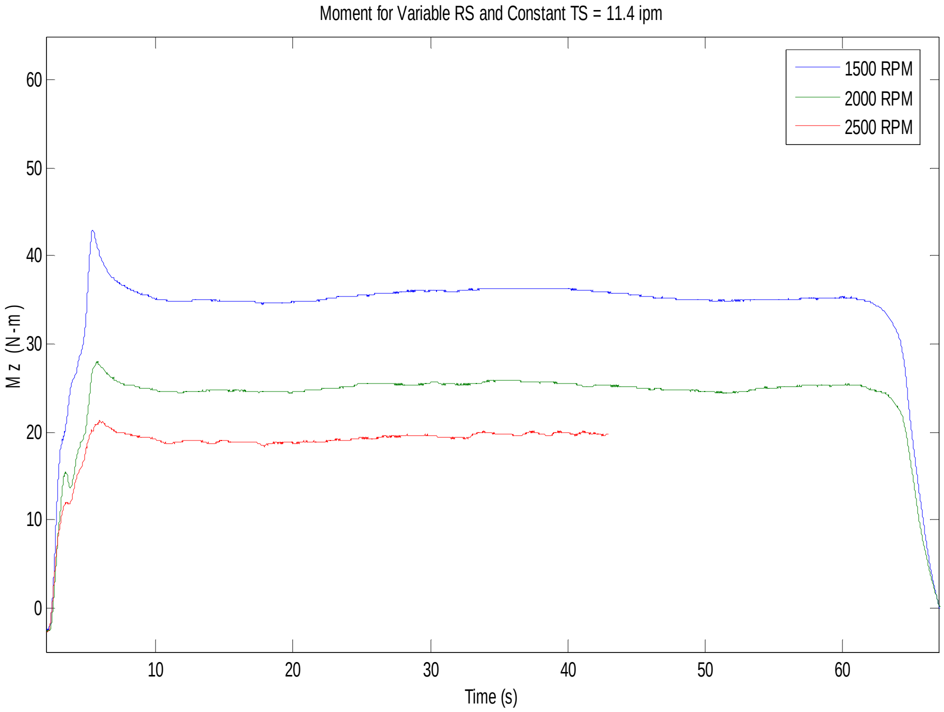

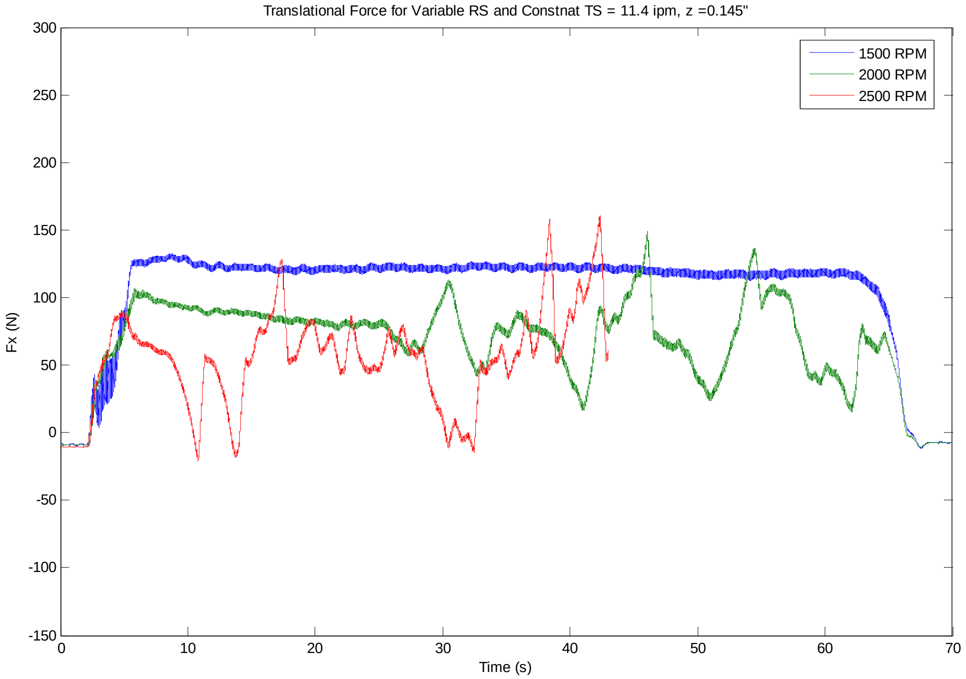
Translational Force for Variable RS and Constnat TS = 11.4 ipm, z =0.145"

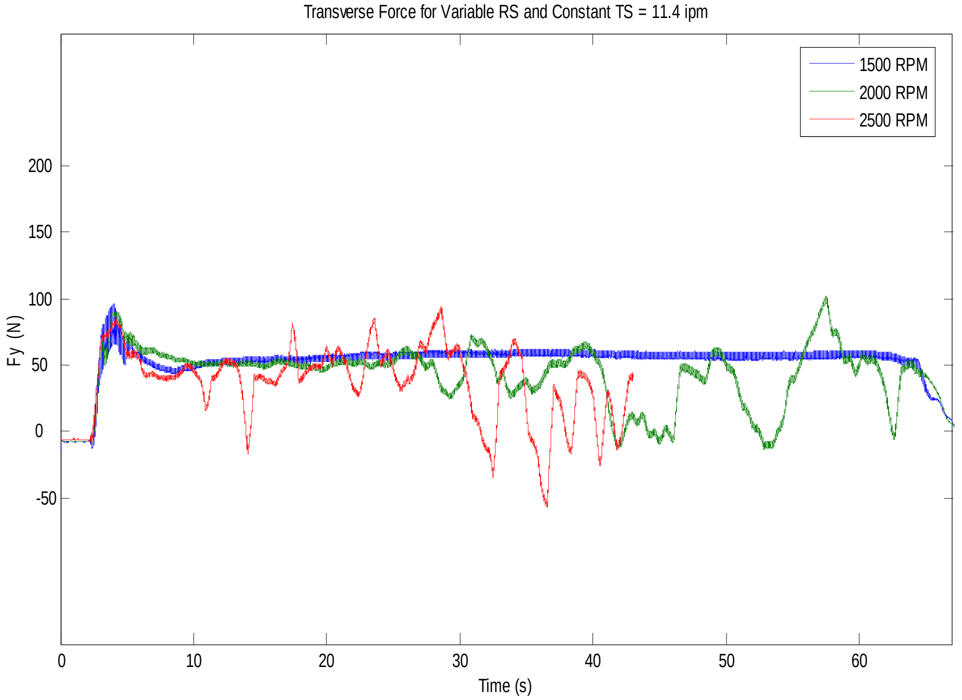
Transverse Force for Variable RS and Constant TS = 11.4 ipm

Travel Speed = 27 ipm

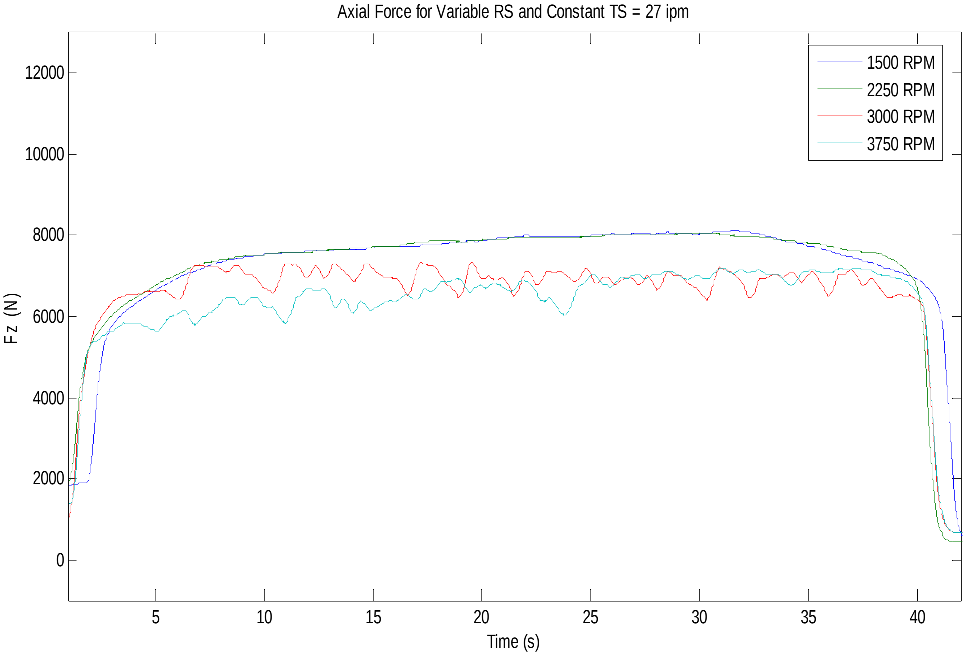

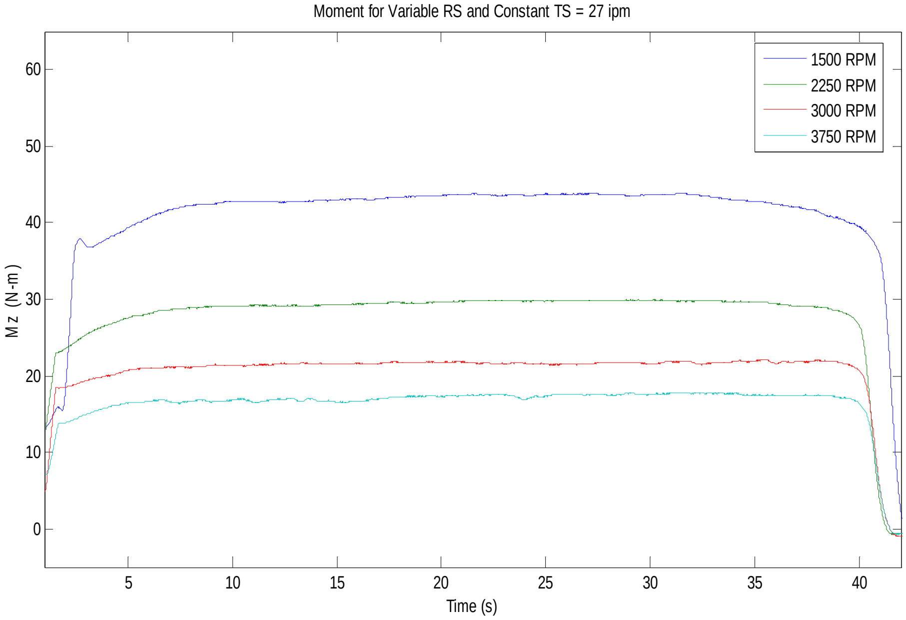

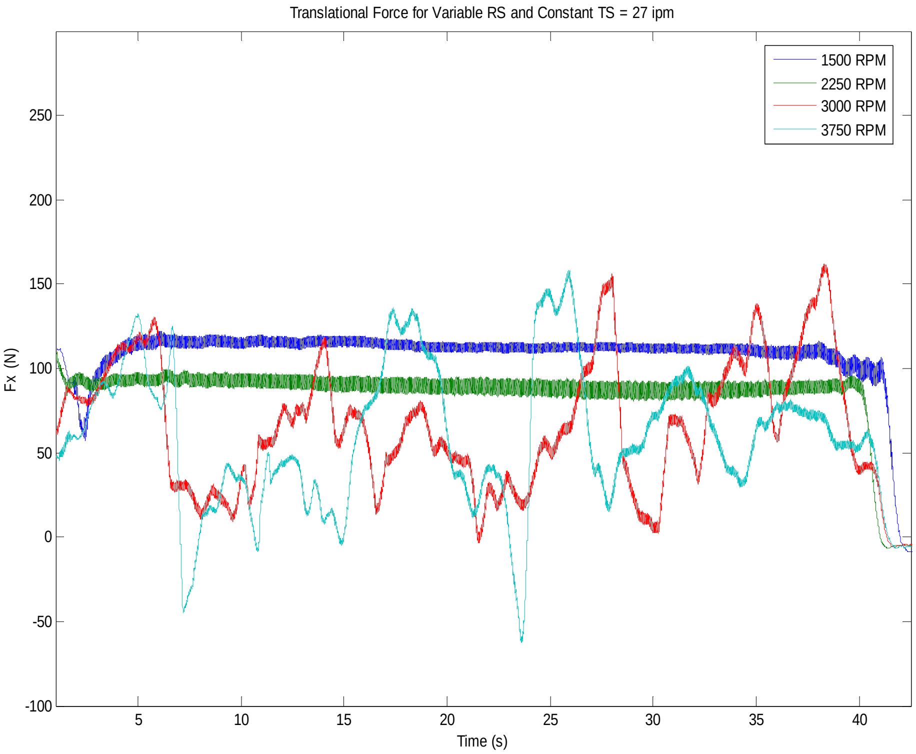
Translational Force for Variable RS and Constant TS = 27 ipm
1500 RPM
2250 RPM
3000 RPM
3750 RPM
Fx (N)
250
200
150
100
50
0
-50
-100
5
10
15
20
25
30
35
40
Time (s)

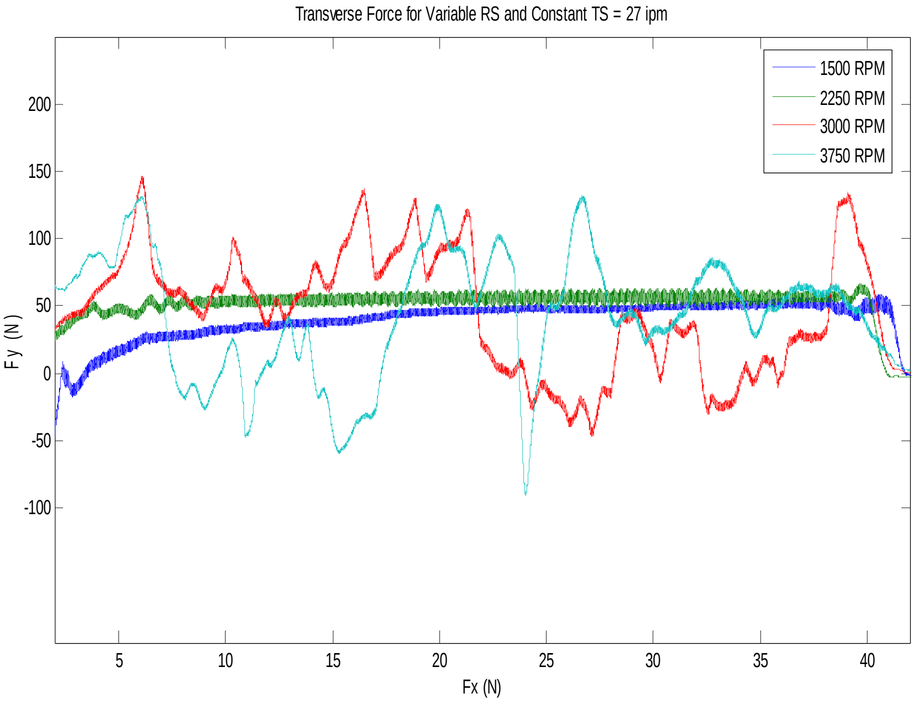
Transverse Force for Variable RS and Constant TS = 27 ipm
1500 RPM
2250 RPM
3000 RPM
3750 RPM
Fy (N)
200
150
100
50
0
-50
-100
5
10
15
20
25
30
35
40
Fx (N)

Travel Speed = 37 ipm

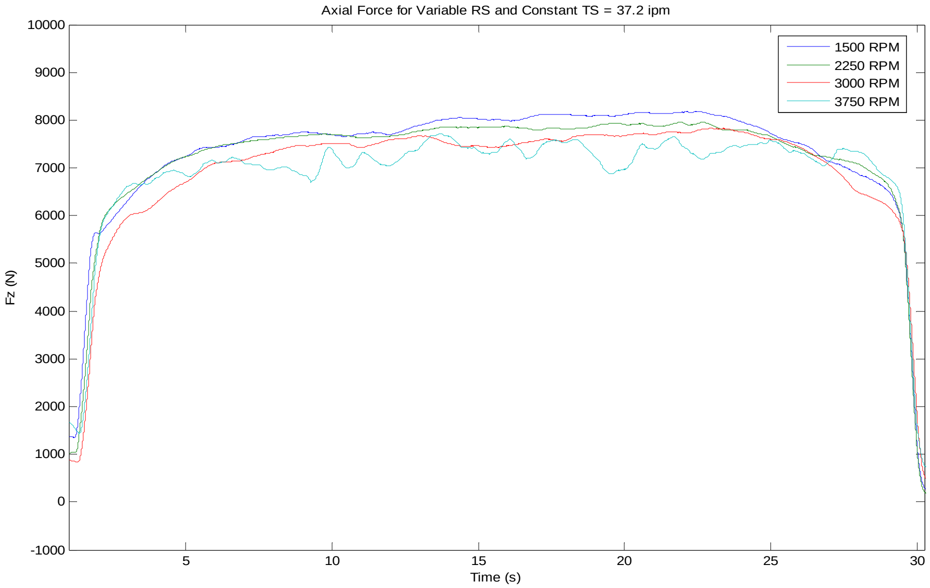

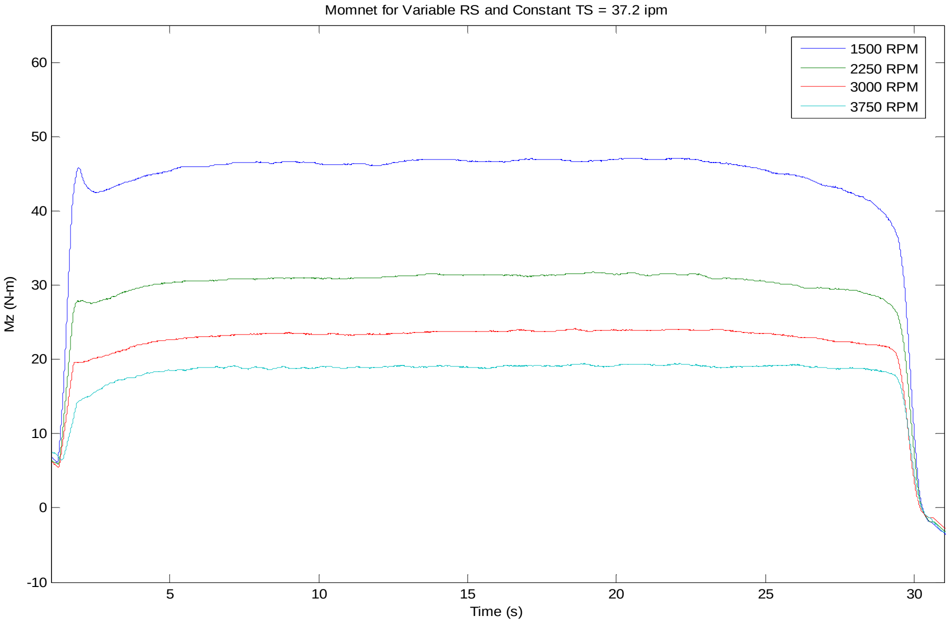

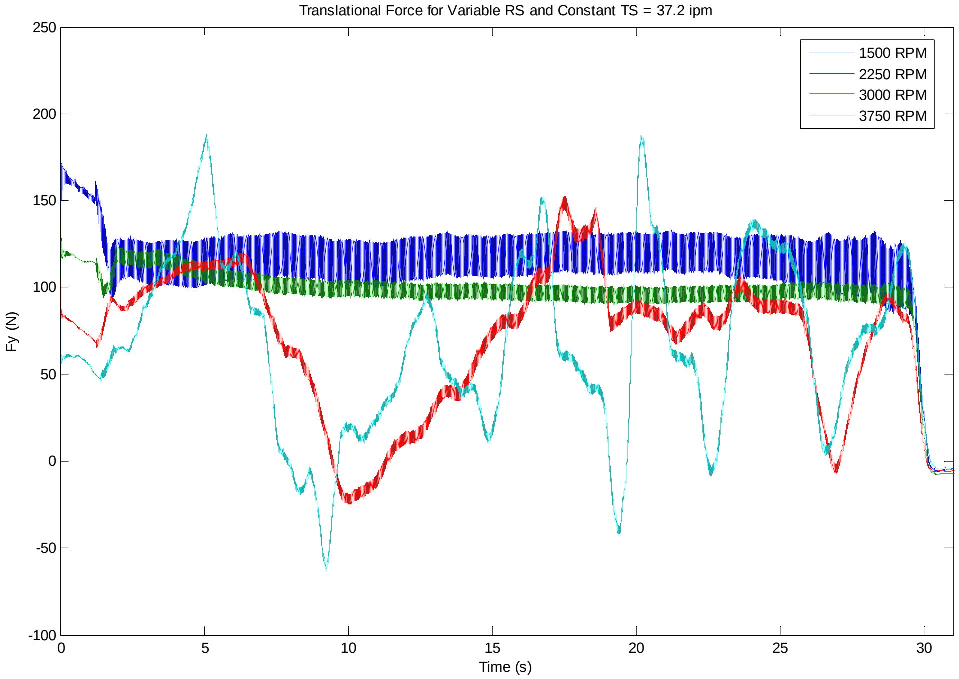
Translational Force for Variable RS and Constant TS = 37.2 ipm
1500 RPM
2250 RPM
3000 RPM
3750 RPM
Fy (N)
Time (s)
250
200
150
100
50
0
-50
-100
0
5
10
15
20
25
30

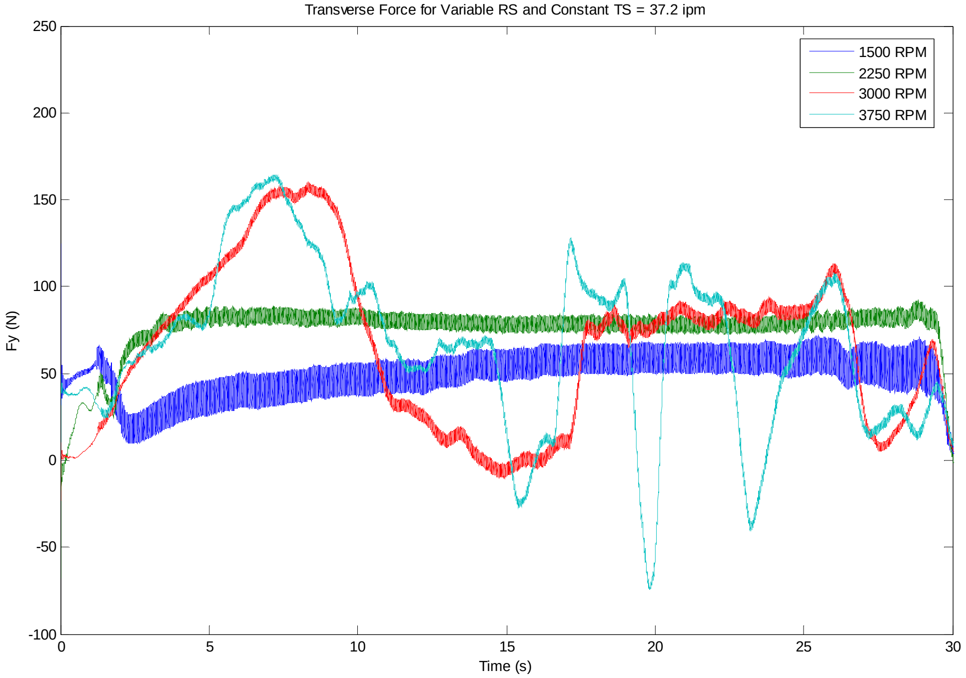
Transverse Force for Variable RS and Constant TS = 37.2 ipm
1500 RPM
2250 RPM
3000 RPM
3750 RPM
Fy (N)
Time (s)
250
200
150
100
50
0
-50
-100
0
5
10
15
20
25
30

Travel Speed = 44.8 ipm

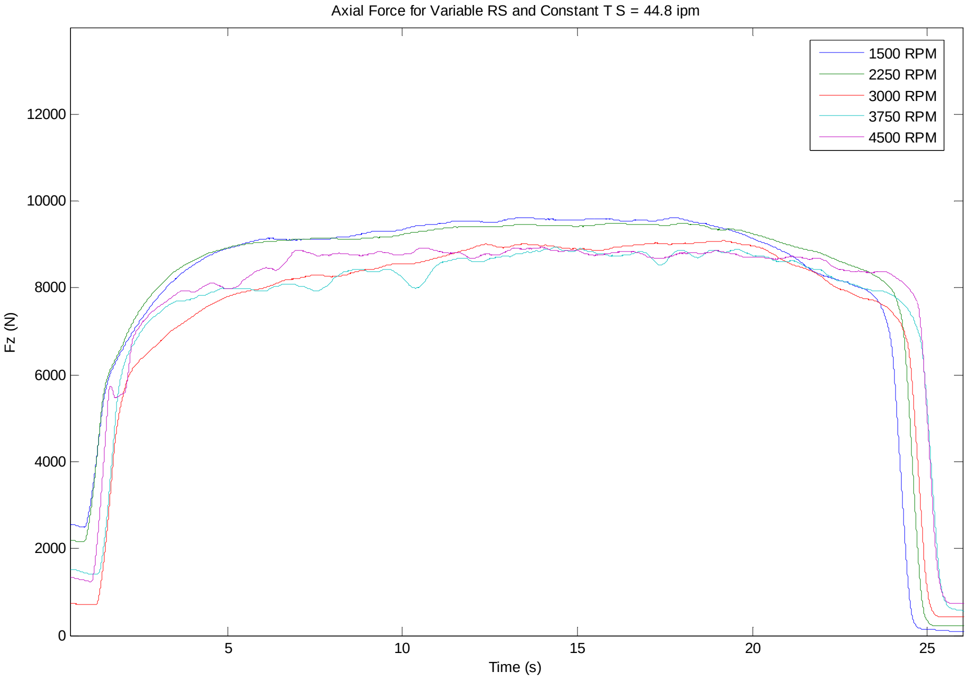

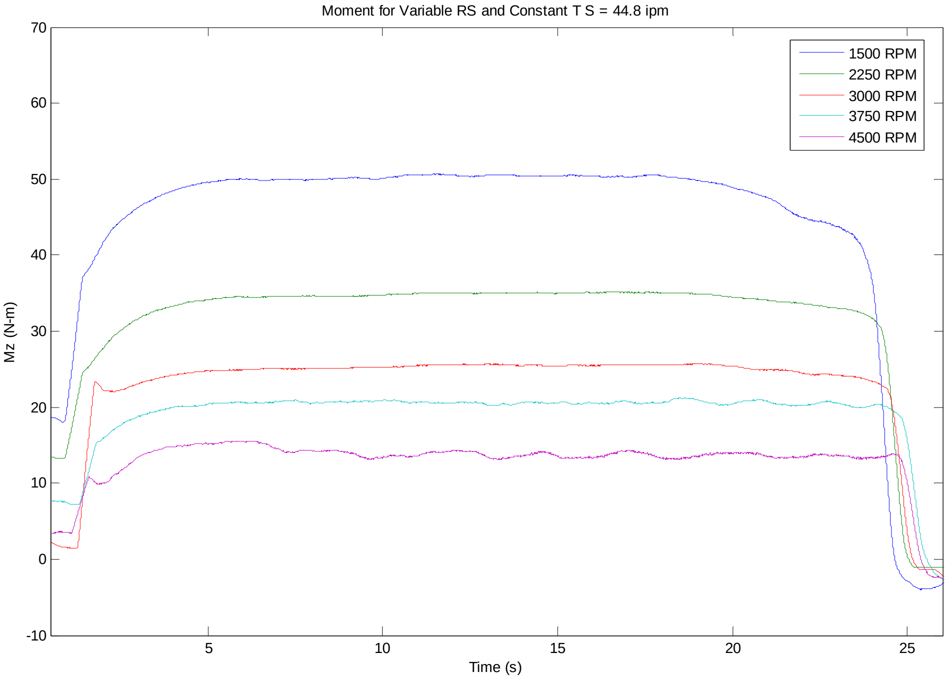

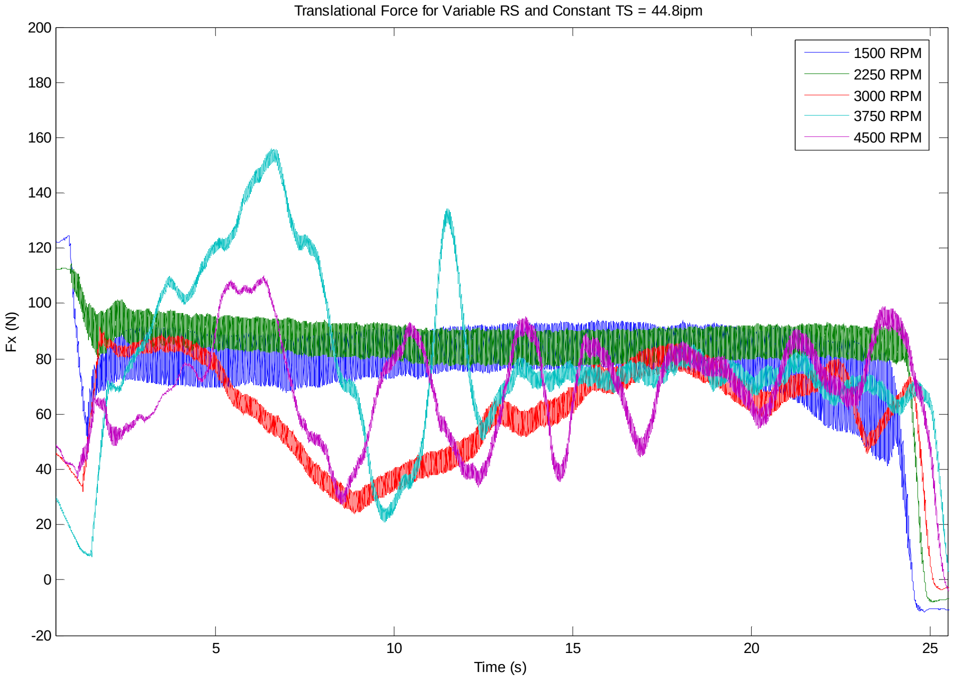
Translational Force for Variable RS and Constant TS = 44.8ipm
Fx (N)
Time (s)
200
180
160
140
120
100
80
60
40
20
0
-20
5
10
15
20
25
1500 RPM
2250 RPM
3000 RPM
3750 RPM
4500 RPM

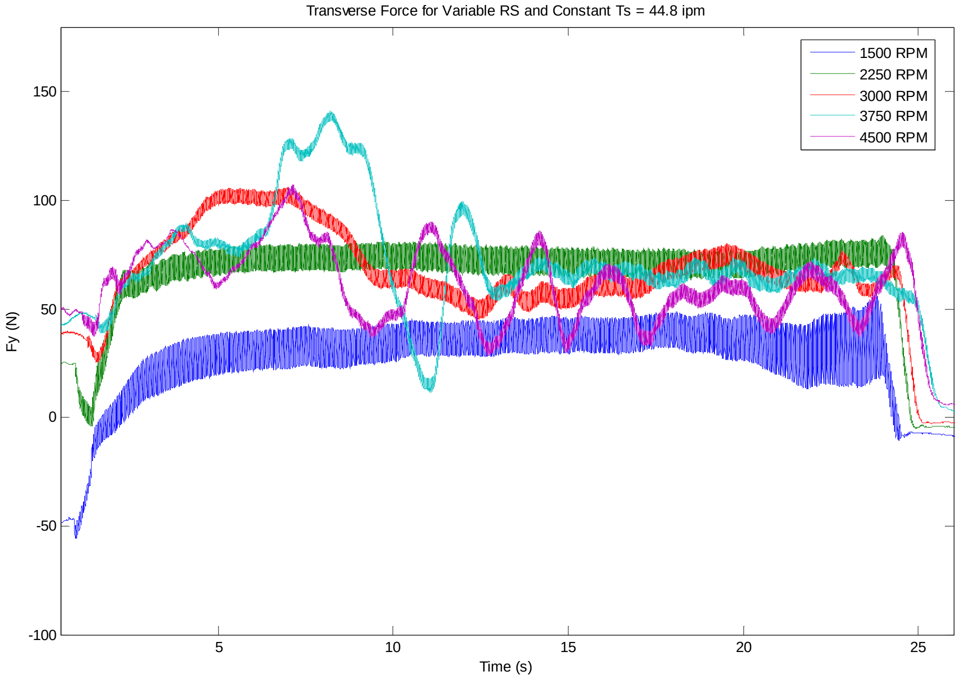
Transverse Force for Variable RS and Constant Ts = 44.8 ipm
Fy (N)
Time (s)
150
100
50
0
-50
-100
5
10
15
20
25
1500 RPM
2250 RPM
3000 RPM
3750 RPM
4500 RPM

Travel Speed = 53.3 ipm

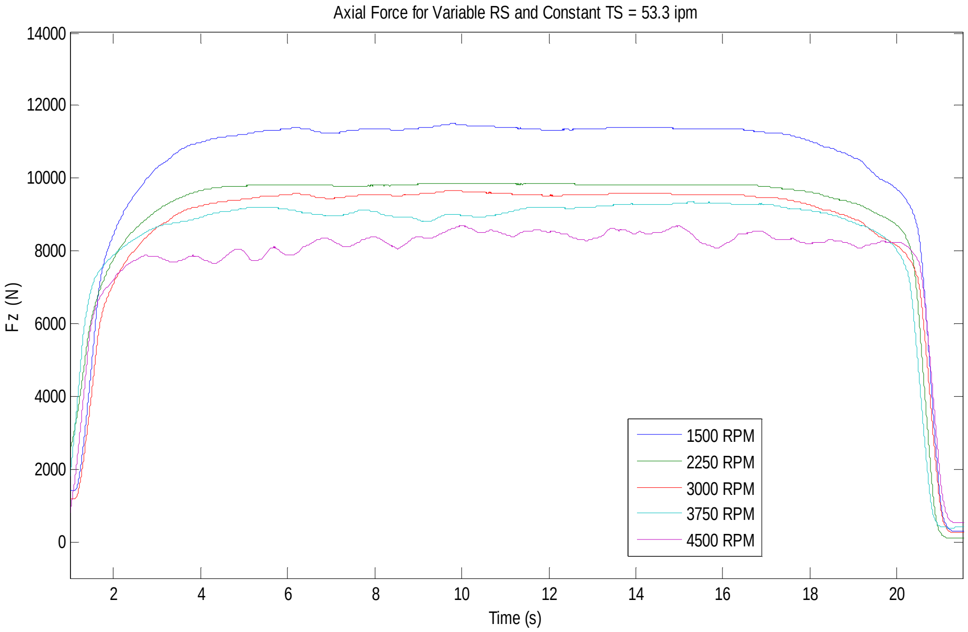

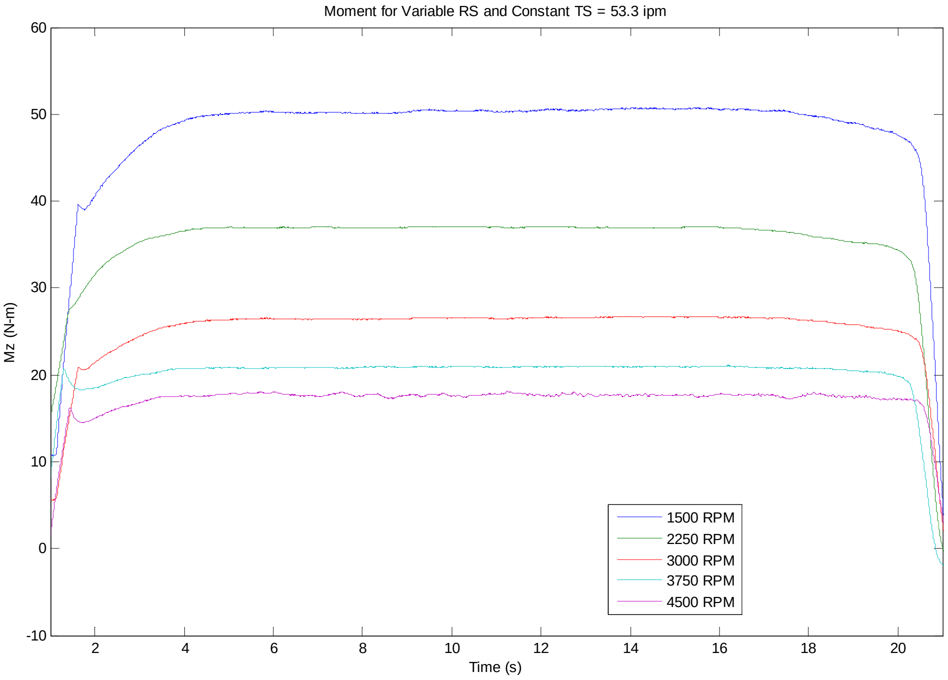

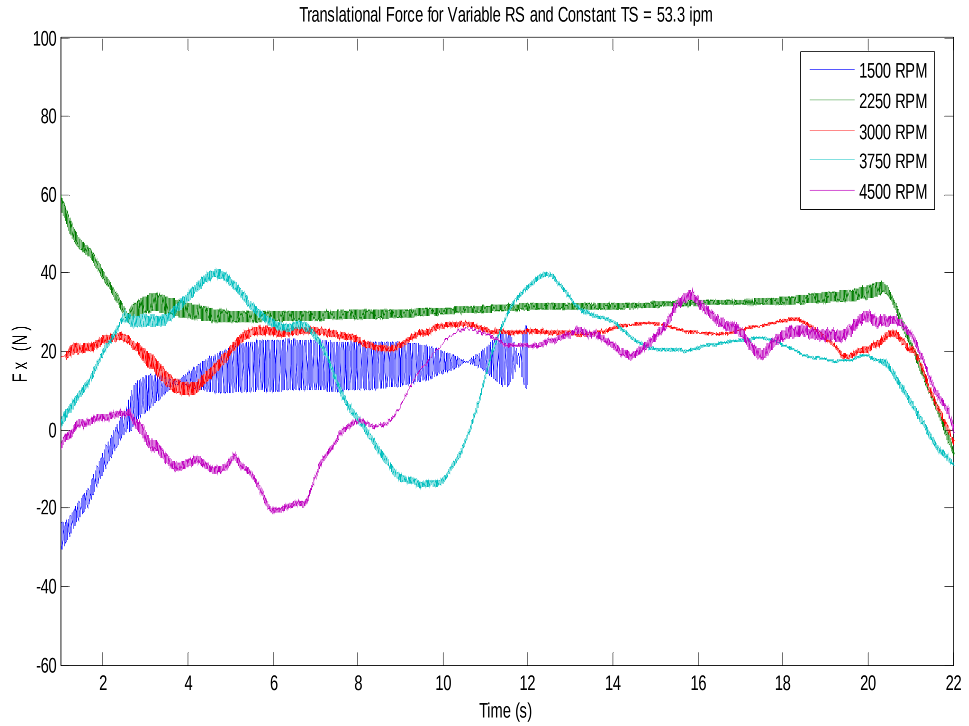
Translational Force for Variable RS and Constant TS = 53.3 ipm
F x (N)
100
80
60
40
20
0
-20
-40
-60
2
4
6
8
10
12
14
16
18
20
22
Time (s)
1500 RPM
2250 RPM
3000 RPM
3750 RPM
4500 RPM

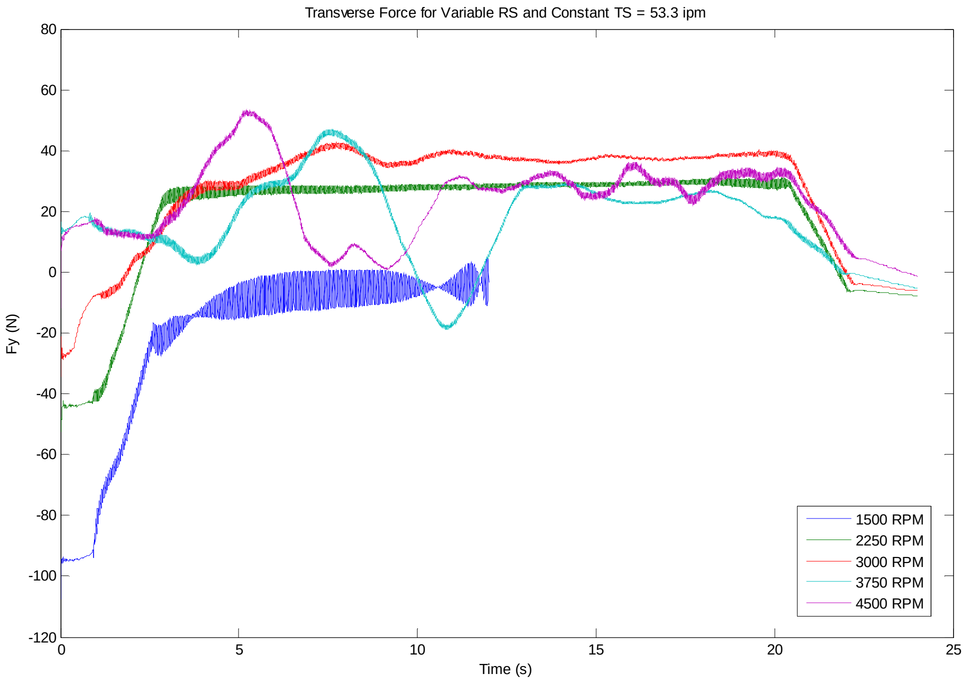
Transverse Force for Variable RS and Constant TS = 53.3 ipm
Fy (N)
80
60
40
20
0
-20
-40
-60
-80
-100
-120
0
5
10
15
20
25
Time (s)
1500 RPM
2250 RPM
3000 RPM
3750 RPM
4500 RPM

Travel Speed = 63.3 ipm

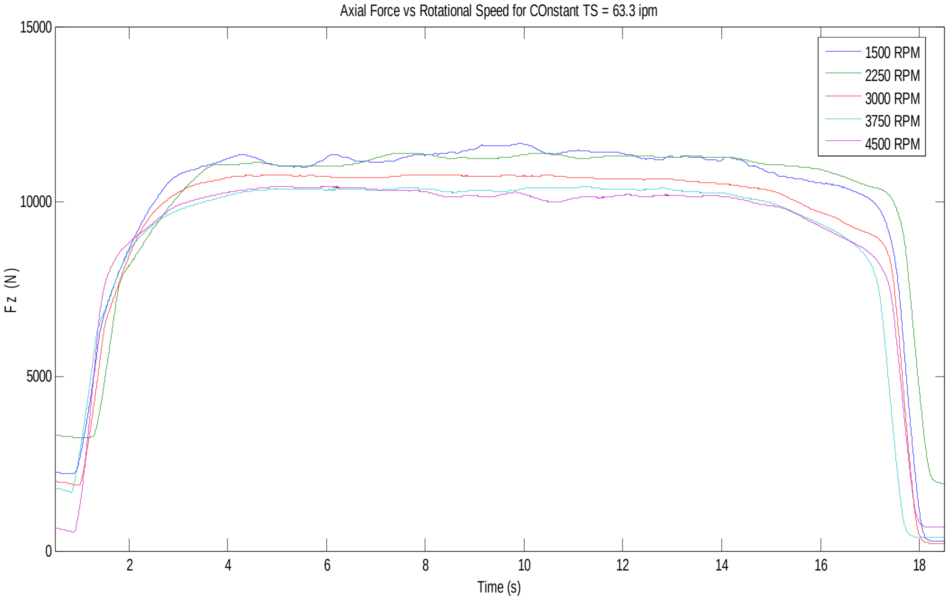

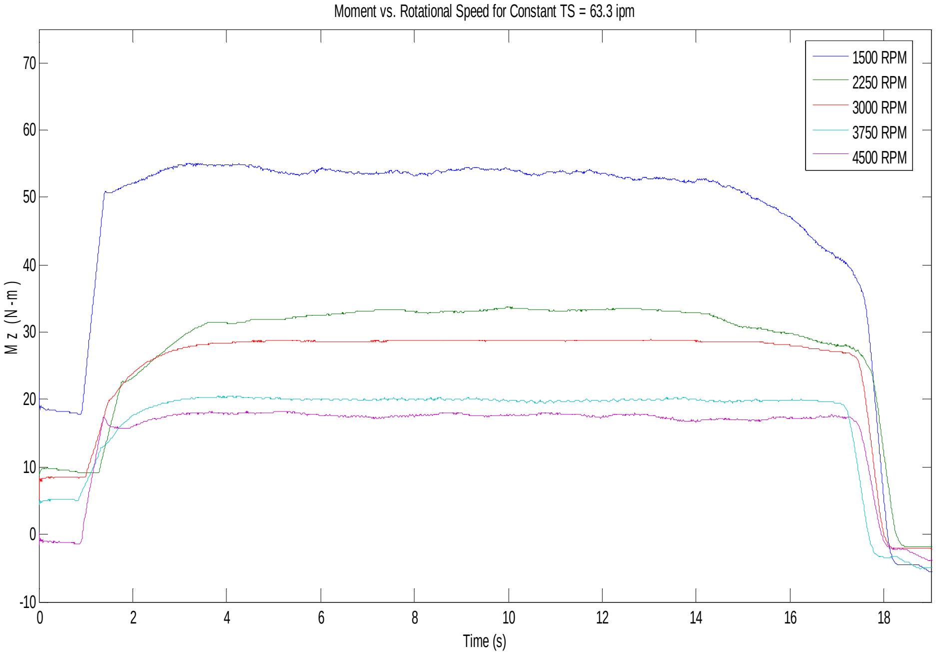

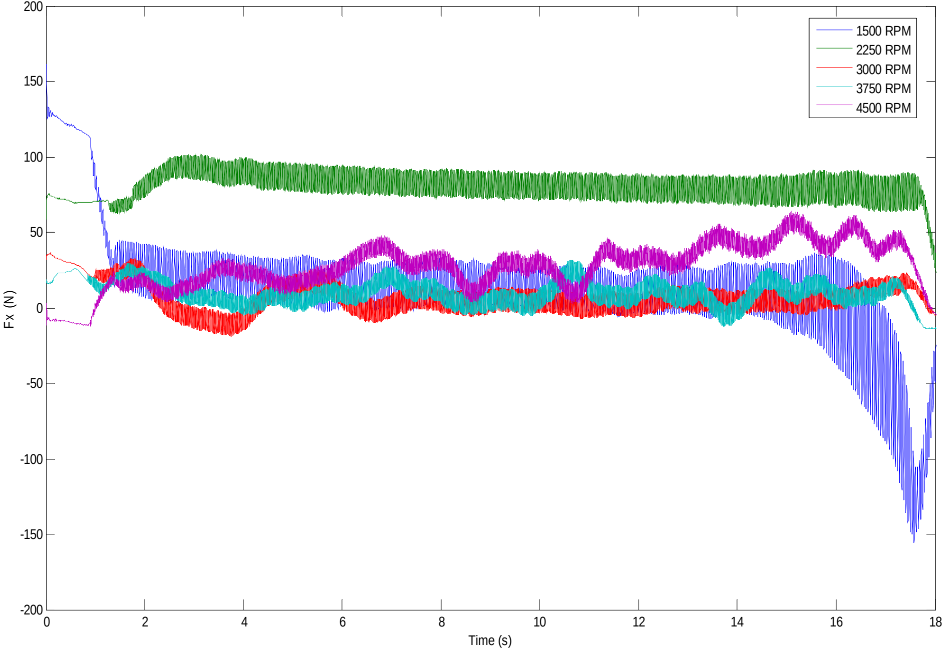
Translational Force vs. Rotational Speed for TS = 63.3 ipm

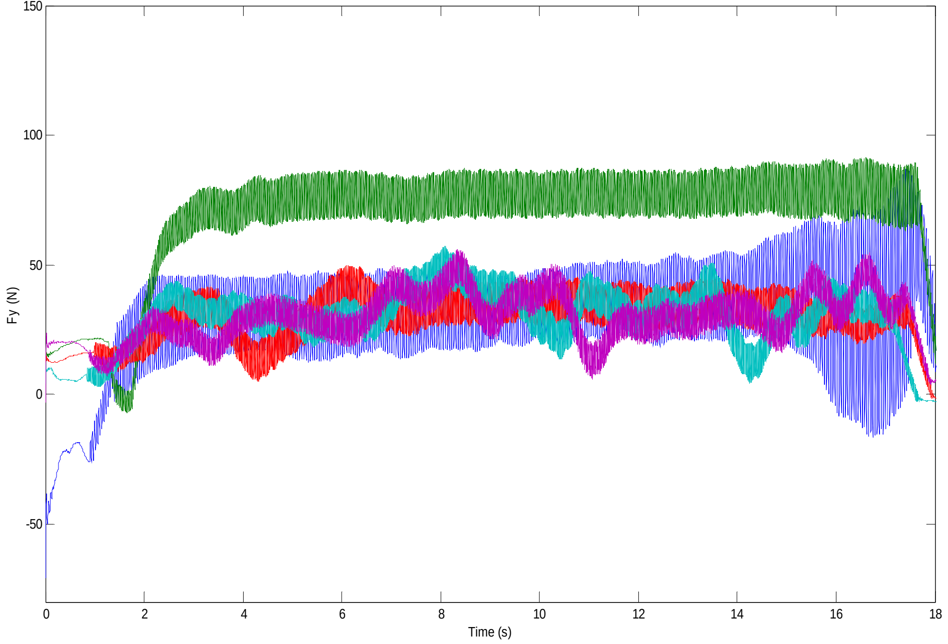
Transverse Force vs. Rotational Speed for Constant TS = 63.3 ipm

APPENDIX B

Deformed Weld for 3000 rpm and 27 ipm.

Deformed Weld for 3750 rpm and 27 ipm

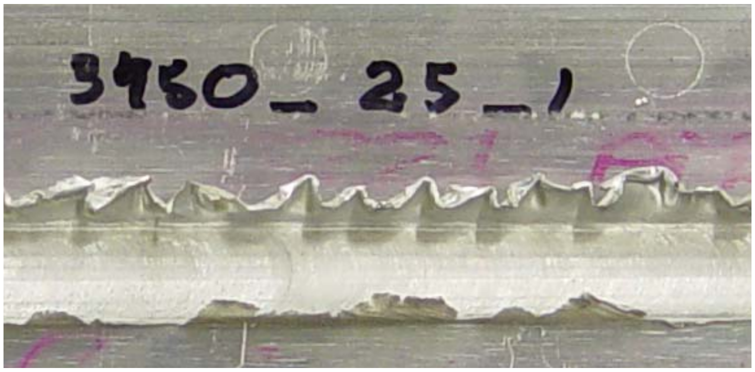

Deformed Weld for 3750 rpm and 37.2 ipm

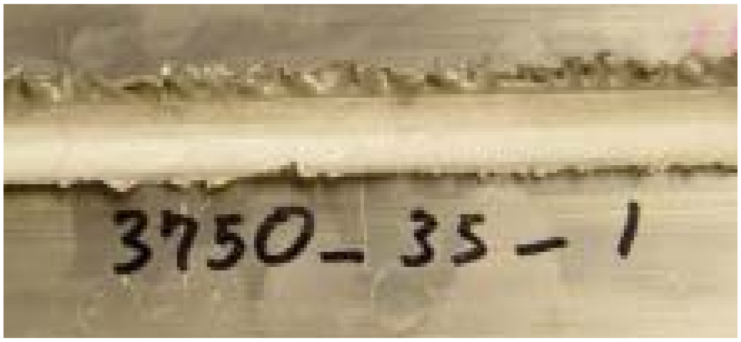

Deformed Weld for 3750 rpm and 44.8 ipm

Deformed Weld for 4500 rpm and 44.8 ipm

APPENDIX C

MATLAB CODE TO POST EXPERIMENTAL DATA

```
load F1.txt
 tx = F1(:,1);
 Fx1 = F1(:,2);
 l = length(Fx1);
 for i = 1:l
     Fx1(i) = Fx1(i)/1;
 end
 n = input('Filter Scale: ');
 for i = 1:n
     sum = 0;
     for j = 1:i
         sum = sum + Fx1(j);
     end
     Fx1smth(i) = sum / i;
 end
 for i = (n+1):l
     sum = 0;
     for j = 0:(n-1)
         sum = sum + Fx1(i-j);
     end
     Fx1smth(i) = sum / n;

 end
```

REFERENCES

[1] Thomas W.M., et al. 1991, Friction Stir Butt Welding. International Patent Application # PCT/GB92/02203, GB Patent Application #9125978.8, and GB Patent # 2,306,366.

[2] http://www.twi.co.uk/j32k/unprotected/band_1/fswjoint.html

[3] Nicholas E. D., and Kallee, S.W., 2000, "Friction Stir Welding – A decade on." IIW Asian Pacific International Congress. Sydney 29 October to 2 November

[4] Heideman R. J. et al., 2000, Friction Stir Welding Tool. U.S. Patent #6,053,391

[5] Carter, Robert W., "Pin Tool Design" *Proceedings of the NASA MSFC Friction Stir Welding Workshop and Showcase, Huntsville, Al, September 2003*

[6] Thomas, W.M., et al., 1995, Friction Welding. U.S. Patent # 5,460,317

[7] Cocks, E. E., et al., 2000, Enantiomorphic Friction-Stir Welding. U.S. Patent # 6,029,879

[8] Su, J. Q., 2003, *Acta Materialia*. **51** 713-729

[9] Mahoney, M.W., Rhodes, C.G., Flintoff, J.G., Spurling, R.A., and Bingel, W.H., 1998, *Metall. Mater. Trans. A*. **29A** (1998) 1955-1964.

[10] Heinz, B., Skrotzki, B., and Eggler, G., 2000, *Mater. Sci. Forum*. **331–337** 1757-1762.

[11] Svensson, L.E., Karlsson, L., Larsson, H., Karlsson, B., Fazzini, M., and Karlsson, J., 2000, *Sci. Technol. Welding Joining*. **5** 285-296.

[12] Reynolds, A.P., Lockwood, W.D., and Seidel, T.U., 2000, *Mater. Sci. Forum.* **331–337** 1719-1724.

[13] Lumsden, J.B., Mahoney, M.W., Pollock, G. and Rhodes, C.G., 1999, *Corrosion.* **55** 1127-1135.

[14] Murr, L.E., Liu, G. and McClure, J.C., 1998, *Mater. Sci.*. **33** 1243-1251.

[15] Rhodes, C.G., Mahoney, M.W, Bingel, W.H., Spurling, R.A., and. Bampton, C.C., 1997, *Scripta Mater.* **36** 69-75.

[16]. Jata, K.V., Sankaran, K.K, and Ruschau J.J., 2000, *Metall. Mater. Trans. A,* **31A** 2181-2192.

[17] Liu, G., Murr, L.E., Niou, C.S., McClure, J.C., and Vega, F.R., 1997, *Scripta Mater.* **37** 355-361.

[18] Sato, Y.S., Kokawa, H., Enomoto M., and Jogan, S., 1999, Metall. Mater. Trans. A*,* **30A** 2429-2437.

[19] Su, J.-Q., Nelson, T.W., Mishra, R., and Mahoney, M., 2003, *Acta Mater.* **51** 713-729.

[20] Kwon Y.J., Shigematsu I., Saito N., 2003, *Scripta Materialia.* **49** 785-789

[21] Lee W. B., Yeon Y. M., Jung S. B., 2003, *Materials Science and Technology*. **19** 1513 - 1518

[22] Ulysse, P., 2002, *International Journal of Machine Tools & Manufacture*. **42** 1549–1557

[23] Johnson W., Kudo H.K., ***The Mechanics of Extrusion***., 1962, Manchester University Press, UK P.40

[24] FIDAP, Fluid Dynamic Analysis Package, version 7.6, Fluid Dynamics International, Evanston, IL. 2002

[25] Reynolds A P, Deng X, Seidel T and Xu S., 2000, *Proc. Joining of Advanced and Specialty Materials* (St Louis, MO, ASM International) pp 172–177

[26] Nunes A.C., Bernstien, E.L., and McClure, J.C., A rotating Plug Model for Friction Stir Welding. Paper presented at the 81st American Welding Society annual Convention, Chicago, IL, April 26-28, 2000

[27] Mitchell, Jason. *Experimental Thermo-mechanics of Friction Stir Welding.* M.S. Thesis, Vanderbilt University, 2002

[28] Guerra M., Schmidt C., McClure J.C., Murr, L.E., Nunes A.C., 2003, *Materials Characterization*. **49** 95-101

[29] Colligan, K., 1999, *Welding Journal*, **78** 229 –237.

[30] Colegrove P. 2000, 3-Dimensional Flow and Thermal Modeling of the Friction Stir Welding Process. Paper presented at the 2nd Int. Symp. on Friction Stir Welding, Gothenburg, Sweden, June 27-29, 2000

[31] Shercliff H. R., and Colgrove P. A., 2002, *Math. Modelling Weld. Phenom.* **6** 927–974

[32] Chen C.M., Kovacevic R., 2003, *International Journal of Machine Tools & Manufacturing* **43** 1319–1326

[33] http://www.memagazine.org/medes03/coolweld/coolweld.html

[34] Thomas, W.M., Threadgill P.L., and Nicolas E.D., 1999, *Science and Technology of Welding and Joining.* **4(6)** 365-372

[35] Mills, K.C., *'Recommended Values of thermophysical properties for commercial alloys'*, 68-71; 2002, Woodhead Publishing Ltd., Cambridge, UK

[36] North T.H. North, G.J. Bendzsak and C. Smith. Material Properties Relevant to 3-D FSW Modeling. Paper presented at the 2nd Int. Symp. on Friction Stir Welding, Gothenburg, Sweden, June 27-29, 2000

[37] http://scienceworld.wolfram.com/physics/RayleighCriterion.html

[38] G.F. Braun and W.J. Arbegast, "Aluminum Flow Stress Determinations Using A Gleeble System", presented at the 11th Annual Advanced Aerospace Materials and Processes Conference and Symposium, *ASM International*,
Seattle WA, March 14-15, 2000

[39] Chao, Y. J., and Qi, X., 1999, *1st Int. Symp. on Friction Stir Welding (Thousand Oaks, CA, USA)*

[40] Russell M J and Shercliff H R 1999 *1st Int. Symp. on Friction Stir Welding (Thousand Oaks, California, USA)*

[41] Schmidt, H., Hattel, J., Wert, J. 2004, *Modeling and Simulation in Materials Science and Engineering*. **12** 143–157

[42] Sheppard T., Jackson A. 1997, *Mater. Sci. Technol.***13** 203-209.

[43] FLUENT, Fluid Dynamic Analysis Package, version 6.122 Fluid Dynamics International, Evanston, IL. 2004

[44] Song M., and Kovacevic R. 2003, *Mach. Tools Manuf.* **43** 605–15

[45] White, F., Kudo H.K., ***Viscous Fluid Flow***, 1991, McGraw-Hill P.112